TECHNICAL UNIVERSITY OF CRETE

DOCTORAL DISSERTATION

Contributions to Satellite Altimetry Calibration with Microwave Transponders and Corner Reflectors in the context of Fiducial Reference Measurements

Author:
Konstantinos Kokolakis

Supervisory Committee:
Prof. Stelios P. Mertikas
Prof. Dionissios Hristopulos
Prof. Panagiotis Partsinevelos

A dissertation submitted in partial fulfillment of the requirements for the degree of Doctor of Philosophy

in the

Laboratory of Geodesy and Geomatics Engineering
School of Mineral Resources Engineering

May 5, 2023

"There is nothing permanent except change."

Heraclitus

Abstract

This dissertation improves satellite altimetry calibration by strengthening existing procedures, integrating active and passive targets, proposing new calibration methodologies and revisiting calibration processing.

Satellite altimetry provides measurements for assessing Earth's climate by monitoring oceans and inland waters. The primary measurement of altimetry is the range between the altimeter and the surface of the Earth. Accuracy and reliability of altimetric range are ensured through dedicated calibration. Over the last decades the developments in instrumentation and algorithms increased the accuracy of altimetric measurements. For example TOPEX/Poseidon (launched in 1992) measured ocean topography to an accuracy of 4 cm while Sentinel-3A (launched in 2016) reached an accuracy of 2 cm. On the other hand, external calibration, the only means of controlling altimeters accuracy post-launch, remained practically unchanged.

To cover this gap, this work improves the reliability and accuracy of calibration by mitigating its largest sources of uncertainty. These have been determined following Fiducial Reference Measurements (FRM) principles and are the wet delay, transponder's internal delay, geophysical corrections and calibration processing approximations. The FRM have been established by the European Space Agency to standardise the bias estimation. The dissertation is separated into four sections, each one presenting a research objective and the corresponding contribution of this work.

The first objective has been to increase the confidence in the estimation of the most variable parameter in altimetry calibration, the wet delay. This was achieved by validating and implementing two independent techniques for estimating wet delays, i.e., the Ocean and Land Colour Instrument on-board Sentinel-3 and the MP-3000A ground radiometer. The implementation of these techniques additionally to the conventional GNSS methods, offers redundant and independent estimation of wet delay correction for range calibration.

The second objective has been to evaluate alternative methods of point target calibration, and assess their advantages with respect to currently-used methods. This would mitigate potentially the largest error of calibration using a transponder, the transponder's internal delay. After a systematic assessment of several calibration techniques, the integration of active (transponder) and passive (corner reflectors) point targets at the same calibration network is proposed. The main reference target of the proposed calibration technique is the transponder because of its higher signal to noise ratio. The tandem operation of diverse targets allows to monitor the largest uncertainty of transponder calibration (i.e., internal delay) by comparing its echo with this of corner reflectors.

The third objective has been to design new techniques, in order to mitigate the uncertainty of calibration, accounting for the increased accuracy of modern missions. This dissertation proposes a new technique for altimetry calibration called Altimeter Differential Corner Reflector (ADCR). The ADCR offers for the first time a bias free of atmospheric, geophysical and orbital errors. This elimination of calibration errors is achieved by co-locating corner reflectors to experience identical effects. A differential bias is thus estimated, which originates from the comparison of corner reflectors range difference (estimated using altimetry measurements) against their known distance.

The last objective, has been to revisit conventional calibration processing to reduce approximations that could degrade bias reliability. For this objective, the approximation of applying a constant offset to perform the common reference of the measured and geometrical ranges is examined. A comprehensive methodology is proposed for accurately referencing the measured and geometric ranges at the same satellite point by incorporating satellite attitude information into calibration. The revised calibration correction on Jason-3, varies from $-2\,\mathrm{mm}$ to $1\,\mathrm{mm}$ for the range bias and from $-110\,\mu\mathrm{s}$ to $110\,\mu\mathrm{s}$ for the datation bias. The magnitude of corrections on datation bias corresponds to about 30% of its average value. The mean bias difference of Jason-3 ascending and descending orbits over the GVD1 transponder is improved by 12%.

To sum up, this work removes the influence of systematic effects both in the ground infrastructure (i.e., internal delay knowledge, atmospheric and geophysical corrections) and on the satellite that depend on both physical characteristics (e.g., internal geometric structure) and attitude realization of each satellite. To ensure that calibration procedures are aligned with the requirements of future satellite missions and FRM standards, the methods proposed in this dissertation should be considered in every current and future Cal/Val infrastructure. The potential impact of this work is to reach sub-cm accuracy in the calibration of satellite altimeters.

Acknowledgements

I would like to express my gratitude to my supervisor, Prof. Stelios P. Mertikas, for his support and cooperation. His passion for research acted as a continuous motivation for this work. Prof. Mertikas's delicate guidance assisted me to understand the final goal of my PhD research, and at the same time allowed me to pave my own "path" to achieve it. My appreciation also goes to my past supervisor Prof. Vasiliki Pavlidou for triggering my achievement drive.

I would like to acknowledge the other members of my supervisory committee, Prof. Dionissios Hristopulos and Prof. Panagiotis Partsinevelos, for their support throughout my studies. Moreover, I thank Assistant Prof. Emmanouil A. Varouchakis, Dr. Craig Donlon, Dr. Josh Willis and Dr. Constantin Mavrocordatos for accepting to serve as members of my examination committee.

Working with my colleagues Achilles Tripolitsiotis, Xenophon Frantzis and Dr. Dimitrios Piretzidis assisted me to evolve as a researcher and to sincerely feel the effectiveness of collegiality.

The long discussions with my friends and the unreserved support, love and understanding of my family helped me to enjoy this challenging "journey".

Contents

List of Figures

List of Tables

List of Abbreviations

A109	Ascending **109**
ADCS	**A**ttitude **D**etermination and **C**ontrol **S**ystem
AOI	**A**rea-**o**f-**I**nfluence
APC	**A**ltimeter **P**hase **C**enter
Cal/Val	**Cal**ibration and **Val**idation
CCD	**C**harge **C**ouple **D**evice
CDDIS	**C**rustal **D**ynamics **D**ata **I**nformation **S**ystem
CoG	**C**enter **o**f **G**ravity
CRISTAL	**C**opernicus **P**olar **I**ce and **S**now **T**opography **A**ltimeter
D018	**D**escending **018**
DORIS	**D**oppler **O**rbitography and **R**adiopositioning **I**ntegrated by **S**atellite
ECMWF	**E**uropean **C**entre for **M**edium-Range **W**eather **F**orecasts
EFRS	**E**arth-**F**ixed **R**eference **S**ystem
ESA	**E**uropean **S**pace **A**gency
FoV	**F**ield **o**f **V**iew
FRM	**F**iducial **R**eference **M**easurements
GAMIT	**G**NSS **A**t **MIT**
GDR	**G**eophysical **D**ata **R**ecord
GDOP	**G**eometric **D**ilution **o**f **P**recision
GNSS	**G**lobal **N**avigation **S**atellite **S**ystem
GPS	**G**lobal **P**ositioning **S**ytem
GPT	**G**lobal **P**ressure and **T**emperature
IDS	**I**nternational **D**ORIS **S**ervice
IEEE	**I**institue of **E**lectrical and **E**lectronics **E**ngineers
IRS	**I**nertial **R**eference **S**ystem
IWV	**I**ntegrated **W**ater **V**apour
JPL	**J**et **P**ropulsion **L**aboratory
LWC	**L**iquid **W**ater **C**ontent
MERIS	**M**edium **R**esolution **I**maging **S**pectometer
MIT	**M**assachusetts **I**nstitute of **T**echnology
MODIS	**M**oderate **R**esolution **I**maging **S**pectroradiometer
NCEP	**N**ational **C**enter for **E**nvironmental **P**rediction
OLCI	**O**cean and **L**and **C**olour **I**nstrument
OL_2_LFR	**O**cean **L**evel **2** **L**and **F**ull **R**esolution
ORB	**ORB**ital reference system
PDOP	**P**osition **D**ilution **o**f **P**recision
PFAC	**P**ermanent **F**acility for **A**ltimetry **C**alibration
PODS	**P**recise **O**rbit **D**etermination **S**ystem
PPP-AR	**P**recise **P**oint **P**ositioning with **A**mbiguity **R**esolution
PTR	**P**oint **T**arget **R**esponse
PT	**P**oint **T**arget
RF	**R**adio **F**requency
RPY	**R**oll-**P**itch-**Y**aw

SAR	**S**ynthetic **A**perture **R**adar
SAT	**SAT**ellite body reference
SD	**S**tandard **D**eviation
Sentinel-6 MF	Sentinel-6 **M**ichael **F**reilich
SNR	**S**ignal **N**oise **R**atio
STD	**S**lant **T**otal **D**elay
STEC	**S**lant **T**otal **E**lectron **C**ontent
SWOT	**S**urface **O**cean **W**ater **T**opography
TCA	**T**ime of **C**losest **A**pproach
TDOP	**T**ime **D**ilution **o**f **P**recision
USO	**U**ltra-**S**table **O**scillator
VMF1	**V**ienna **M**apping **F**unctions **1**
ZHD	**Z**enith **H**ydrostatic **D**elay
ZTD	**Z**enith **T**otal **D**elay
ZWD	**Z**enith **W**et **D**elay

Physical Constants

Cosmic Microwave Background Temperature	$T_C = 2.725\,48\,\text{K}$
Dry Air Gas Constant	$R_d = 287.04\,\text{J}\,\text{K}^{-1}\,\text{kg}^{-1}$
Dry Air Mean Weight	$m_d = 28.9647\,\text{g}\,\text{mol}^{-1}$
Dry Air Refractivity Constant	$K_1 = 77.604 \times 10^3\,\text{K}\,\text{bar}^{-1}$
Earth Gravitational Acceleration	$g = 9.806\,65\,\text{m}\,\text{s}^{-2}$
Electron Charge	$e = 1.602\,176\,63 \times 10^{-19}\,\text{C}$
Electron Mass	$m_e = 9.109\,383\,7 \times 10^{-28}\,\text{g}$
Gas Constant	$R = 8.314\,462\,6\,\text{J}\,\text{K}^{-1}\,\text{mol}^{-1}$
Planck Constant	$h = 6.626\,070\,15 \times 10^{-34}\,\text{J}\,\text{s}$
Reduced Planck Constant	$\hbar = 1.054\,571\,6 \times 10^{-34}\,\text{J}\,\text{s}$
Speed of Light	$c = 2.997\,924\,58 \times 10^8\,\text{m}\,\text{s}^{-1}$
Vacuum Dielectric Permittivity	$\varepsilon_0 = 8.854\,187\,8 \times 10^{-12}\,\text{F}\,\text{m}^{-1}$
Vacuum Magnetic Permeability	$\mu_0 = 1.256\,637\,1 \times 10^{-6}\,\text{N}\,\text{A}^{-2}$
Water Vapour Gas Constant	$R_w = 461.5\,\text{J}\,\text{K}^{-1}\,\text{kg}^{-1}$

Dedicated to my "roots" Δήμητρα, Καίτη, Κώστα και Μανόλη.

Executive Summary

This dissertation improves calibration of satellite altimeters by strengthening existing procedures, integrating active and passive reference targets, proposing new methodologies and revisiting conventional processing.

External calibration is the only way (post-launch) to assess the accuracy and validity of altimetric products. These products are the starting point for scientific research, interpretation and important decision making that can largely impact society. Thus, calibration should be treated as indispensable element of all operational satellite altimetry missions. About 20 satellite altimetry missions, spanning more than 30 years, provide geophysical parameters that are crucial for Earth observation. Sea level changes are primarily estimated and monitored on a global scale by satellite altimetry. This is performed because the ocean is a regulator of Earth's climate and thus key indicators in understanding climate change.

The altimetric range, used for determining sea surface heights, is continuously monitored for its quality to identify potential instrumental errors, drifts, etc. Continuously monitoring the accuracy, homogeneity, and reliability of altimetric ranges is performed by external and independent facilities dedicated to Calibration/Validation (Cal/Val). The Cal/Val techniques developed for this purpose are generally classified into two main categories: those which rely on reference infrastructures deployed at sea (e.g., buoys) or on coasts (e.g., tide gauges) and those that rely on point reference targets on land (e.g., active transponders and corner reflectors). The present investigation is focused on the latter category, calibration of altimetric ranges using a transponder. It used measurements acquired by two Ku-band microwave transponders of the Permanent Facility for Altimeter Calibration (PFAC) of ESA, installed on Crete (CDN1 site) and Gavdos (GVD1 site) islands. The GVD1 site was completed and inaugurated in October 2021 at approximately the middle of this doctorate dissertation.

In calibration using point targets, the altimeter measurements quality is quantified with the range and datation bias. The range bias is estimated by comparing the altimeter (or measured) range with the corresponding geometric distance (considered the "true" value) between the satellite center of gravity (CoG) and the reflecting point target (microwave transponder or corner reflector). In the context of calibration with a transponder, several corrections need to be applied to the measured and geometric ranges to correctly estimate the altimeter range bias (Mertikas et al., 2020a). The corrections to the initial measured range (i.e., tracker range) are applied partially from the processing agencies and the Cal/Val teams. Conventional corrections applied by the processing agencies account for the offset distance between the altimeter phase center (APC) and satellite CoG, the ultra-stable oscillator (USO) drift, internal path delay, and instrumental and system errors. The corrections applied by the Cal/Val teams to the uncorrected measured range are to account for the effects of the ionosphere and troposphere (atmospheric delays), the transponder internal path delay and Doppler effect as a consequence of the relative velocity of the altimeter satellite with respect to the transponder. Additional corrections are applied to the uncorrected geometric range to account for displacements of the transponder

position caused by tidal and non-tidal effects of atmosphere , solid Earth , pole and ocean loading. Another type of altimetric bias estimated during every calibration is the datation (or time-tagging) bias. This bias describes the error of altimetric measurements time reference (Garcia-Mondéjar et al., 2018). The datation bias equals to the difference between the time of closest approach as estimated using altimetric measurements against this from orbital data.

Although altimeter calibration using a transponder has been proposed in the past (Powell, 1986), its practical implementation has not evolved substantially (Cristea and Moore, 2007; Roca et al., 2013; Fornari et al., 2014; Mertikas et al., 2020b). Therefore, the disadvantages of the conventional calibration using a transponder persisted, and its error sources were not significantly reduced. This realization defined the four research objectives of this dissertation that are provided in the sequel of this Section.

The first objective of this dissertation has been to increase the confidence in determining wet delay. The correction for wet delay is the most variable (spatially and temporally) parameter in calibration and is currently estimated using only one technique based on GNSS. In this dissertation two additional techniques along with GNSS are proposed and implemented, i.e., using the Ocean and Land Colour Instrument on board Sentinel-3A & B satellites and using a ground radiometer installed in CDN1 Cal/Val site. Independent and diverse sources for estimating the wet delay ensures that calibration is successful even in the case of GNSS receiver malfunction. Also, cross-evaluation of independent results for the same parameter allows detection and isolation of outliers and thus increases robustness and confidence of wet delay and bias estimation.

The second objective has been to examine alternative methods of point target calibration to mitigate the major uncertainty in calibration with a transponder, i.e., the knowledge of its internal delay. This dissertation proposes the simultaneous operation of passive targets along with the active transponder in the same calibration network. Thus, the transponder remains the main reference target because of its significantly higher signal to noise ratio while its internal delay is monitored by comparing its echo with this of the passive target. The optimal target according to calibration needs and practical limitations was investigated with analytical computations and simulations. The optimal design is found to be a 1.5 m rectangular trihedral corner reflector consisted of three 5083 aluminum plates connected with honeycomb aluminum. Honeycomb aluminum offers intrinsic structural integrity and removes the need for additional support while forcing contractions and expansions to lengthen rather than wrap the plates.

The third objective has been to improve the accuracy of altimetry calibration with a point target to cover the needs of current missions such as the Surface Water and Ocean Topography (SWOT) and future missions like the Copernicus Polar Ice and Snow Topography Altimeter (CRISTAL). To address this need, a new methodology, called Altimeter Differential Corner Reflector (ADCR) is proposed. The ADCR method is based on co-located corner reflectors with the optimal design described in the second objective. The ADCR introduces a differential bias and offers a quantification of altimeter measurements quality free of the errors of atmospheric delays (i.e., wet, dry and ionospheric delay), geophysical effects (i.e., solid Earth, pole and ocean tides, atmospheric pressure and mass loadings) and orbital errors. The differential bias is defined as the height difference between the two (or more) corner reflectors, as estimated using altimetry measurements minus their corresponding height difference derived using conventional spirit levelling. The co-located targets experience identical atmospheric delays, geophysical displacements and orbital errors and thus

their differential bias is free of these common effects. The targets should be placed at a distance of 100 m along track in order to have separable responses, which can be currently identified by exploiting Fully Focused Synthetic Aperture Radar (Egido and Smith, 2016) processing.

The last objective has been to revisit calibration processing to remove approximations that could degrade the bias accuracy. Conventionally, the reference of measured and geometric ranges was performed by adding a constant offset to the measured range. However, the attitude (i.e., orientation in space) of altimetry satellites during calibration with point targets, affects the relative position between the starting point of measured (APC) and geometrical (CoG) ranges and should be taken into account. This dissertation presents a rigorous processing to reference measured and geometric ranges at the same point on the satellite by adding a vector that incorporates satellites attitude effects. The revised processing was demonstrated on Jason-3. In this case, the correction on range and datation biases from CDN1, fluctuated from -2 mm to $+1$ mm and ± 110 μs, respectively. The magnitude of attitude effects on datation bias corresponds to about 30% of its average value. The implementation of the new processing at the crossover between the ascending (A109) and descending (D018) pass over GVD1, showed an improvement of 12% for Jason-3. The proposed calibration procedure is comprehensive and can be applied to past, current and future missions with available attitude measurements.

The potential outcome of this work is to reach sub-cm accuracy in the calibration of satellite altimeter. This is achieved by removing the influence of systematic effects both in the ground infrastructure (i.e., internal delay knowledge, atmospheric and geophysical corrections) and on the satellite (i.e., internal geometric structure and attitude realization). The next step is the deployment of corner reflectors in PFAC for simultaneous calibrations using active transponders and the corner reflectors. The installation of corner reflectors also allows the implementation of the ADCR approach to determine differential bias.

Chapter 1

Introduction

Human activities over the last centuries increased the concentration of greenhouse gases in the Earth's atmosphere. This led to global warming, ocean acidification, thermal expansion of the sea mass and melting of glaciers and ice sheets. Climate change is a problem that humanity is currently facing and should act to mitigate. The first step towards this direction is to assess environment's current state and forecast its evolution. In order to achieve this, it is necessary to have continuous, indisputable, long and accurate records of oceanic, hydrological, atmospheric and geophysical measurements globally (Plummer, Lecomte, and Doherty, 2017).

One of the most important regulators of Earth's climate and thus key indicator in understanding climate state is the ocean. Sea level is a fundamental environmental parameter as it reflects variations of multiple Earth mechanisms and physical processes (Gornitz, 1995). Additionally, sea level rise is one of the most certain and threatening consequences of climate change (Haigh et al., 2014). A rise of 30 cm would push coastlines inwards by about 30-100 m (Carlowicz, 2015) and thus cause destructive erosion, contamination of freshwater resources, reduction of agricultural soils and floods that endanger human lifes. The importance of sea level for society led to include it into the 50 essential climate variables (ECV) by the Global Climate Observing System (Bojinski et al., 2014) and into the 13 ECVs monitored by the Climate Change Initiative (Hollmann et al., 2013) of the European Space Agency.

Sea level changes are primarily estimated and monitored on global scale by satellite altimetry. About 20 satellite altimetry missions spanning for more than 30 years provide products for various geophysical parameters that are crucial for the majority of Earth observing programs. These geophysical parameters are related to open ocean, near-coast areas, inland waters and ice-caps (Fu and Le Traon, 2006; Vignudelli et al., 2019; Calmant, Crétaux, and Rémy, 2016; Foresta et al., 2016). Some of the altimetric products that are routinely used in geophysical analysis and climate studies are the sea surface height, wave height, wind speed, ionospheric total electron content, sea and land ice coverage and polar region topography (Archer, Li, and Fu, 2020; Timmermans et al., 2020; Abdalla, 2012; Ray, 2020; Rose et al., 2019; Müller et al., 2019). These products are the starting point of a series of scientific research, interpretation and important decision making that largely impact society as presented in the works of Hanson and Nicholls (2020), Cain, Gerber, and Hui (2020), Nazarnia et al. (2020), and Dasgupta et al. (2007).

The aforementioned role of altimetric products, acting as the base of many scientific works and decision making, led to the establishment of the Fundamental Data Records for Altimetry[1]. Fundamental Data Records principles dictate that altimetric data should be *"calibrated and quality controlled"* in order to have a *"long data record*

---

[1] https://www.fdr4alt.org

that is stable spatially and temporally" (Brizzi, 2020). Systematically assessing the accuracy and validity of altimetric products through calibration should be an indispensable element of all operational satellite altimetry missions. But, what is calibration and validation? Calibration[2] is "*the process of quantitatively defining a system's responses to known, controlled signal inputs*". On the other hand, validation is "*the process of assessing, by independent means, the quality [uncertainty] of the data products derived from those system outputs*".

Focusing into altimetry calibration, its principle measurement the range, which is used for the direct calculation of sea surface heights, is continuously monitored for its quality to identify potential instrumental errors, drifts etc. Altimetric ranges of one satellite are also assessed with respect to other missions for identifying relative effects. Continuously monitoring the accuracy, homogeneity, and reliability of altimetric ranges is performed by external and independent facilities dedicated to Cal/Val. The calibration of satellite altimeters involves multiple diverse procedures, such as signal processing, estimation of geophysical corrections or instruments installation and operation. Hence, it is inevitable that the calibration procedures introduce errors that are accumulated and transferred to the bias estimation. Furthermore, the uncertainty of the altimetry bias depends on multiple parameters, such as the instrumentation used, the selected signal processing, the applied geophysical corrections etc. Therefore, different Agencies and calibration sites may produce diverse results.

This created the need for specific guidelines regarding altimetry calibration in order to have traceable bias results from different Agencies that can be compared and combined. This need was covered by the Fiducial Reference Measurements (FRM) strategy (Donlon et al., 2014). FRM describes that: (1) measurements have documented SI traceability, (2) measurements are independent from the satellite geophysical retrieval process, (3) An uncertainty budget for all instruments and derived measurements is available and maintained, (4) measurement protocols and community-wide management practices are defined, published openly and adhered to by instrument deployments and (5) measurements are openly and freely available for independent scrutiny (ESA, 2019). The FRM strategy entails, among other things, reporting of every constituent of uncertainty associated to the calibration process before calculating the final uncertainty of the altimeter bias. The FRM asks for redundancy of scientific instrumentation (different manufacturers, diverse measuring principles, various setups, etc.) and diversity in the techniques and methods followed for the bias estimation. Following these guidelines, every key parameter for altimetry calibration is estimated using different approaches and methodologies.

The Cal/Val techniques developed for satellite altimetry are generally classified into two main categories: those which rely on reference infrastructures deployed at sea (e.g., buoys) or on coasts (e.g., tide gauges) and those that rely on point targets operating on land (e.g., active transponders and corner reflectors). The present analysis is focused on the latter category (i.e., calibration of altimetric ranges using a point target) and uses measurements acquired by two Ku-band microwave transponders of the Permanent Facility for Altimeter Calibration (PFAC) of the European Space Agency (ESA), installed in Crete (CDN1 site) and Gavdos (GVD1 site) islands.

Although altimeter calibration using a transponder has been proposed in the past (Powell, 1986), its practical implementation has not evolved substantially. This is indicated by a systematic review of the literature on satellite altimeter calibration

---

[2]https://ceos.org/

TABLE 1.1: The FRM uncertainty error budget for satellite altimeters calibration with a microwave transponder (Mertikas et al., 2020a).

Error Constituent	Uncertainty Estimate	Standard Uncertainty (Confidence 68%)
GNSS Height	0.13 mm	±0.13 mm
GNSS Receiver	6.00 mm	±3.50 mm
GNSS Antenna Reference Point	2.00 mm	±2.00 mm
Measured Range	3.00 mm	±1.73 mm
Transponder Internal Delay	30.00 mm	±15.00 mm
Dry Tropospheric Delay	2.00 mm	±1.15 mm
Wet Tropospheric Delay	14.00 mm	±8.08 mm
Ionospheric Delay	4.00 mm	±2.31 mm
Geophysical Corrections	20.00 mm	±11.55 mm
Satellite Orbit Height	30.00 mm	±17.32 mm
Pseudo-Doppler Correction	2.00 mm	±2.00 mm
Leveling Instrument/Method	1.00 mm	±1.00 mm
Transponder Leveling	0.50 mm	±0.16 mm
Processing and Approximations	30.00 mm	±17.32 mm
Orbit Interpolations	0.30 mm	±0.17 mm
Unaccounted effects	20.00 mm	±11.55 mm
Root-Sum-Squared Uncertainty		±34.46 mm

using a transponder (Cristea and Moore, 2007; Wei et al., 2011; Hausleitner et al., 2012; Roca et al., 2013; Fornari et al., 2014; Quartly et al., 2018; Mertikas et al., 2020b; Wang et al., 2021). Therefore, the disadvantages of the methodology persisted, and error sources were not significantly reduced. On the contrary, the algorithmic and technological developments increased the accuracy of satellite altimetry measurements over the last decades (Raney, 1998; Griffiths and Purseyyed, 1989; Ray et al., 2014; Egido and Smith, 2016; Raynal et al., 2018; Scagliola and Guccione, 2020; Egido, Dinardo, and Ray, 2021). Indicatively, the root-sum-square accuracy requirement of a single-pass sea level measurement of TOPEX/Poseidon launched in 1992 was approximately 14 cm (Fu et al., 1994) while for Sentinel-6 MF launched in 2020 is around 3 cm (Group, 2019). Thus, the motivation of this work is to advance the calibration of satellite altimeters by mitigating its largest error sources to align it with the improved altimetry measurements. The main error sources that degrade the overall FRM bias (Table 1.1) are the transponder's internal delay and processing and approximations, both with an uncertainty estimate of 30 mm. The satellite orbit height (Table 1.1) induces the same level of uncertainty but is not controlled by the calibration team and hence is out of this dissertation's scope.

Apart from mitigating error sources, this work also strengthens the compatibility of altimetry calibration with FRM standards. In particular, the proposed tandem operation at the PFAC network of diverse (passive and active) instruments, aligns

for the first time the range calibration with the FRM principles. Until now, the the principle measurement of satellite altimetry, the range, was monitored by only one type of instrument (transponder or corner reflector) at a Cal/Val site. Therefore, its calibration did not meet FRM standards that require independent sources for estimating concurrently the same parameter.

    This work increases the reliability and accuracy of satellite altimetry calibration in the context of FRM by:

- **improving existing procedures**. The calibration reliability is increased by adding the Ocean and Land Colour Instrument on board Sentinel-3A & B and the MP–3000A for the wet delay determination along with the existing GNSS following FRM guidelines. The wet delay is the most variable (temporarily and spatially) correction of the calibration. Even short gaps ($\sim$30 minutes) of wet delays estimation can not be recovered, since their accurate modeling from in situ measurements is extremely challenging. Adding sources for wet delays estimation increases the calibration's robustness by assuring its completion even in the case of GNSS receiver malfunction. Moreover, independent results offer the capability of inter-comparison between independent results and thus detection and rejection of possible outliers.

- **proposing new methodology of calibration**. The enhanced calibration technique, combines passive (corner reflectors) and active (microwave transponder) point targets. This combination of targets with diverse signal enhancing allows to independently estimate the transponder's internal delay by comparing its echo with this of the corner reflector. It should be noted that not only the uncertainty of internal delay (Table 1.1) is mitigated but for the first the altimetric range estimation is compatible with FRM standards. This is achieved by measuring the range concurrently ($\simeq$ 11 seconds) with two diverse and independent instruments.

- **introduce novel configuration for altimetry quality control**. A new technique called Altimeter Differential Corner Reflectors is proposed and a differential bias is introduced. This differential bias originates from the comparison of reflectors range difference (estimated using altimeter's measurements) against their known distance. The corner reflectors are co-located to experience identical atmospheric and geophysical effects (Table 1.1). Therefore, the differential bias is free of errors related with estimating common corrections, i.e., wet, dry, ionospheric delays, solid Earth, pole tide etc. The differential calibration configuration does not prevent the extraction of the conventional bias as it is based on post-processing. On the contrary, the additional corner reflectors can be used as independent point targets and increase the number of absolute biases per satellite pass.

- **optimizing processing algorithms**. This work identifies a procedure of conventional processing that degrades the accuracy of calibration using point targets (active and passive) and presents its correction. Evidence for the impact of attitude upon calibration results is the matching frequencies between the attitude angles (i.e., roll, pitch, yaw) and biases of Jason-3 calculated using the CDN1 transponder. The proposed comprehensive methodology incorporates the satellite attitude to rigorously reference the measured and geometrical ranges at the same point. The difference of the aforementioned ranges is defined as range bias. The rigorous common reference of these ranges allows

their accurate comparison and thus correct bias estimation independently of the attitude.

Objectives and Contributions

At the beginning of this doctorate dissertation, the open questions in altimetry calibration were the effect of atmospheric corrections variability on bias, the dependence of transponder calibration upon the knowledge of transponder's internal delay, the uncertainty of absolute calibration and the presence of processing approximations. These unresolved matters led to the research objectives of this dissertation and the purpose of improving satellite altimeters calibration.

To begin with, the first objective was to increase the confidence in estimating the component of tropospheric delay, the most variable parameter both spatially and temporally. The wet delay is currently estimated using only one technique based on GNSS. This work proposed and implemented two additional techniques, i.e., OLCI on-board Sentinel-3 and a ground radiometer installed in CDN1 Cal/Val site. Alternative and independent sources for estimating wet delay increase the robustness of altimetry calibration by assuring its success even in the case of GNSS receiver malfunction and enhance estimation's confidence via cross-evaluating independent results.

The second objective was to examine alternative methods for point target calibration in order to mitigate the major uncertainty in transponder calibration which is the knowledge of transponder's internal delay. This dissertation proposes the integration of active (transponder) and passive (corner reflector) targets at the same calibration network. In this way, the transponder is preserved as the main reference target because of its higher signal to noise ratio while its internal delay is monitored by comparing its echo with this of the corner reflector. The optimal design is found to be a 1.5 m rectangular trihedral corner reflector consisted of three 5083 aluminum plates connected with honeycomb aluminum. The honeycomb aluminum offers intrinsic structural integrity and removes the need for additional supporting structure, while forcing contractions and expansions to lengthen rather than wrap the plates. The preferable location inside the PFAC network for corner reflector has been searched and found. The location offers the capability of calibrating multiple missions (i.e., Sentinel-6 MF, Sentinel-3A and Sentinel-3B), while it has low clutter.

The third objective was to increase accuracy of point target calibration to cover the increased capabilities and thus requirements of recently launched altimetry satellites like the Surface Water and Ocean Topography and future missions such as the Copernicus Polar Ice and Snow Topography Altimeter. To adress this need, this dissertation presents a new calibration methodology called Altimeter Differential Corner Reflector. The ADCR method is based on co-located corner reflectors and the determination of differential bias. The differential bias originates from the comparison of corner reflectors height difference (estimated using altimetry measurements) against their known height difference derived using conventional spirit leveling. The ADCR offers a quantification of altimeter measurements quality, without the uncertainty of atmospheric corrections, geophysical effects because the targets experience identical atmospheric and geophysical effects

The last objective was to examine the conventional calibration processing to reduce the applied approximations and thus reach a more accurate bias. This dissertation detected a common processing approximation, in which the attitude of the satellite is not incorporated into calibration. Specifically, the common reference of measured range, beginning from the altimeter phase center, and geometric range,

beginning from the satellites center of gravity, was performed using a constant off-set. This dissertation presents a revision of the conventional processing, in which the common reference of measured and theoretical ranges is rigorously performed at the same point on the satellite. This was achieved by incorporating attitude measurements from on-board star trackers into the calibration processing. The proposed processing is comprehensive and can be applied to every mission with available attitude information.

Outline

The dissertation is structured as follows. Chapter 2 provides the theoretical background and instrumentation of this work. Specifically, Section 2.1 describes the ESA PFAC infrastructure and site distribution while Section 2.2 provides the fundamental methodology for the calculation of range and datation bias. Section 2.3 focuses into the interaction of atmosphere with altimetric signals and the three techniques of GNSS, OLCI and ground radiometer, used in this dissertation for estimating the atmospheric correction for altimetry calibration. Then, Section 2.4 presents the fundamental methodology of GNSS positioning which is necessary for accurate range and datation bias estimation. Section 2.5 describes the Physical processes that govern the propagation of electromagnetic waves, basic radar theory and the fundamentals of corner reflectors that are proposed as complementary targets to transponders for altimetry calibration. Section 2.6 presented the determination of satellite attitude angles using satellite body quaternions and the optimized calibration processing accounting for satellite orientation. Afterward, Chapter 3 provides the main findings, results and methodologies of my dissertation. In particular, Section 3.1 presents the addition of OLCI and MP-3000A ground radiometer along with GNSS for estimating atmospheric delays and thus the capability of inter-comparison between independent results and alternative sources in case of an instrument malfunction. A new methodology of combining diverse target with active (transponder) and passive (corner reflector) signal enhancement for mitigating the uncertainty of internal delay is presented in Section 3.2. Furthermore, a new methodology of differential calibration with multiple co-located corner reflectors is proposed to obtain a bias free of atmospheric and geophysical estimation errors. Section 3.3 presents the implementation of the calibration accounting for attitude on Jason-3 and the corresponding bias results. Finally, Chapter 4 presents the main conclusions of this work.

Chapter 2

Theoretical Background

2.1 The Cal/Val Infrastructure

The instrumentation used throughout this dissertation is part of the PFAC established by ESA. The ground infrastructure of the PFAC is located in west Crete and Gavdos, Greece (Fig. 2.1). It is dedicated to satellite altimetry calibration and validation (Cal/Val) activities by providing both indirect (sea-surface) and direct (transponder) absolute calibrations of all overflying altimeters. The PFAC is used for relative calibration for both transponder and sea-surface calibration by comparing the biases of different missions and/or satellites. Established in 2004, the PFAC has been delivering bias results for every international altimetry mission, such as Jason-1/2/3, SARAL/AltiKa, HaiYang-2A, B & C, CryoSat-2, Sentinel-3A & B and Sentinel-6 Michael Freilich (Sentinel-6 MF) (Mertikas et al., 2018). It consists of (a) four permanent sea-surface calibration sites, namely the GVD8 Cal/val site on Gavdos island, the CRS1, SUG1 and RDK1 Cal/Val sites in southwest Crete, and (b) two Ku-band (central frequency 13.575 GHz) transponder sites for absolute calibration of satellite altimeters (Mertikas et al., 2020a).

This work is dedicated into the development of direct absolute calibration and thus the methodology and the results regard the two transponder sites. Therefore, further information for only the transponder sites of PFAC network are provided. The first transponder site, named CDN1, is located on a mountainous region at an elevation of about 1050 m in the western part of Crete and has been continuously operating since September 2015. CDN1 from the beginning of its operation, CDN1 transponder site has been used for the calibration of many altimetry missions such as Jason-3, Sentinel-3A & B, CryoSat-2 and for the reference orbits of Jason-3 and Sentinel-6 MF at their descending 018 (D018) pass (Fig. 2.1).

The GVD1 Transponder Cal/Val Site

The second site, named GVD1, was established at about the middle of this PhD, in October 2021, at an elevation of 98 m on Gavdos island. The GVD1 Cal/Val has been continuously operational since its inauguration. The GVD1 transponder site, located on a crossover point of Sentinel-6 MF, provides calibrations for D018 about 11 seconds after the CDN1 calibration of the same pass, and calibrations for the ascending 109 (A109) pass about 5 days after the calibration of D018 (Fig. 2.1). The GVD1 is also used for the calibration of Sentinel-3A and CryoSat-2. Apart from the principal instrument of a transponder, each Cal/Val site is equipped with additional instrumentation required for calibration, such as permanent GNSS stations, meteorological sensors, microwave radiometer, etc. A detailed description of the infrastructure and all geophysical corrections necessary for calibrations can be found in Mertikas et al. (2020a). To further strengthen the operational value and accuracy
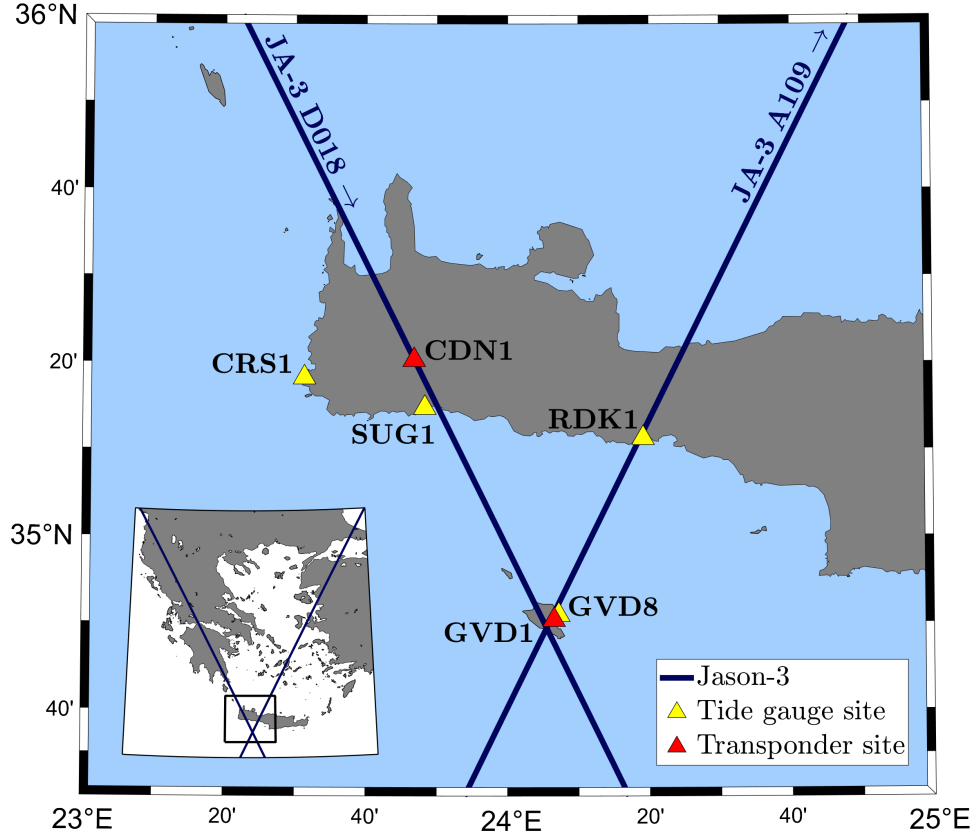
FIGURE 2.1: A map of the PFAC infrastructure with Jason-3 orbits forming a crossover at Gavdos island.

of bias results, a DORIS beacon (Auriol and Tourain, 2010) is planned to be installed in the GVD1 site for the positioning of altimetry satellites.

Both transponder Cal/Val sites are compliant with the strategy of FRM, established by ESA for satellite calibrations (Donlon et al., 2014; Mertikas et al., 2019). For example, transponder coordinates are determined by relative GNSS positioning and precise point positioning, while tropospheric delays are estimated using GNSS observations, radiometers and satellite sensors e.g., the Ocean and Land Color Instrument (OLCI) on board Sentinel-3A & B (Mertikas et al., 2020b).

2.2 Range and Datation Bias

The objective of this dissertation is to reach a more accurate estimation of altimetry measurements quality. In calibration using point targets, the altimeter measurements quality is quantified with the range and datation bias. The range bias of a satellite altimeter represents the systematic error in measuring distances. This bias is estimated by comparing the altimeter (or measured) range with the corresponding geometric distance (considered the "true" value) between the satellite center of gravity (CoG) and the reflecting point target (microwave transponder or corner reflector). The initial estimation of the measured range is typically performed by the altimeter tracker or by a retracking algorithm, and is based on the return waveform as these presented in Figure 2.2. The shape of the return waveform is described by the Brown model (Brown, 1977) over ocean regions and by a point target response (PTR) over

(A)

(B)
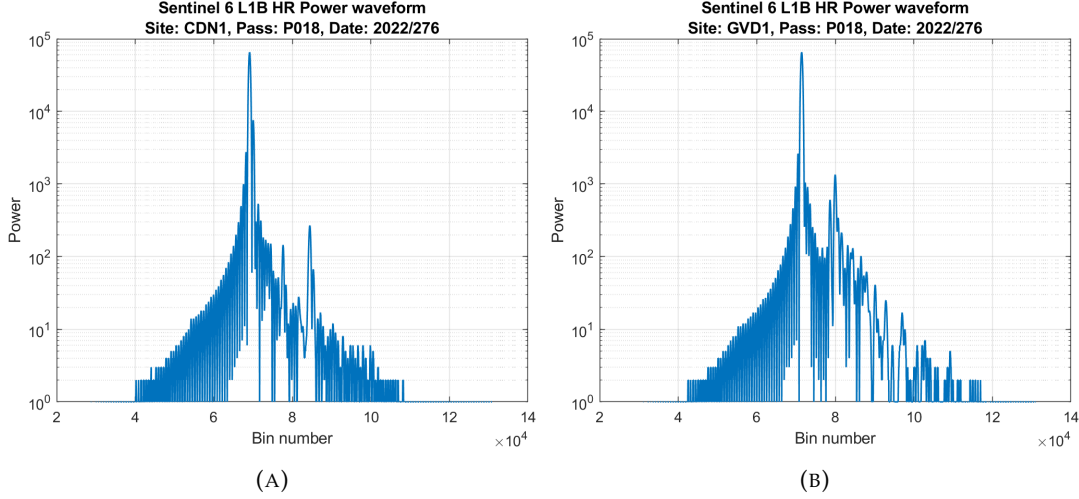
FIGURE 2.2: The waveform of Sentinel-6 MF over (A) the CDN1
transponder and (B) over the GVD1 transponder on DOY = 276 of
2022. The strongest response in both figures originates from the corresponding transponder.

transponders. A profile map of the PFAC transponder sites and the Jason-3 return
waveforms transitioning between a Brown model and a PTR is presented in Fig. 2.3.

In the context of calibration with a transponder, several corrections need to be
applied to the measured and geometric ranges to correctly estimate the altimeter
range bias (Mertikas et al., 2020a). The corrections to the initial measured range (i.e.,
tracker range) are applied partially from the processing agencies and the Cal/Val
teams. Conventional corrections applied by the processing agencies account for
the offset distance between the altimeter phase center (APC) and satellite CoG, the
ultra-stable oscillator (USO) drift, internal path delay, and instrumental and system
errors. The corrections applied by the Cal/Val teams to the uncorrected measured
range ($R^{un}(t)$) are due to the effects of the ionosphere (δr_{iono}) and troposphere (atmospheric delays) (δr_{tropo}), the transponder internal path delay (δr_{TRP}) and the Doppler
effect (δr_{Dop}) as a consequence of the relative velocity of the altimeter satellite with
respect to the transponder. Additional corrections are applied to the uncorrected
geometric range ($r_0^{un}(t)$) to account for displacements of the transponder position
caused by tidal and non-tidal effects of atmosphere (δr_{atmo}), solid Earth (δr_{solid}), pole
(δr_{pole}) and ocean loading (δr_{ocean}). The corrections applied are expressed as:

$$R(t) = R^{un}(t) + \delta r_{iono} + \delta r_{tropo} + \delta r_{TRP} + \delta r_{Dop}, \tag{2.1}$$

$$r_0(t) = r_0^{un}(t) + \delta r_{atmo} + \delta r_{solid} + \delta r_{pole} + \delta r_{ocean}. \tag{2.2}$$

The offset between APC and CoG, also known as "CoG correction", is associated
with satellite attitude. Given the objectives of this dissertation, we isolate this parameter from the rest of the corrections and examine how its current implementation influences bias results. Based on the information given in the beginning of this
section, the range bias $B(t)$ is defined as follows:

$$B(t) = r(t) - r_0(t), \tag{2.3}$$

where $r(t)$ and $r_0(t)$ denote the corrected measured and geometric range, respectively, both of which are referred to the satellite CoG. Since both ranges change as
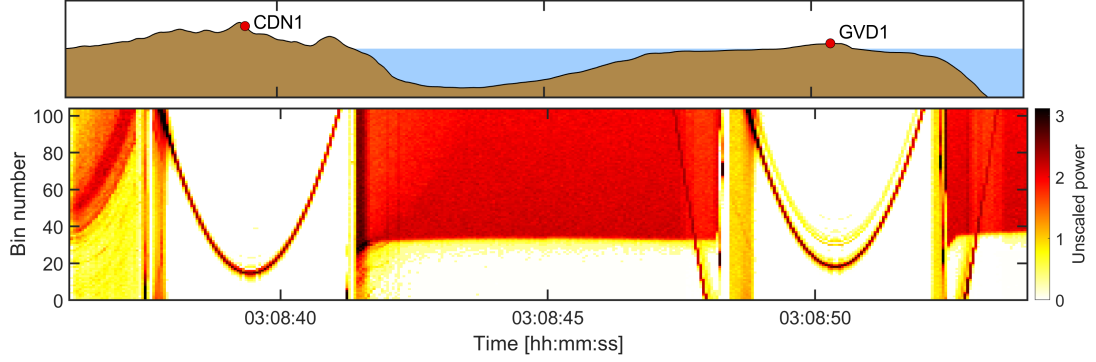
FIGURE 2.3: Topographic and bathymetric profile along the Jason-3 D018 pass, starting from the north with the CDN1 transponder in Crete, passing over the sea region between Crete and Gavdos, and reaching the other GVD1 transponder south in Gavdos. The generated averaged waveforms of the transponder signals are also shown (bottom).

the satellite flies over the transponder, they are functions of time t. The range $r(t)$ is written in terms of the corrected measured range $R(t)$ referred to the APC, as follows:

$$r(t) = R(t) + \delta r, \tag{2.4}$$

with δr being the CoG correction. The corrected geometric range $r_0(t)$ is calculated by:

$$r_0(t) = \sqrt{\left(X^{\mathrm{TRP}} - X^{\mathrm{CoG}}(t)\right)^2 + \left(Y^{\mathrm{TRP}} - Y^{\mathrm{CoG}}(t)\right)^2 + \left(Z^{\mathrm{TRP}} - Z^{\mathrm{CoG}}(t)\right)^2}, \tag{2.5}$$

where (X, Y, Z) are the coordinates of the transponder (superscript TRP) and satellite CoG (superscript CoG) in the Earth-fixed reference system. In Eq. (2.5) it is assumed that the transponder coordinates are constant for a specific cycle.

A second type of bias estimated during the calibration of an altimetric system is the datation (or time-tagging) bias. This bias provides information regarding the error made on the reference time of the altimetric measurements (Garcia-Mondéjar et al., 2018). The definition of datation bias is based on the time of closest approach (TCA), which represents the time at which the distance between transponder and satellite is minimized. Two types of TCA are associated with the calculation of datation bias. The first one is the time at which the corrected measured range is minimized and the second one is the time at which the corrected geometric range is minimized. Since the histories of both ranges form a parabolic curve over a transponder (Fig. 2.3), the two TCAs denote the vertex position of the corresponding parabolas. The datation bias is defined as the difference between the two TCAs, as follows:

$$dt = \underset{t \in \mathbb{R}_+}{\arg \min}\, r(t) - \underset{t \in \mathbb{R}_+}{\arg \min}\, r_0(t), \tag{2.6}$$

where the function $\arg \min_x f(x)$ returns the value of x that minimizes $f(x)$.
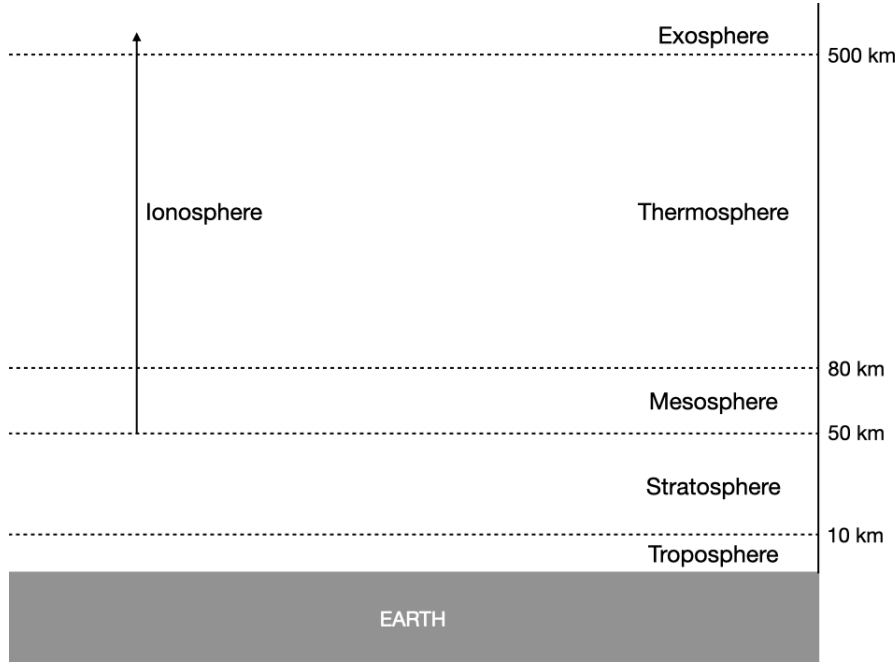
FIGURE 2.4: The layers of Earth's atmosphere and their typical height ranges (*not to scale).

2.3 Atmospheric Effects on Microwaves

A necessary correction applied to every altimetry measurement is to account for the delay on altimetric signals caused by the atmosphere. Therefore, a description of the interaction between atmosphere and electromagnetic signals is provided. The pulses of satellite altimeters propagate through the Earth's atmosphere before they reach the surface of a water mass or a point target in range calibration. Atmospheric effects on altimetry signals are usually interpreted as additional length added to their path. This additional length is known as "atmospheric delays". Thus, the atmospheric delay is added to the length of the straight line that connects the altimeter with the reflecting point in order to estimate the total length of the signal's path.

A more detailed understanding of the physical mechanisms and interactions between the atmosphere and electromagnetic waves from radar altimeters is presented. To begin with, the molecules of the atmosphere (Table 2.1) absorb energy from the signals and thus their speed is reduced. Therefore, a greater amount of time is required to cover the same length in Earth's atmosphere compared to vacuum. Secondly, their trajectory is not the geometrical straight line connecting the altimeter with the target but rather a curved line. This trajectory is caused by the varying refraction indexes at different parts of the atmosphere, which result into fluctuating velocities. The effect of the two previously mentioned effects can be modelled together as a total impact, the atmospheric delay. This length is estimated using the methodologies explained throughout the Sections 2.3.1 – 2.3.1.

The total two-way (from the altimeter to the reflecting surface and back) atmospheric delay is quantified in Chelton et al. (2001) as:

$$\Delta L_{\text{atm}} = L - L_0 = \frac{1}{2} \int_0^{\Delta t} \text{v}(t)\, dt - \frac{c}{2}\, \Delta t = -\frac{c}{2} \int_0^{\Delta t} \left(1 - \frac{\text{v}(t)}{c} \right) dt, \qquad (2.7)$$

where L is the range covered by the signal, Δt is the time that the signal needs to

cover the distance from the satellite to the target and back, c is the speed of light travelling through vacuum, $v(t)$ is the instantaneous speed of altimetric signal. The parameter $L_0 = c\,\Delta t$ is the two-way distance if the signal travelled with speed c. The Equation (2.7) can be expressed alternatively by introducing the refractivity index n = c/v $\geq$ 1. The parameter n is a characteristic of the medium which expresses its opacity and thus the signal's speed reduction. According to Fernandes, Lázaro, and Vieira (2021), the delay of the radar signal equals to:

$$\Delta L_{atm} = -\frac{c}{2} \int_0^{\Delta t} \left(\frac{n-1}{n} \right) dt. \tag{2.8}$$

At this point, the integration parameter is changed from the time t to the signal path z $(dz = (c/n)\,dt)$ and the refractivity index n to the refractivity of the medium N. This is done to express the atmospheric effect in terms of additional path instead of time retardation as:

$$\Delta L_{atm} = -10^6 \int_{z_t}^{z_{sat}} N(z)\,dz = -10^6 \int_{z_t}^{z_{sat}} \left(N_{dry} + N_{vap} + N_{liq} + N_{ion} \right) dz, \tag{2.9}$$

where z_t and z_{sat} are the heights of the surface and satellite respectively. The total refractivity N was divided into individual components of the dry gases (dry), water vapour (vap), liquid water droplets in clouds (liq) and ionospheric (ion) using the corresponding subscripts. Alternatively, there is another more general categorization in which the atmospheric effects are divided into those from the neutral atmosphere (dry, vap and liq) and from the ionized part (ion). The refractivity depends on various meteorological parameters such as temperature, pressure, density of water vapour density of liquid water and density of ions. These meteorological parameters vary strongly both temporally and spatially and thus the refractivity modelling is extremely challenging. Also, the atmosphere absorbs energy from altimetric signals and thus reduces their propagation speed as presented in the sequel.

2.3.1   Neutral Atmosphere

The mechanisms regarding the atmospheric delays caused by the absorption of altimetric signals' energy by neutral atmosphere molecules (Table 2.1) are described. The absorption is mainly governed by three basic Physics principles (Rosenkranz, 1993):

- The Bohr's conditions describe that a photon can be absorbed or emitted if its energy is compatible with the energy difference of two states E_a, E_b of a gas. The absorption results into transition to a state of higher energy while the opposite is true for emission. This equality can be expressed in terms of energy or frequency (ν) by the equation $E_a - E_b = h\nu$, where h is the Planck constant.

- The Einstein's law of emission/absorption defines that the probability of absorbing a photon and moving to a higher energy level (e.g., from a to b) is the same as emitting a photon and passing to a lower energy state (i.e., from b to a). If p_a and p_b are the thermodynamic probabilities of the energy levels, the difference between absorption and emission is analogous to $p_b - p_a$.

- The Dirac's perturbation theory states that passages between two energy levels can only be performed if the corresponding element of the operator is different that zero. For microwave wavelengths, that are of interest for radar altimetry,

TABLE 2.1: Composition of clear Earth's atmosphere at sea level (Hering, 1965). The molecular weight is measured in ^{12}C isotope scale and v/v denotes gas volume/total atmosphere volume.

Gas Name	Gas Symbol	Content v/v %	Molecular weight
Nitrogen	N_2	78.084	28.0134
Oxygen	O_2	20.9476	31.9988
Argon	Ar	0.934	39.948
Carbon Dioxide	CO_2	0.0314	44.00995
Neon	Ne	0.001818	20.183
Helium	He	0.000524	4.0026
Krypton	Kr	0.000114	83.80
Xenon	Xe	0.0000087	131.30
Hydrogen	H_2	0.00005	2.01594
Methane	CH_4	0.0002	16.04303
Nitrous Oxide	N_2O	0.00005	44.0128
Ozone	O_3	$0 - 0.000007$	47.9982
Sulfur Dioxide	SO_2	$0 - 0.0001$	64.0628
Nitrogen Dioxide	NO_2	$0 - 0.000002$	46.0055
Ammonia	NH_3	$0 - $ trace	17.03061
Carbon Monoxide	CO	$0 - $ trace	28.01055
Iodine	I_2	$0 - 000001$	252.8088

the dimensions of atmospheric gases molecules are negligible. Thus, the aforementioned operator is the electric of magnetic dipole moment.

The absorption coefficient $\alpha(\nu)$ can be quantified according to Gordon (1968) and Clarke (1978) as:

$$\alpha(\nu) = \frac{8\pi^3\nu}{3hcV} \sum_{a,b} \delta(\nu_{ab} - \nu)(p_b - p_a) \sum_{\sigma} \frac{|m_{ab}^{\sigma}|^2}{4\pi\epsilon_0}, \qquad (2.10)$$

$$\alpha(\nu) = \frac{8\pi^3\nu}{3hcV} \sum_{a,b} \delta(\nu_{ab} - \nu)(p_b - p_a) \sum_{\sigma} \mu_0 |m_{ab}^{\sigma}|^2, \qquad (2.11)$$

where subscripts a, b are the energy levels, m_{ab}^{σ} is the element that performs the transition from a to b of the matrix m^{σ}. This matrix is a constituent of the molecules' dipole moments (the electric dipole moment divided by $4\pi\epsilon_0$ in Equation (2.10) and the magnetic dipole moment multiplied with μ_0 in Equation (2.11)) in a volume V with $\sigma = [1,3]$. Again p_a, p_b are the thermodynamic probabilities of quantum states a and b respectively, ν is the frequency of the incident wave and δ is the Dirac function. According to Heisenberg's uncertainty law the probability of a transition without a deterministic cause is nonzero and thus a δ function with zero width should not be used. However, in the regime of microwaves for altimetry calibration this possibility

is negligible. We begin by reporting quantum-mechanics principles concerning the interaction of electromagnetic waves with atmosphere and then the specific mechanisms for the O_2 and H_2O molecules are described.

Born-Oppenheimer Approximation

To further present challenge in estimating atmospheric effects on signals the dual nature of nuclei (particle and wave) is briefly presented. In particular, The probability of locating elementary particles (electron or nuclei) is defined by the wave function. A wave function $\mathbf{\Psi}$ dependent on time can be expressed (if there are no external fields or other perturbations, Pauling and Wilson, 2012) as:

$$\mathbf{\Psi} = \psi e^{-iEt/\hbar},\tag{2.12}$$

where $\hbar = h/2\pi$, E is the state's energy and ψ is the solution of the equation (eigenvalues and the corresponding eigenvectors):

$$H\psi = E\psi,\tag{2.13}$$

where H is the Hamiltonian. Generally, the total ψ can be divided into the constituents related with the vibration (ψ_{vib}), rotation (ψ_{rot}), nucleus spin (ψ_{nuc}) and the transnational motion. The specific case of a rigid rotor that is used to model the behaviour of atmosphere molecules is analyzed.

Hamiltonian of a Rigid Rotor

The Hamiltonian of a rigid rotor such as a molecule can be written, according to Townes and Schawlow (2013), as:

$$H_{rot} = \frac{p_x^2}{2I_x} + \frac{p_y^2}{2I_y} + \frac{p_z^2}{2I_z},\tag{2.14}$$

where I_x, I_y, I_z are the inertia moments of the principles body axes and P_x, P_y, P_z the corresponding angular momenta. More details on the solution of the eigenvalues for Schröndinger with Hamiltonian the H_{rot} and the wave functions for atmospheric molecules in microwaves can be found in Herzberg (1950), Strandberg, Johnson, and Eshbach (1954), Gordy, Cook, and Weissberger (1984), and Edmonds (1996).

Moreover, there is interaction between microwaves and ozone (O_3), carbon monoxide (CO), nitrous oxide (N_2O), chlorine monoxide (ClO), ammonia (NH_3), oxygen (O_2) and water vapour (H_2O). The O_2 and H_2O molecules are the major constituents and thus their interaction with microwaves will be shortly described in this dissertation. Detailed analysis of every molecule is provided in the work of Rosenkranz (1993).

Absorption of Microwaves by Oxygen

The oxygen molecule O_2 consists of two oxygen ^{16}O atoms, bond together with a covalent bond (i.e., share two pairs of electrons). Hence, O_2 has the structure of a nobble gas at their outer energy level. The O_2 is a non-polar molecule with two unpaired electron spins. Thus, its interactivity with microwaves originates from the molecule's permanent magnetic moment or in other words its paramagnetic nature. The absorption/emission of microwaves is permitted according to the transitions of
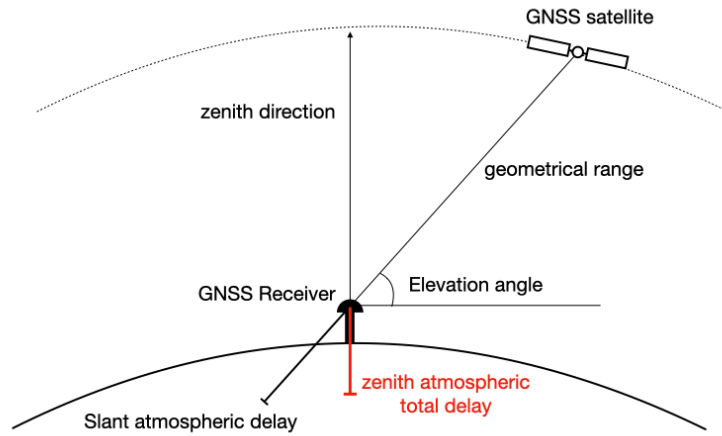
FIGURE 2.5: The additional slant path induced on a GNSS signal by
the atmosphere and its mapping on zenith are presented.

magnetic dipoles, which resonate in microwaves instead of electric states which resonate in ultraviolet (Van Vleck, 1947a). It should be noted that generally the electric effect is stronger than the magnetic one. However, because altimetric signals travel through the whole atmosphere the total delay is at the order of ~ 2 m. This magnitude is caused, because the Ku = 13.575 GHz altimetric signals have a corresponding wavelength of $\lambda \simeq 2.2$ cm, which lies at the vicinity of the resonance maximum (0.5 cm) in microwaves. Detailed analysis of these mechanisms and effects with their formulas can be found in Van Vleck (1947a).

Absorption of Uncondensed Microwaves by Water

The water H_2O is a polar molecule and consists of two hydrogen ^1H and one oxygen atom ^{16}O that are bond with strong hydrogen bonds at an angle of around $105°$. The absorption of microwaves by uncondensed atmospheric water vapours can only be described in quantum mechanics terms. The spin of ^{16}O is zero while each ^1H has $\frac{1}{2}$ with the corresponding eigenvalues being $\pm\frac{1}{2}\hbar$. The wave functions for symmetric and anti-symmetric spins are detailed in (Van Vleck, 1947b; Rosenkranz, 1993). The water vapour interaction in microwaves resonates at 22.235 GHz and 183.310 GHz. The first resonance corresponds to about 1.35 cm which is adjacent to the Ku altimetry signals wavelength of 2.2 cm.

Tropospheric Delays from GNSS

The sequel of this Section will focus on delays by neutral atmosphere determined using the Global Navigation Satellite Systems (GNSS). This technique, based on GNSS, is the main source of tropospheric corrections in satellite altimetry. The neutral part of the Earth's atmosphere is a non-dispersive medium and thus affect equally the GNSS signals with different frequencies. Therefore, the different effects on various frequencies cannot be exploited (as is performed in ionospheric delays) and therefore, build an analytic solution. Hence, to increase the validity of tropospheric delays estimation, multiple independent methodologies are exploited.

Determination of delays caused by neutral atmosphere, which are most commonly referred to as tropospheric delays (because the major contribution comes

TABLE 2.2: The GNSS receivers along with their antennas operating on the PFAC transponder sites are provided.

Location	Code	Receiver	Antenna
Candanos	CDN0	LEICA GR10	Leica AR25
	CDN2	TRIMBLE NETRS	Trimble Zephyr Geodetic
Gavdos	GVD0	Septentrio PolaRx4	Leica AT504
	GVD2	Trimble Alloy	Trimble Ti-V2
	GVD8	Leica GNSS1200	Leica AR25

from troposphere) is primarily determined using GNSS. Therefore, this is the primary way that we use in this work to calculate the tropospheric delays and the corresponding corrections for satellite altimeters calibration. The GNSS receivers along with their antennas that are utilized in PFAC for satellite altimeters calibration are presented in Table 2.2. This selection is justified by the fact it has been tested and proved its accuracy and reliability for many years and in various scientific applications. Some examples are the correction on Synthetic Aperture Radar interferometry (Janssen, Ge, and Rizos, 2004; Bonforte et al., 2001), meteorology studies (Jin et al., 2007; Baldysz et al., 2016; Riccardi, Tammaro, and Capuano, 2021) and the control of measurements from microwave radiometers that operate on altimetry satellites (Desai and Haines, 2004; Edwards, Moore, and King, 2004).

The first step in calculating tropospheric delays using GNSS is to divide the total delay along the zenith (ZTD) into the zenith hydrostatic delay (ZHD) and the zenith wet delay (ZWD). The hydrostatic delay ZHD comprises about the 90% of the total delay, with a mean value of 2.3 m at sea level (Fernandes et al., 2013). The ZHD can be accurately estimated for a station at latitude (ϕ), orthometric height (H) and meteorological measurements of pressure (P) with the Saastamoinen model (Saastamoinen, 1973). The hydrostatic component is provided by processing Agencies such as the European Centre for Medium-Range Weather Forecasts (ECMWF), the United States National Center for Environmental Prediction (NCEP) and the Vienna Mapping Functions 1 (VMF1) ZHD datasets (Boehm and Schuh, 2004). On the other hand, the ZTD has a lower magnitude, at the order of ∼10 cm for PFAC stations. However, is strongly variable both temporally and spatially. Thus, ZTD accurate estimation is extremely challenging. The equation connecting the ZHD, ZTD and the slant total delay (STD) originating from GNSS processing (King and Bock, 2006) is:

$$\text{STD}(E) = \text{ZHD}\, mf_h(E) + \text{ZWD}\, mf_w(E), \tag{2.15}$$

where E denotes the elevation angle of the GNSS satellite that was used for the tropospheric delays estimation and $mf_h(E)$, $mf_w(E)$ are the mapping functions for hydrostatic and wet components respectively. The STD is the delay of the path that connects the receiver with the GNSS satellite through the atmosphere. The mapping functions are crucial because they perform the transformation from the slant delay, which is the observable quantity of GNSS receivers, to the zenith delay, that is the product we use for satellite altimeters calibration (Figure 2.5). The first expression of mapping functions was provided by Marini (1972) with dependence on the elevation angle E of the GNSS satellite and three coefficients, namely a, b and c. The most common mapping functions are based on the original expression of Marini (1972). The differentiation of other approaches lies upon the values of a,b and c and the procedure followed for their calculation. These coefficients can be calculated exploiting

radiosondes data (Niell, 1996), numerical weather models (Niell, 2001; Boehm, Werl, and Schuh, 2006) and climate studies (Boehm and Schuh, 2004).

The ZWD is calculated as the difference between the STD, given by the GNSS processing, and the ZHD can be calculated independently. Particularly, ZHD is estimated according to:

$$\text{ZHD} = 10^{-6} \int_{h_s}^{\infty} N_H(h)\, dh, \tag{2.16}$$

where $N_H(h)$ is the radio refractivity height profile regarding the hydrostatic component of the atmosphere. Using the relation of Davis et al. (1985), Equation (2.16) is transformed into:

$$\text{ZHD} = 10^{-6} K_1 R_d \int_{h_s}^{\infty} \rho(h)\, dh. \tag{2.17}$$

According to Thayer (1974), the refractivity constant for the hydrostatic component (dry air) is $K_1 = 77.604$ K mbar^{-1} and the dry air gas constant R_d has a value of 287.04 J K^{-1}kg^{-1} (Herrmann, Kretzschmar, and Gatley, 2009). The $\rho(h)$ is the density accounting for both water vapour and dry air. The h_s denotes the height of the receiver or in other words the height in which the delays are calculated, and the integration parameter h is the orthometric height (height from the geoid).

The work of Saastamoinen (1972) presented for the first time a closed form of Equation (2.17). This closed form was extracted under the approximation that the atmosphere is an ideal gas and there is hydrostatic equilibrium in an atmospheric column. Moreover, in the work of Davis et al. (1985), the closed form of ZHD proposed is:

$$\text{ZHD} = \frac{K_1 R_d}{10^6 g_m} P_s, \tag{2.18}$$

where P_s is the pressure at the location of the ground receiver and g_m is the gravity acceleration at the center of mass of an atmospheric column. Substituting K_1, R_d constants with the aforementioned values and g_m by the equation given in Saastamoinen (1972) gives:

$$g_m = 98.07(1 - 0.00266\cos(2\phi) - 0.26 \times 10^{-3} h_s), \tag{2.19}$$

the Equation (2.18) can be written as:

$$\text{ZHD} = \frac{0.0022768 P_s}{1 - 0.00266\cos(2\phi) - 0.26 \times 10^{-3} h_s}, \tag{2.20}$$

where ϕ is the latitude of the GNSS receiver and h_s its elevation in meters. The parameters in equations (2.18) – (2.20) are known with high accuracy. Indicatively, each parameter introduces an error of 0.2 mm to 0.4 mm since K_1 is known to 0.018% (Thayer, 1974), R_d to 0.006% (Bosser et al., 2007) and g_m to 0.01% (Davis et al., 1985). Hence, the accuracy of ZHD is strongly dependent upon the P_s in-situ measurements. The equation (2.20) gives the ZHD at the height of the receiver. However, it is necessary to calculate the ZHD and the ZWD at different height for comparing results from different GNSS receivers and/or methodologies (as performed in this work with OLCI and radiometer) a profile of the pressure is necessary. Such an equation provided by Hopfield (1969):

$$P(h_s) = P(h_0) \exp\left(-\frac{g_m(h_s - h_0)}{R_d T_m}\right), \tag{2.21}$$
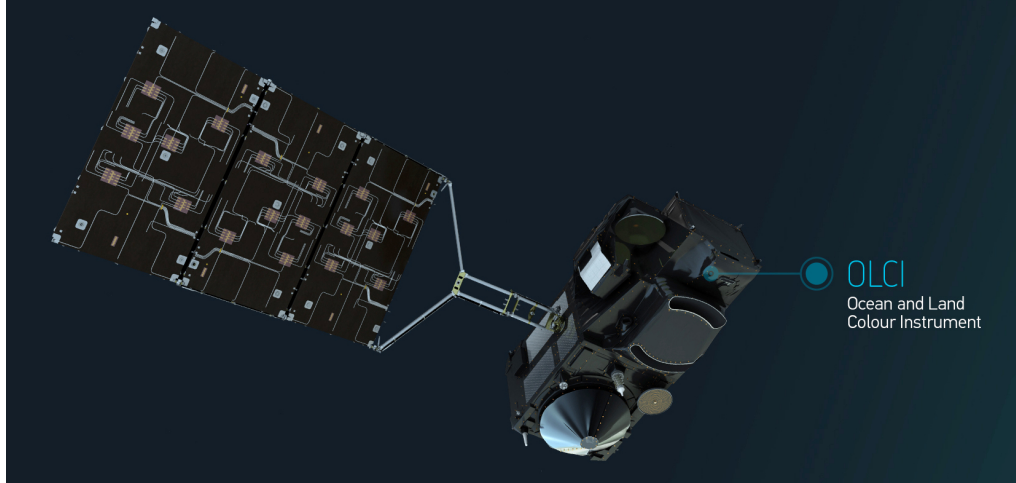
FIGURE 2.6: Position of OLCI on Sentinel-3 spacecraft. Photo credit:
EUMETSAT.

where $P(h_s)$, $P(h_0)$ are the pressures at heights h_s and h_0 respectively and T_m denotes the mean difference between the temperatures at h_s and h_0. The parameter T_m can be estimated assuming a gradient of -0.065 K/m from the mean sea level with temperature T_0. The latter parameter is provided by the Global Pressure and Temperature (GPT) model (Boehm and Schuh, 2004).

Tropospheric Delays from OLCI

An alternative for wet delays estimation used in this dissertation is based on OLCI. The OLCI is part of the scientific payload on-board the Copernicus Sentinel-3 satellites. Sentinel series is comprised of Sentinel-3A & B that are currently operational and the upcoming Sentinel-3C & D, planned to be launched in 2024 and 2028 respectively. In the framework of this work, OLCI was exploited as an additional way to determine ZWD for calibration of satellite altimeters.

OLCI is a multi-spectral imaging spectrometer with a push broom measuring capability, observing from the visible to the near-infrared spectrum (400 - 1020 nm). It is the successor of the ENVISAT's Medium Resolution Imaging spectrometer (MERIS) that assures the continuity of ocean color data records. OLCI is based on the opto-mechanical design of MERIS but is equipped with crucial upgrades. Specifically, OLCI has an increased number of spectral channels, optimized camera arrangement and reduced load of on-board processing. Elaborating on the improvements, the spectral bands of OLCI increased to 21 compared to 15 of MERIS (Table 2.3), the repeat cycle reduced from 15 days of MERIS to less than four days for ocean and three days for land observations and progressed to 14-bit analogue to digital converter which resulted into a delivery time of approximately three hours for Level-2 products.

Another improvement of OLCI compared to MERIS is the reduced contamination of measurements from sun glint. This was achieved by tilting the cameras 12.6° away from the sun. Each of the five OLCI cameras has 14.2° Field of View (FoV) with 0.6° in-between overlap. Therefore, OLCI total FoV equals to 68.6°. The total coverage of OLCI (ground swath) is approximately 1270 km with a spatial resolution of 300 m independently of the targeted surface. This resolution is the instrument's native full resolution while there are 1B level products with reduced resolution of 1.2

TABLE 2.3: The wavelength bands of OLCI on-board Sentinel-3, are presented along with their main applications. The additional bands of OLCI compared to MERIS are denoted with bold font. (Donlon et al., 2012)

Band #	λ center (nm)	Width (nm)	Application
Oa1	**400**	**15**	Aerosol correction
Oa2	412.5	10	Yellow substance pigments
Oa3	442.5	10	Biochemistry
Oa4	490	10	High Chlorophyll
Oa5	510	10	Red tides
Oa6	560	10	Chlorophyll reference
Oa7	620	10	Sediment loading
Oa8	665	10	Chlorophyll 2nd absorption
Oa9	**673,75**	**7.5**	Fluorescence retrieval
Oa10	681.25	7.5	Chlorophyll fluorescence peak
Oa11	708.75	10	Chlorophyll fluorescence reference
Oa12	753.75	7.5	O_2 absorption
Oa13	761.25	2.5	O_2 absorption band
Oa14	**764.375**	**3.75**	Atmospheric correction
Oa15	**767.5**	**2.5**	Fluorescence over land
Oa16	778.75	15	Atmospheric and aerosol correction
Oa17	865	20	Pixel co-registration
Oa18	885	10	Water vapour absorption reference
Oa19	900	10	Water vapour absorption
Oa20	**940**	**20**	Water vapour absorption
Oa21	**1020**	**40**	Atmospheric and aerosol correction

km. More details about OLCI products can be found in Bourg et al. (2021). There is a dedicated Charge Couple Device (CCD) at each camera with 384000 pixels that are translated into 740 ground pixels spanning from 390 nm to 1040 nm (Team, 2016). The OLCI operating schedule includes recurrent on-board calibrations regarding radiometric and spectral characteristics to assure measurements' reliability (Lamquin et al., 2020).

The OLCI spectrometer is exploited for numerous applications such as aerosol correction biochemistry, turbidity estimation, red tide, chlorophyll fluorescence peak, O_2 absorption, maximum reflectance of vegetation (Table 2.3). In this work the OLCI was used for the determination of the water (H_2O) vapour absorption in the context of satellite altimeter calibration. The integrated water vapour (IWV) retrieval was performed using the different absorption methodology between the reference water vapour band Oa18 with central wavelength 885 nm and the non-affected Oa19 with central wavelength 900 nm (Borel and Schlaepfer, 1996). The measured radiance is

affected by solar radiance, transmittance of the atmosphere and the reflected radiation from the surface (ignoring diffusion phenomena). Hence, the IWV in kg/m^2 can be estimated by (Leinweber, 2010):

$$\text{IWV} = -\frac{1}{k_{19}}\ln\left(\frac{L_{19}}{L_{18}}\right), \qquad (2.22)$$

where L_{19} and L_{18} is the measured spectral radiance at Oa18 and Oa19 bands and k_{19} is the water vapour mass coefficient at Oa19 retrieved following the procedure described in Fischer, Leinweber, and Preusker (2010). The necessary data regarding OLCI observations over Crete were acquired from the Copernicus Open Hub [1].

Tropospheric Delays from Ground Radiometer

The second alternative implemented for wet delays estimation is based on a ground microwave radiometer installed in CDN1 Cal/Val/site. This technique will be described at this section. Generally, radiometry is a passive remote sensing technique for the measurement of the emitted energy (radiant and thermal) by materials and media. These direct measurements realized by instruments such as microwave radiometers are used for the estimation of various parameters. Some examples are soil moisture (Le Vine and Skou, 2006), show-pack characteristics (Rango, Chang, and Foster, 1979), Earth's surface materials (Grody, 1988) and temperature profiles (Askne and Westwater, 1986).

Microwave radiometers are extensively used on altimetry satellite missions for the calculation of wet delays correction that should be applied on range measurements over ocean. Some examples of altimetry satellites exploiting a radiometer are the TOPEX-Poseidon (Ruf et al., 1994), Jason-1 (Obligis, Tran, and Eymard, 2004), OSTM/Jason-2 (Sibthorpe et al., 2011), Jason-3 (Maiwald et al., 2016), CryoSat-2 (Fernandes, Nunes, and Lázaro, 2013), Haiyang-2B (Zhang et al., 2020), Sentinel-3A (Fernandes and Lázaro, 2018) and Sentinel-3B (Picard et al., 2020). A significant improvement on the radiometer design and thus measurement accuracy has been performed in Sentinel-6 MF. More details on this can be found in (Kloosterman et al., 2017). It should be noted that the wet delays determined by on-board radiometers can be directly applied to satellite altimeters operating at Ku = 13.575 GHz and/or Ka = 35 GHz, since the effect of neutral atmosphere is practically the same for signals between 0 - 100 GHz (Crane, 1976).

As previously mentioned, the wet delays calculation is challenging because of their strong variability over time and space. They depend on micro-physical processes such as the cloud's drop radius, concentration, and distribution (Wallace and Hobbs, 2006). Thus, to strengthen the reliability of wet delays estimation for calibration needs, we inserted an additional methodology based on a ground microwave radiometer operating at CDN1 transponder site. Specifically, the radiometer that was used is the MP–3000A from the Radiometrics Corporation. The MP–3000A ground radiometer is mainly used for temperature, relative humidity, and water vapour profiles estimation and secondly for liquid profiles (with lower resolution). This instrument includes two Radio Frequency (RF) units that share the same antenna system (Figure 2.7). The first RF component, which is used for temperature profiling, observes at the frequency bandwidth between 51 and 59 GHz while the second, dedicated to water vapour, between 22 and 30 GHz as presented in Table

---

[1] https://scihub.copernicus.eu/
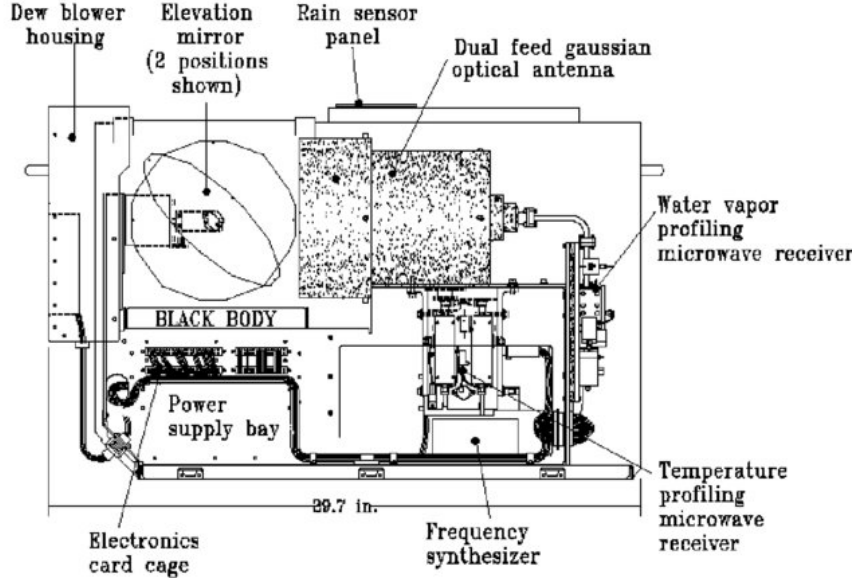
FIGURE 2.7: Cross section of the MP3000 ground radiometer. Photo credit: Radiometrics Corporation.

2.4. The added length (L) which is induced into microwaves is expressed as:

$$L = 10^{-6} \int_0^{\infty} N(h) \, dh, \tag{2.23}$$

where $N(h)$ is the air refractivity as a function of height h. The refractivity of air is given in the work of Bean and Dutton (1966) as:

$$N = \frac{77.6}{T} \left(P + \frac{4810 \, e}{T} \right), \tag{2.24}$$

where T is the temperature measured in Kelvin (K), P the pressure in millibars (mb) and e the partial water vapour pressure in mb. The first term of the right part of Equation (2.24) is called "dry term" and originates from air polarization, while the second, the "wet term", from the water vapour dipole moments (Moran and Rosen, 1981). Similarly, the refractivity can be divided into its dry (N_D) and wet (N_W) constituents. Approximating the behavior of atmosphere in microwaves as this of an ideal gas (Liebe, 1969), N_D and N_W can be expressed as:

$$N_D = \frac{77.6P}{T} = 2.7 \times 10^4 \, \rho_D, \tag{2.25}$$

$$N_W = \frac{3.73 \times 10^5 e}{T^2} = 1.72 \times 10^3 \, \frac{\rho_W}{T}, \tag{2.26}$$

with ρ_D and ρ_W denoting the density of dry air and water vapour, respectively. The coefficients in equations (2.25) and (2.26) correspond to densities measured in gr/cm^3. The additional path caused by the dry constituent is accurately modeled, under the approximation of hydrostatic equilibrium over an atmospheric column, as:

$$L_D = 10^6 \int_0^{\infty} N_D \, dh = \frac{77.6R}{gm} P_0, \tag{2.27}$$

TABLE 2.4: The specifications of MP–3000A microwave radiometer
as reported in Radiometrics (2008).

Parameter	Specification
Long term stability	< 1.0 K/yr
Brightness Temperature Resolution	0.1 to 1 K
Brightness Temperature Range	0 – 400 K
Antenna System Resolution at 22-30 GHz	4.9° – 6.3°
Antenna System Resolution at 51-59 GHz	2.4° – 2.5°
Antenna System Resolution at 170-184 GHz	1.0° – 1.1°
Integration Time (10 ms increments)	0.01 – 2.5 s
Low Water Vapour Band	K band (22.0 – 30.0 GHz)
Oxygen Band	V band (51.0 – 59.0 GHz)
Standard calibrated channels	35
Surface Temperature Accuracy	0.5 °C at 25 °C
Surface Barometric Pressure Accuracy	0.3 mb
Surface Relative Humidity Accuracy	2%

where P_0 is the surface pressure, R is the gas constant, g is the gravity acceleration at Earth's surface and m the mean weight of dry air molecules. Thus, it is evident from Equation (2.27) that the accuracy of L_D depends only upon the accuracy of measuring P_0, after the approximation of ideal gas and hydrostatic equilibrium and assuming that constants are accurately known. The accuracy of L_D is at the order of ~1 cm which originates from a measurement accuracy of a few millibars for P_0 (Hopfield, 1971). In other terms, L_D relative accuracy with a mean value for dry delay at 2.3 m is around 0.4% (Fernandes, Nunes, and Lázaro, 2013).

The additional path L_W caused by the wet constituent can be expressed using Equation (2.26) and substituting $\rho_W = 217e/T$ (again under the approximation of ideal gas) by:

$$L_W = 1.72 \times 10^3 \int_0^\infty \frac{\rho_w(h)}{T(h)} \, dh = 3.73 \times 10^5 \int_0^\infty \frac{e(h)}{T(h)^2} \, dh, \qquad (2.28)$$

where $\rho_W(h)$ and $T(h)$ are the height h profiles of water vapour density and temperature respectively.

The objective of ground microwave radiometers is to calculate the absorption losses of atmosphere with measurements from Earth's surface. This is realized by using the radiative transfer along the Earth's atmosphere. The radiative transfer is described in Goody and Yung (1995), while its effect on radiometry is analyzed in Ulaby, Moore, and Fung (1981), Janssen (1994), and Petty (2006). Microwave radiometer brightness temperature T_b is related with thermal emissions. Analytically, $T_b(f)$ depends on the frequency f, the polarization of the electromagnetic waves and the observing elevation angle θ. However, in this work the observing angle was kept constant at $\theta = 90°$, because it is dedicated to nadir looking satellite altimeters. According to Chandrasekhar (2013) the brightness temperature T_b along

the path h toward zenith, is dependent upon the atmosphere absorption (assuming non-scattering mechanisms), as described by the Radiative Transfer Equation (RTE) (Chandrasekhar, 2013; Ulaby, Moore, and Fung, 1981):

$$T_b(f) = T_c \, e^{-\tau_f(0,\infty)} + \int_0^\infty T(z) \, a(f,z) \, e^{-\tau_f(0,z)} \, dz. \tag{2.29}$$

The first term of Equation (2.29) describes the radiation from the cosmic microwave background that equals to $T_c = 2.72548 \pm 0.00057$ K (Fixsen, 2009) and $\tau_f(0,\infty)$ is the total optical path at frequency f. The $a(f,z)$ is the absorption coefficient at z with frequency f and $T(z)$ is the temperature at z, which is the coordinate along the zenith of the emitting/absorbing atmospheric volume. Finally, $\tau_f(0,z)$ is the optical path from the Earth's surface up to height z. The latter term is also known as opacity.

The mean radiating temperature T_m can be related with brightness temperature $T_b(f)$ as:

$$T_m(f) = \frac{\int_0^\infty T(z) \, a(f,z) \, e^{-\tau_f(0,z)} \, dz}{\int_0^\infty a(f,z) \, e^{-\tau_f(0,z)} \, dz}. \tag{2.30}$$

Substituting Equation (2.30) into (2.29) gives for RTE the expression:

$$T_b(f) = T_c \, e^{-\tau_f(0,\infty)} + T_m(1 - e^{-\tau(f)}), \tag{2.31}$$

where $\tau(f)$ denotes the atmospheric opacity. Under the assumption of low attenuation in which:

$$e^{-\tau(f)} = 1 - \tau(f), \tag{2.32}$$

the opacity can be expressed as:

$$\tau(f) = \ln\left(\frac{T_m(f) - T_c}{T_m(f) - T_b(f)}\right). \tag{2.33}$$

The Equation (2.33) connects the direct measurement T_b of microwave radiometers with the total radiometric attenuation $\tau(f)$. The accuracy of opacity determination does not only depend on brightness temperatures measurements but also on T_m estimation (Basili, Ciotti, and Fionda, 1998).

The first observing frequency of the microwave radiometer MP–3000A at CDN1 Cal/Val site is 23.8 GHz (corresponds to total attenuation τ_1) and the second is 31.4 GHZ (corresponds to total attenuation τ_2). The first channel is mainly affected by water vapour, while the second one by liquid water absorption. Tropospheric IWV and Liquid Water Content (LWC) can be estimated using the linear equations (Westwater and Guiraud, 1980):

$$\text{IWV} = \alpha_0 + \alpha_1 \tau_1 + \alpha_2 \tau_2, \tag{2.34}$$

$$\text{LWC} = \beta_0 + \beta_1 \tau_1 + \beta_2 \tau_2, \tag{2.35}$$

where α_k and β_k with $k \in \{0,1,2\}$ are the retrieval coefficients. These combined with τ_1 and τ_2 are used to determine IWV and LWC respectively (Basili, Ciotti, and Fionda, 1998; Basili et al., 2001; Westwater and Guiraud, 1980). The retrieval coefficients are determined using radiative transfer theory, applied to a large dataset of radiosondes measurements (Schroeder and Westwater, 1991). Hence, a microwave radiometer with observing channels near 23 GHZ and 31 GHZ can be used to estimate IWV and LWC, as demonstrated in Ulaby, Moore, and Fung (1981), Fionda,

Falls, and Westwater (1991) and Barbaliscia, Fionda, and Masullo (1998).

Finally, the linear relation proposed in Shangguan et al. (2015) is used for determining ZWD (which is the parameter of interest in altimetry calibration) from the IWV (which is estimated by the microwave radiometer).

$$\text{ZWD} = \frac{1}{\pi}\text{IWV} = \frac{\rho R_w (C_1/T_w + C_2)}{10^6}\,\text{IWV}, \tag{2.36}$$

where π is the atmosphere conversion coefficient, $\rho = 1$ gr cm^{-3} is the density of water, $R_w = 0.4615$ NmK^{-1} the gas constant for water vapour, $C_1 = 3.776 \times 10^5$ K^2 hPa^{-1} and $C_2 = 22.10$ K hPa^{-1} are refractivity coefficients and T_w is the atmosphere weighted mean temperature (Askne and Nordius, 1987; Davis et al., 1985; Duan et al., 1996). Given that the surface temperature T_s is known, T_w can be determined with 2% accuracy by (Bevis et al., 1994):

$$T_w = 70.20 + 0.72\,T_s. \tag{2.37}$$

2.3.2 Ionosphere

The description of ionospheric delays is provided in this Section for completion purposes, even though there was not performed any analysis in this dissertation. The ionosphere is the ionized part of the Earth's atmosphere that extends roughly from 50 to 950 km above sea level. This layer covers part of the mesosphere, the thermosphere, and the beginning of the exosphere. The exact limit of ionosphere is variable, since it depends on the location, the season, and also on the time of the day, which can be summarized in the parameter of solar activity. During the daylight, the ionosphere becomes larger as the Sun's radiation ionizes more molecules and then lessens during night. The ionosphere's dispersive characteristic needs to be explained in order to understand the effect of ionosphere on microwave signals.

Dispersive Medium

An electromagnetic wave with frequency f propagating through a medium such as the atmosphere, has two distinct types of velocities. As presented in Figure 2.8, the phase velocity (u_{ph}) expresses the velocity of a single sinusoidal wave traveling through the medium whereas the velocity with which the wave-packet moves is called group velocity (u_{gr}). A medium that causes divergence between the phase and group velocities is called dispersive. The aforementioned definitions of phase and group velocities also emerge from the equation of a wave travelling along the direction x as function of time t. Such an expression is:

$$\phi(x,t) = e^{i(kx - \omega t)}, \tag{2.38}$$

where ω is the angular frequency and k is the wavenumber. The group and phase velocity are:

$$u_{ph} = \frac{\omega}{k} \tag{2.39}$$

$$u_{gr} = \frac{d\omega}{dk}. \tag{2.40}$$

According to Hofmann-Wellenhof, Lichtenegger, and Collins (2012) the relation between the refractive index regarding phase velocity (n_{ph}) and group velocity (n_{gr}) is:
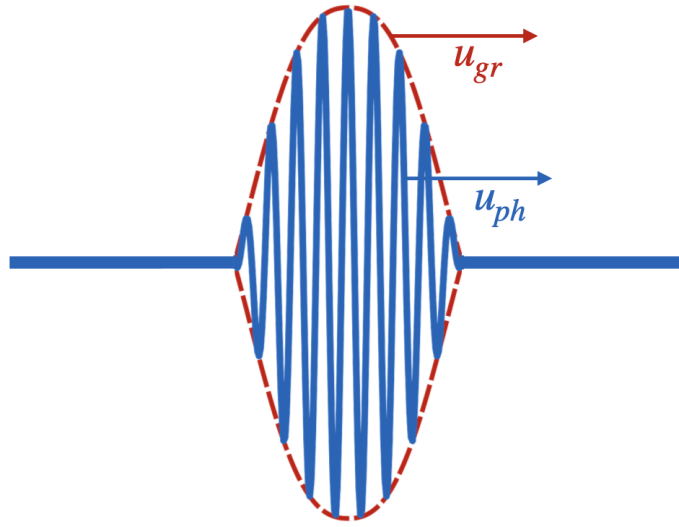
FIGURE 2.8: The phase and group velocity of an electromagnetic wave are denoted with different colors.

$$n_{gr} = n_{ph} + f \frac{dn_{ph}}{df}. \tag{2.41}$$

Ionospheric Delays from GNSS

The measured range s across a medium with refraction index n is (Born and Wolf, 2013):

$$s = \int n \, ds, \tag{2.42}$$

where the integration is performed along the signal's propagation path. The ionospheric delay (ΔL_{ion}) is defined as:

$$\Delta L_{ion} = \int n \, ds - \int ds_0, \tag{2.43}$$

where the second term of the equation's right side is the geometrical range between the satellite and the receiver which is realized in vacuum with $n=1$. Under the assumption that the curve of the altimetric signal's path is negligible and the integration parameter is along the geometrical range s_0, the ionospheric phase delay can be expressed as (Tucker and Fannin, 1968; Hartmann and Leitinger, 1984; Budden, 1988; Alizadeh et al., 2011):

$$\Delta L_{ion} = -\frac{C_X}{2f^2} \int N_e \, ds_0 - \frac{C_X C_Y}{2F^3} \int N_e \, B_0 \cos\theta \, ds_0 - \frac{C_X^2}{8f^4} \int N_e^2 \, ds_0, \tag{2.44}$$

where N_e is the electrons density, θ is the angle between the vectors of the magnetic field and the propagating wave, B_0 is the magnitude of the magnetic field and C_X, C_X are equal to (Brunner and Gu, 1991):

$$C_X = \frac{e^2}{4\pi \epsilon_0 \, m_e}, \tag{2.45}$$

$$C_Y = \frac{\mu_0 e}{2\pi \, m_e}, \tag{2.46}$$

where m_e is the electron's mass, e is the electron's charge, ϵ_0 is the vacuum dielectric permittivity and μ_0 denotes the vacuum magnetic permeability. In the framework of satellite altimetry we focus on the delay of first order in Equation (2.44):

$$\Delta L^1_{ion} = -\frac{C_X}{2f^2} \int N_e \, ds_0, \tag{2.47}$$

by substituting the value of C_X the group ionospheric delay in meters can be expressed as:

$$\Delta L^1_{ion} = \frac{40.31}{f^2} \int N_e \, ds_0. \tag{2.48}$$

The integral of Equation (2.48) is the Slant Total Electron Content (STEC) since the density integration is performed along the propagation path. Thus, the phase ionospheric delay can be expressed as:

$$\Delta L^1_{ion} = \frac{40.31}{f^2} \text{STEC}. \tag{2.49}$$

Equation (2.49) manifests the relation between delay and frequency. In particular, the delay is inversely proportional to the square of the signal's frequency.

There was not performed any further analysis regarding the ionospheric delays because they are analytically calculated using GNSS receivers. However, the description of ionospheric delays is included in this work for completeness. This correction for altimetry calibration is initially calculated using the L_1 = 1575.42 MHz and L_2 = 1227.60 MHz frequencies of GNSS (Katzberg and Garrison Jr, 1996; Brunner and Gu, 1991; Komjathy and Born, 1999; Alizadeh et al., 2011; Lin et al., 2022) and then transformed for estimating the corresponding delay for satellite altimeters. The altimeters frequency can be Ku = 13.575 GHz, e.g., Jason-3, Sentinel-3A & B, Sentinel-6 MF or Ka for the Surface Water and Ocean Topography. The ionospheric delay is at the order of $\sim$10 – 20 cm for CDN1 and GVD1 transponder locations.

Over open ocean the ionospheric delay correction on altimeter's range measurement are calculated similarly exploiting the two diverse frequencies of the altimeter (Imel, 1994; Le Roy et al., 2007; Meloni et al., 2015; Scharroo et al., 2016). In particular, the altimeters frequencies are Ku = 13.575 GHz and C = 5.41 GHz for Sentinel-3A & B and Ku = 13.575 GHz and C = 5.3 GHz for Jason-3. On the other hand, for satellite with altimeters that operate solely in one bandwidth the ionospheric correction is based on datasets built using GNSS observations. For example, the Cryosat-2 altimeter that operates only at Ku exploits the Global Ionosphere Maps of TEC from the Jet Propulsion Laboratory (Iijima et al., 1999).

2.4 GNSS Positioning

The determination of point targets (active microwave transponder or corner reflector) absolute position is crucial for satellite altimeters calibration. In particular, the coordinates are directly used to calculate the geometrical distance between the reflecting target and the satellite altimeter and indirectly to estimate atmospheric delays through GNSS processing. In the sequel of this section, the general concept of positioning targets on Earth using GNSS is described. The GNSS solution is performed under the assumption that the position of satellites and GNSS receiver are constant during the travel time of the signal from the satellite to the ground receiver.
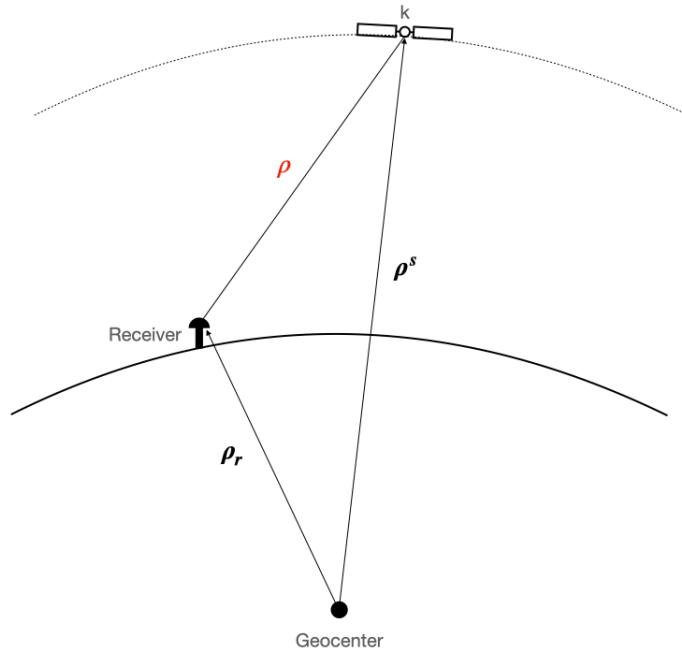
FIGURE 2.9: General concept of positioning based on satellites.

This approximation is justified by the fact that the relative motion between the satellites and the receiver is negligible compared to the speed of light through atmosphere. The range equation of GNSS positioning is:

$$\rho = ||\, \rho^s - \rho_r \,||, \tag{2.50}$$

In Equation 2.50, the space vector ρ^s connecting the Earth's center (geocenter) with the satellite's center of gravity is computed using the navigational message sent by the satellite. The range (geometrical range ρ) between the receiver, with radial position vector ρ_r, and the satellite is determined using the recorded time it takes the coded distance to cover their distance (Figure 2.9). The interception of three spheres' surfaces that are created between the receiver and each one of the three GNSS satellites, can be used to calculate the three unknown variables (X, Y, Z) of the user's position.

However, the above approach presupposes that synchronization of receiver's clock with the system time is absolute, with zero offset. Obviously, this is not a realistic approximation, because receivers use low-cost crystal clocks with limited quality. These clocks induce a substantial time offset which leads to incorrect estimation for the geometrical range. Therefore, for the measured ranges R the term pseudoranges is introduced since there is a difference $\Delta\rho$ with the true range. The offset $\Delta\rho$ can be expressed in terms of time, as bias δ of the user's clock multiplied by the speed of light c. Thus, the model is transformed as:

$$R = \rho + \Delta\rho = \rho + c\delta. \tag{2.51}$$

There are actually four unknown parameters involved in positioning, which are the longitude, latitude, height and δ. Hence, simultaneous observations from at least four GNSS satellites are required for the determination of a user's position. It should be noted that the positioning accuracy is mainly affected by the accuracy of satellite position, the accuracy of pseudoranges calculation and the geometry of the satellites
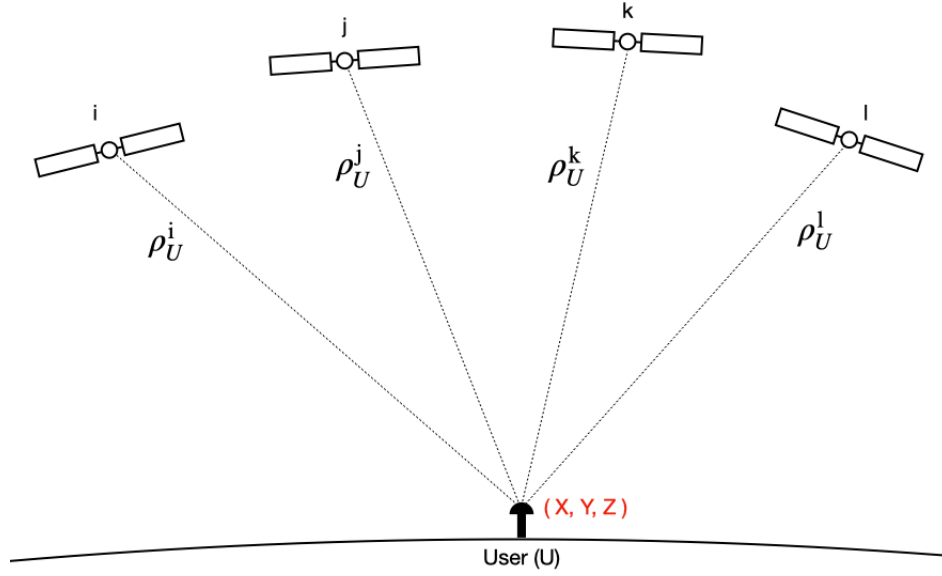
FIGURE 2.10: In point positioning the determination of user's coordinates (X, Y, Z) is based exclusively on GNSS satellites. The pseudoranges ρ connecting a GNSS satellite and the User are presented.

used. The latter can be expressed by the geometric dilution of precision (GDOP), the position dilution of precision (PDOP) and the time dilution of precision (TDOP). The parameter GDOP is inversely proportional to the pentahedron's volume created by the vectors connecting the user with the satellites. From a mathematical point of view, bigger volume of this imaginary body results into lower statistical correlation between the four pseudorange equations. A system of equations with lower correlation entails higher level of information. However, there is a limit on the volume of the pentahedron that is set by the elevation cut-off angle. This cut-off is performed because satellites with elevation lower than the cut-off angle have degraded signals because of the longer traveled path through the Earth's atmosphere.

2.4.1   Precise Point Positioning

In point positioning the unknown coordinates of a receiver are calculated using exclusively GNSS satellites (Figure 2.10). The differentiation and advantage of precise compared to conventional point positioning is that certain sources of error are limited and thus positioning accuracy is increased. The major factors influencing positioning are the satellite orbit errors, clock errors and atmospheric effects (i.e., ionospheric and tropospheric refraction). To mitigate these errors, in precise point positioning accurate orbital and satellite clock parameters, dual-frequency code pseudoranges and carrier phase observations are exploited. Beginning with the code pseudoranges equation (Hofmann-Wellenhof, Lichtenegger, and Collins, 2012):

$$\left[R_1 - \frac{f_2^2}{f_1^2} R_2 \right] \frac{f_1^2}{f_1^2 - f_2^2} = \rho + c\,\Delta\delta + \Delta^{\text{Trop}}, \tag{2.52}$$
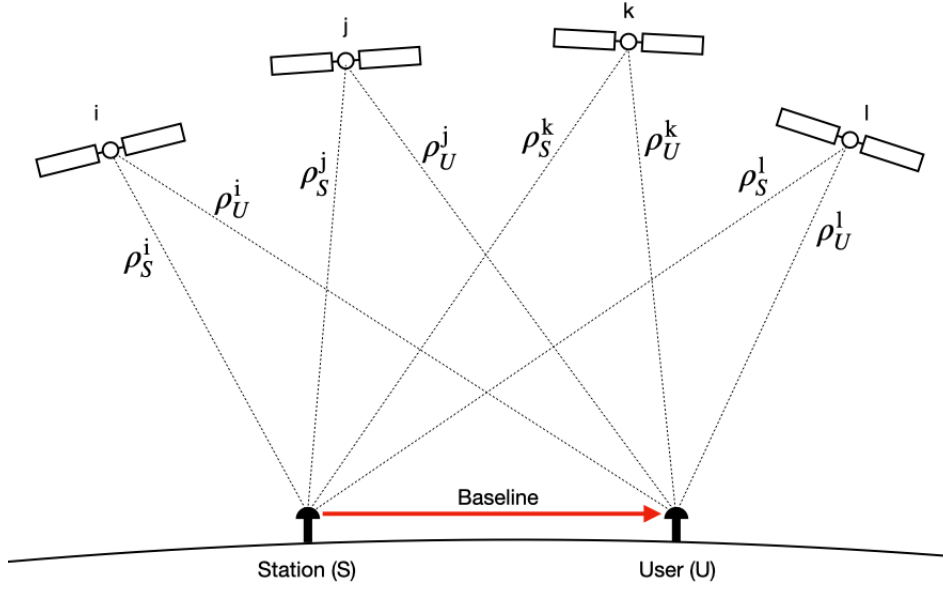
FIGURE 2.11: The baseline between a user and a reference station is determined with relative positioning. The pseudoranges ρ connecting a GNSS satellite and a ground point are presented.

and the carrier phase relation free of ionosphere influence is (Hofmann-Wellenhof, Lichtenegger, and Collins, 2012):

$$\left[\Phi_1 - \frac{f_2}{f_1}\Phi_2\right]\frac{f_1^2}{f_1^2 - f_2^2} = \frac{f_1}{c}\rho + f_1\Delta\delta + \left[N_1 - \frac{f_2}{f_1}N_2\right]\frac{f_1^2}{f_1^2 - f_2^2}, \tag{2.53}$$

where f_1, f_2 are the two carrier frequencies, R_1, R_2 are the corresponding pseudoranges, N_1, N_2 denote the integer cycles and Φ_1, Φ_2 the carrier phases. The unknown parameters need to be determined are the position encoded in ρ, the receiver clock error $\Delta\delta$ and the atmospheric delay Δ^{Trop}. The above unknown parameters can be estimated using various approaches an techniques some of which exploit various constellations (Psychas, Verhagen, and Teunissen, 2020; Paziewski, Sieradzki, and Baryla, 2018; Li et al., 2020).

2.4.2 Relative Positioning

The unique characteristic of relative positioning is that it exploits the known position of a reference GNSS station to determine the coordinates of another GNSS receiver. Thus, the objective of relative positioning is to calculate the three-dimensional vector, usually referred to as baseline, connecting two GNSS antennas (Figure 2.11). The equation of station (S) and user (U) position vectors is:

$$\mathbf{X_U} = \mathbf{X_S} + \mathbf{b_{S,U}}, \tag{2.54}$$

where $\mathbf{X_U}$ and $\mathbf{X_S}$ are the position vectors of the user and station respectively and $\mathbf{b_{S,U}}$ their baseline. The Equation (2.54) can be expressed using the coordinates (X,

Y, Z) of the two points with the corresponding subscripts as:

$$\mathbf{b_{S,U}} = \begin{bmatrix} X_U - X_S \\ Y_U - Y_S \\ Z_U - Z_S \end{bmatrix} = \begin{bmatrix} \Delta X_{S,U} \\ \Delta Y_{S,U} \\ \Delta Z_{S,U} \end{bmatrix}. \tag{2.55}$$

The relative positioning can be based upon code or phase ranges. However, the combination of them is preferred as it offers improved accuracy. This type of positioning requires simultaneous observations with matching time tagging. Single, double, and triple differences can be performed using as nodal points the station, the user, and observable satellites. These differences are between ground points, among satellites and/or in the time domain (Santerre and Geiger, 2018; El-Rabbany and Kleusberg, 2003; Georgiadou and Kleusberg, 1988). The most widely used methodology is the triple-differences across receivers, satellites, and time. The carrier phase frequencies Φ of triple-differences between satellites (j, k), points (S, U), and times (1, 2) can be expressed as:

$$\begin{aligned} \Phi_{US}^{jk}(t_{12}) = &+ \Phi_U^k(t_2) - \Phi_U^j(t_2) - \Phi_S^k(t_2) + \Phi_S^j(t_2) \\ &- \Phi_U^k(t_1) + \Phi_U^j(t_1) + \Phi_S^k(t_1) - \Phi_S^j(t_1), \end{aligned} \tag{2.56}$$

and the corresponding equation of pseudoranges ρ:

$$\begin{aligned} \rho_{US}^{jk}(t_{12}) = &+ \rho_U^k(t_2) - \rho_U^j(t_2) - \rho_S^k(t_2) + \rho_S^j(t_2) \\ &- \rho_U^k(t_1) + \rho_U^j(t_1) + \rho_S^k(t_1) - \Phi_S^j(t_1). \end{aligned} \tag{2.57}$$

The use of triple-difference has the advantage of eliminating the common ambiguities by differentiating across equations. Practically, multiple stations are utilized for the estimation of an unknown position as detailed in Kouba (2009).

2.5 Targets for Altimetry Calibration

Satellite altimeters are in essence nadir looking radars emitting electromagnetic radiation (usually in Ku, C and Ka bands, Table 2.5) which travel through the atmosphere, gets reflected upon a target and finally returns to the radar system. The two-way round-trip time of the electromagnetic waves is recorded by the on-board altimeter and used to determine the distance between the satellite and the reflecting target, since the signal's speed is known. In satellite altimetry, the target can be the ocean, sea ice, glaciers and in-land waters. On the other hand, in the case of direct absolute calibration (range and sigma naught) a point target with known properties is exploited. Targets with such characteristics are the active microwave transponder and passive corner reflector.

   At this point of the dissertation, the basic theory of electrodynamics that is related with the interaction of satellite altimeters signals with ground passive targets will be provided. The theoretical background consists of: (1) the Maxwell's equations which are the "building blocks" of every electromagnetic interactions, (2) the fundamental principles of radars and their range equation which relates the emitted and received power, the distance between the target and the radar, the characteristics of the target and other losses, (3) the decibel scale which is widely used in radar processing analyses, and lastly (4) the radar cross section which determines if a target can be used in satellite altimeters calibration. The maximum radar cross

section denotes if a target is separable from the clutter i.e., the amplitude of the signal is significantly stronger compared to the area's clutter. On the other hand, the dependence of the radar cross section on spherical angles affects the detection probability. The formal definition and a more intuitive explanation of radar cross section is provided in this work.

After the description of the aforementioned background theory, this work focuses on a specific category of point targets, i.e., corner reflectors. Their incorporation in satellite altimeters calibration is proposed and the resulting benefit is proved. The basic types of trihedral corner reflectors along with their fundamental characteristics are described in the sequel. To facilitate the comprehension of the complicated interaction of corner reflectors with incident microwaves, the interpretation is divided into several steps. Initially, the reflection of waves onto the simplest reflector, a flat metallic plate, is described. Then, the reflection upon a dihedral corner reflector is explained and the value of the reflected wave phase is calculated in order to prove that corner reflectors can be used in satellite altimetry range calibration . Only their integration in range calibration is analyzed, since their use in sigma-naught calibration is commonly known and used (Sarabandi and Chiu, 1996; Sorensen, 1991; Badatala et al., 2022). The zero-phase difference between waves reflected onto the apex of a corner reflector and these onto the corner reflector's plates, analytically proves that their phase center coincide with their apex (Döring, Schwerdt, and Bauer, 2007). Thus, they do not introduce additional delay to the signal and can be used as an independent way to estimate in situ the transponder's internal delay. All the measured ranges during a corner reflector calibration, that were calculated by the re-tracking of the waveform, are referenced to the corner reflector's apex. Correspondingly, the geometric distance between the corner reflector and the satellite altimeter is calculated using the coordinates of the apex and the satellites CoG respectively. Thus, the bias, which is the difference of the measured with the geometrical range, is not affected by the uncertainty of the internal delay knowledge as in the case of active transponders.

2.5.1 Maxwell's equations

The calibration of satellite altimeters with point targets is based on the propagation of electromagnetic signals through the atmosphere and its reflection upon the point target. Therefore, the incident electric or magnetic field at the position of the target should be known before the determination of its radar cross section can be performed. All electromagnetic phenomena are described by the four Maxwell's equations. Thus, Maxwell equation are shortly described.

(A)   (B)
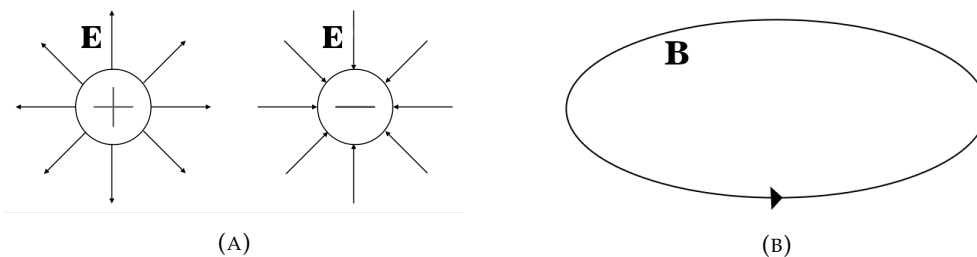
FIGURE 2.12: Graphical representation of the Gauss (A) law and the law of the magnetic field source (B).
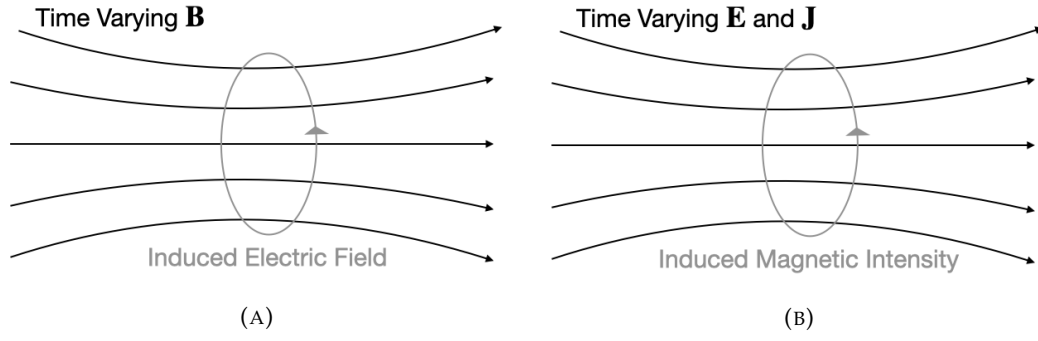
FIGURE 2.13: Graphical representation of the Faraday (A) and Ampere (B) laws.

The first, is the Gauss's law (Figure 2.12a), which connects the electric field $\mathbf{E}$ with its source, the electric charge density ρ.

$$\nabla \cdot \mathbf{E} = \frac{1}{\epsilon_0} \rho, \tag{2.58}$$

where ϵ_0 is the vacuum permittivity. The Gauss law describes that always the source of the electric field is a charge. Additionally, the electric field lines point away or towards the charge, depending on the sign of the charge, positive or negative respectively.

The second equation (that has not a specific name) states that a magnetic monopole (Figure 2.12b) does not exist and thus the lines of the magnetic field $\mathbf{B}$ always close back on themselves.

$$\nabla \cdot \mathbf{B} = 0. \tag{2.59}$$

The third equation, named the Fadaday's law (Figure 2.13a), specifies the relation between the solenoid part of the electric field $\mathbf{E}$ with the change of the magnetic field $\mathbf{B}$, over time.

$$\nabla \times \mathbf{E} = \frac{\partial \mathbf{B}}{\partial t}. \tag{2.60}$$

The fourth and last equation is the Ampère's law (Figure 2.13b). The Ampère's law refers to the solenoid part of the magnetic field $\mathbf{B}$ which is related to the electric field current density $\mathbf{J}$.

$$\nabla \times \mathbf{B} = \mu_0 \mathbf{J}, \tag{2.61}$$

where μ_0 is the permeability of space. It should be noted that the Equation (2.61) was further expanded by Maxwell. From this analysis, another term was added to the right part of Ampère's law, stating that a time varying electric field $\mathbf{E}$ can induce magnetic field $\mathbf{B}$. The revised equation is:

$$\nabla \times \mathbf{B} = \mu_0 \mathbf{J} + \mu_0 \epsilon_0 \frac{\partial \mathbf{E}}{\partial t}. \tag{2.62}$$

2.5.2 Radar Range Equation

An altimeter is basically a nadir looking radar measuring ranges. Thus, the definition of the radar range equation is provided. This radar range equation describes the relation between the emitted power, its scattering upon a target and finally the received power. In other words, if the transmitted power P_t (measured in watts) of a

radar is emitted by an isotropic antenna, the power density $D(R)$ at distance R can be written as (Knott, Schaeffer, and Tulley, 2004):

$$D(R) = \frac{P_t}{4\pi R^2}. \tag{2.63}$$

If the isotropic antenna is replaced with a directional one with gain $G_t(\theta, \phi)$, the power density becomes:

$$D(R) = \frac{P_t G_t}{4\pi R^2}. \tag{2.64}$$

Introducing the radar cross section σ, which is defined as the target area required to radiate isotropically the same amount of power with this transmitted towards the radar's receiving antenna, the $D(R)$ can be written as:

$$D(R) = \frac{P_t G_t \sigma}{(4\pi R^2)^2}, \tag{2.65}$$

with the assumption at bistatic radar systems that the distance between the target and the receiving antenna is equal to this of the target with the transmitting antenna. Thus, the denominator expresses the area of the two spheres, one of the emissions and the second of the reflection. Again, if the receiving antenna is not isotropic, but rather has a preferable direction expressed by the gain $G_r(\theta, \phi)$, which is assumed to be $G_r = G_t = G$, the received power P_r is:

$$P_r = \frac{P_t G^2 \lambda^2 \sigma}{(4\pi)^3 R^4}. \tag{2.66}$$

The Equation (2.66) is a simplified form of the radar range equation in which various losses and phenomena are ignored. With more detail the received power P_r at a radar from a point target (PT) is (Ruck, Barrick, and Stuart, 2002):

$$P_r = \frac{P_t G_t}{L_t} \frac{1}{4\pi r_t^2 L_{mt}} \sigma \frac{1}{4\pi r^2 L_{mr}} \frac{G_r \lambda_0^2}{4\pi L_r} \frac{1}{L_p}, \tag{2.67}$$

where P_t is the radar's transmitted power, G_t is the gain of the transmitting antenna at the direction of PT and L_t, L_r are the numerical factor used to include losses at the transmitting and receiving system respectively. Also, r_t is the range between the radar's transmitting antenna and PT, σ is the radar cross section of PT, L_{mt} and L_{mr} account for propagating losses across the medium between the radar and PT, r is the range between PT and receiving antenna, G_r is the gain of the receiving antenna at the direction of PT, λ_0 is the wavelength of the electromagnetic radiation and L_p is the power losses that originate from polarization. Rewriting Equation (2.67) to get an expression for radar cross section σ:

$$\sigma = \frac{4\pi P_r L_r}{G_r \lambda_0^2} \frac{L_t}{P_t G_t} (4\pi)^2 r_t^2 r^2 L_{mr}.L_{mt} L_p \tag{2.68}$$

Decibel Scale

The definition of the decibel scale is presented because it is used throughout the dissertation. This decibel scale is used because the radar cross section of different targets fluctuates from thousands of square meters (e.g., ships) to decimal square

TABLE 2.5: Frequency bands of radars and their usual applications
(Knott, Schaeffer, and Tulley, 2004).

Band Notation	Frequency Range	Application
VHF	50 – 300 MHz	Very Long Range Surveillance
UHF	300 – 1000 MHz	Very Long Range Surveillance
L	1 – 2 GHz	Very Long Range Surveillance, Enroute Traffic Control
S	2 – 4 GHz	Moderate Range Surveillance, Terminal Traffic Control, Long Range Weather
C	4 – 8 GHz	Long Range Tracking, Airborne Weather Detection
X	8 – 12 GHz	Short Range Tracking, Missile Guidance, Mapping, Marine Radar, Airborne Intercept
K_u	12 – 18 GHz	**Satellite Altimetry**, High Resolution Mapping
K	18 – 27 GHz	Water Vapour Absorption Estimation
K_a	27 – 40 GHz	**Satellite Altimetry**, High Resolution Mapping, Airport Surveillance
Millimeter	40 – 100 GHz	Experimental

meters (e.g., fighter aircrafts). Moreover, the values of power in Equation (2.67) usually cover multiple orders of magnitude i.e., the transmitted power P_t is at the order of megawatts whereas the received power P_r after the absorption and other losses is at the order of picowatts (Knott, Schaeffer, and Tulley, 2004). Therefore, the need of introducing a logarithmic scale for radar range equation arose. In particular, this logarithmic scale is called decibel (dB):

$$P(\text{dB}) = 10 \log_{10}\left(\frac{P}{P_0}\right), \tag{2.69}$$

where P is the power measured in W and P_0 is the reference power level, which can be equal to 1 W or 1 mW. The $P(\text{dB})$ is measured in units dBW or dBm respectively. It should be noted that even though power in radar systems is expressed usually in dBW or dBm the SI unit of power is the W which in base units is equal to:

$$1W = 1\,kg\,m^2\,s^{-3}. \tag{2.70}$$

$$P_i \qquad\qquad \sigma P_i \qquad\qquad P_s = \frac{\sigma P_i}{4\pi R^2}$$

| Incident Power | Total Power Intercepted | Isotropically Transmitted |
| Density | by the Target | Power by the Target |
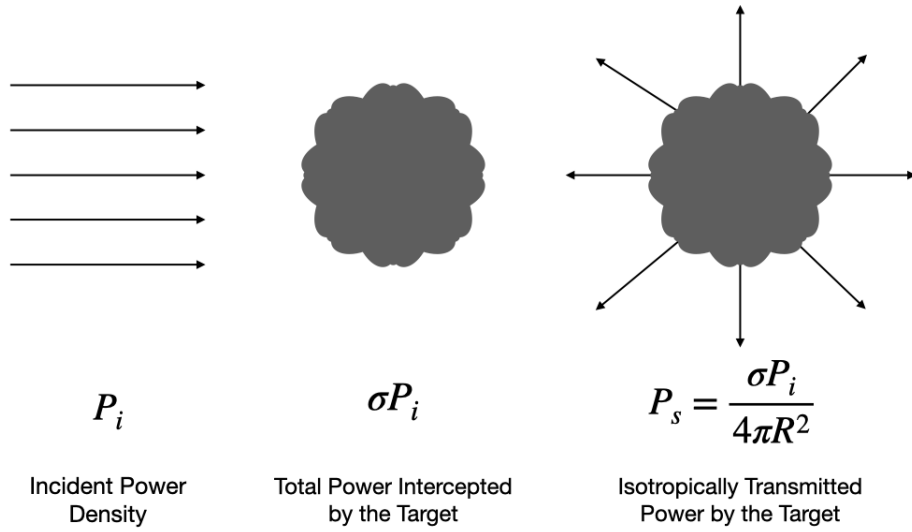
FIGURE 2.14: Graphical representation of radar cross section.

For the radar cross section, the reference level is usually set to 1 m^2 and the corresponding decibel scale unit is dBm^2.

$$\sigma_{\text{dBsm}} = \sigma_{\text{dBm}^2} = 10 \log_{10}\left(\frac{\sigma}{\sigma_0}\right), \tag{2.71}$$

where σ is measured in m^2. Practically, the radar cross section magnitude is normalized by the wavelength of the incident radiation and the unit is turned into dBλ^2. This transformation is convenient for comparing different targets independently of the scattered wavelength.

2.5.3 Radar Cross Section

The radar cross section expresses the apparent surface of a target from a radar and is used to understand if a point target can be used for calibration. The Institute of Electrical and Electronics Engineers (IEEE) dictionary defines the radar cross section σ (Jay and Goetz, 1984):

$$\sigma = \lim_{r\to\infty} 4\pi r^2 \frac{|E^{\text{scat}}|^2}{|E^{\text{inc}}|^2}, \tag{2.72}$$

where E^{scat} is the electric field scattered by the target and E^{inc} is the incident electric field at a radar cross section σ. Equation (2.72) expresses the ability of a target to reflect power and can be quantified as 4π times the fraction of the scattered power per unit solid angle and the incident power per unit area of a plane wave (Knott, Schaeffer, and Tulley, 2004).

Another way of describing the radar cross section is to use the power density P_i incident at the position of a target in the far-field. The radar cross section σ (in m^2) of the target equals to the area that reflects power (in W) equal to σP_i (Figure 2.14). Assuming that this power is scattered isotropically in all directions (ignoring absorption) the power density that is scattered from the target with σ is:

$$P_s = \frac{\sigma P_i}{4\pi R^2}. \tag{2.73}$$

Solving Equation (2.73) for σ we get:

$$\sigma = 4\pi R^2 \frac{P_s}{P_i}. \tag{2.74}$$

Thus, the radar cross section can be intuitively comprehended as the fraction of the scattered with the incident power density, which is then multiplied by $4\pi R^2$. The parameter $4\pi R^2$ is justified because the scattered power is assumed to be transmitted isotropically. Considering that the power density of electromagnetic waves is a function of the square of the magnetic **H** or electric **E** field, Equation (2.74) can be expressed as:

$$\sigma = 4\pi R^2 \frac{|\mathbf{E}^{\text{scat}}|^2}{|\mathbf{E}^{\text{inc}}|^2} = 4\pi R^2 \frac{|\mathbf{H}^{\text{scat}}|^2}{|\mathbf{H}^{\text{inc}}|^2}. \tag{2.75}$$

This more intuitive derivation of Equation (2.75) coincides with the formal definition of IEEE summarized in Equation (2.72).

The radar cross section quantifies the detectability of a target that is exploited for satellite altimeter calibration in this dissertation. However, depending on the needs of the application there are other definitions of cross sections such as these described in Knott, Schaeffer, and Tulley (2004):

- The absorption cross section which is the ratio between the absorbed power and the incident power density.

- The total cross section which is the ratio between the scattered power in all directions and incident power density.

- The extinction cross section which is the sum of the absorption and total cross sections and expresses the power that was abstracted by the incident electromagnetic field by the target.

2.5.4   Corner Reflectors

Corner reflectors are proposed as alternative point targets for altimetry calibration along with active transponders. Thus, their radar cross section is described at this point. The radar cross section of corner reflectors can be approximated using geometrical physics in the high-frequency regime using the equation:

$$\sigma \approx 4\pi \frac{A_e^2}{\lambda_0^2}, \tag{2.76}$$

where A_e is the effective area of the corner reflector that reflects radiation towards the monostatic radar (the satellite altimeter in the framework of this dissertation) and λ_0 is the wavelength of the incident radiation (Ruck, Barrick, and Stuart, 2002). To estimate the radar cross section of corner reflectors of different type, their corresponding effective area is substituted. For a dihedral corner reflector, which is comprised of two metallic flat plates connected with an angle of 90° presented in Figure 2.15, the effective area equals to (Wang and Jeng, 1998):

$$A_e = 2\alpha\beta \sin\left(\frac{\pi}{4} + \phi\right). \tag{2.77}$$

Substitution of Equation (2.76) into (2.77), results into an expression of the radar
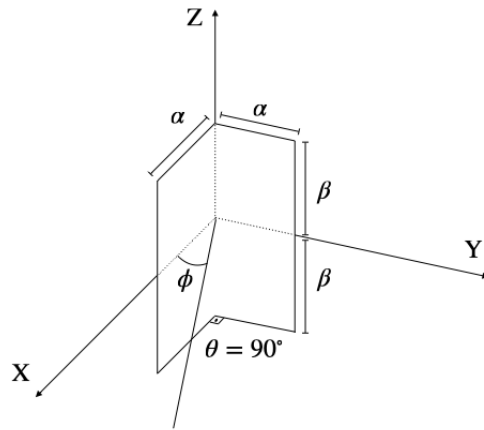
FIGURE 2.15: A dihedral corner reflector is presented along with the
angle ϕ of the incoming radiation.

cross section that depends upon the dimensions of the dihedral corner reflector α
and β, the wavelength of the reflected radiation λ and the wave's incident angle ϕ.

$$\sigma \approx \frac{16\pi\alpha\beta\, sin^2(\pi/4 + \phi)}{\lambda^2}. \tag{2.78}$$

The dihedral corner reflector has significant cross section (compared with its physi-
cal dimensions) over a wide range of $30°$ inside the $3\, dB$ range from the maximum.
However, the disadvantage of dihedral corner reflectors that reduces their opera-
tional value , is that they reflect radiation only towards the plane perpendicular to
the connection line of the two plates (Figure 2.16). This is evident from Equation
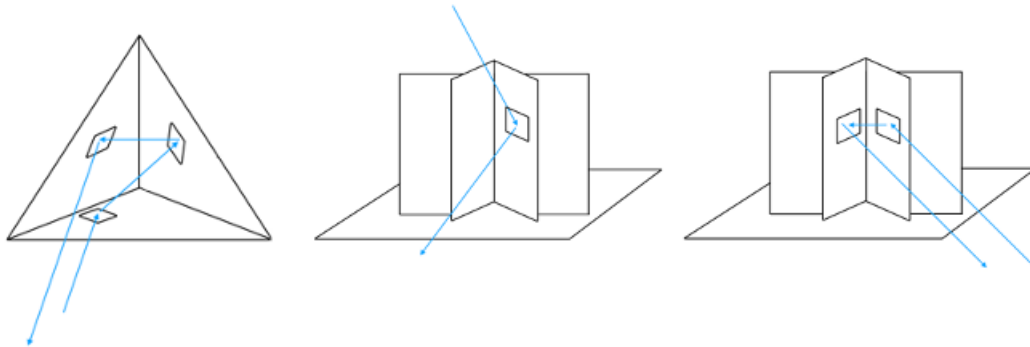
FIGURE 2.16: In the left figure, the signal returns to its source after the
"triple bounce" on the trihedral corner reflector. For dihedral corner
reflectors, radiation returns only if the radiation plane is perpendicu-
lar to the connecting line of the two plates and not in any other con-
figuration, as presented in the right and center figures respectively.

(2.78), that depends only upon the angle ϕ lying on the XY plane.

The solution to this limitation is the addition of another plate and the transition
from the aforementioned dihedral to trihedral corner reflector. The third plate offers
the characteristic "triple bounce" (left of Figure 2.16), which allows the incident ra-
diation to return towards the direction of its emitting source independently of the

(A)

(B)   (C)
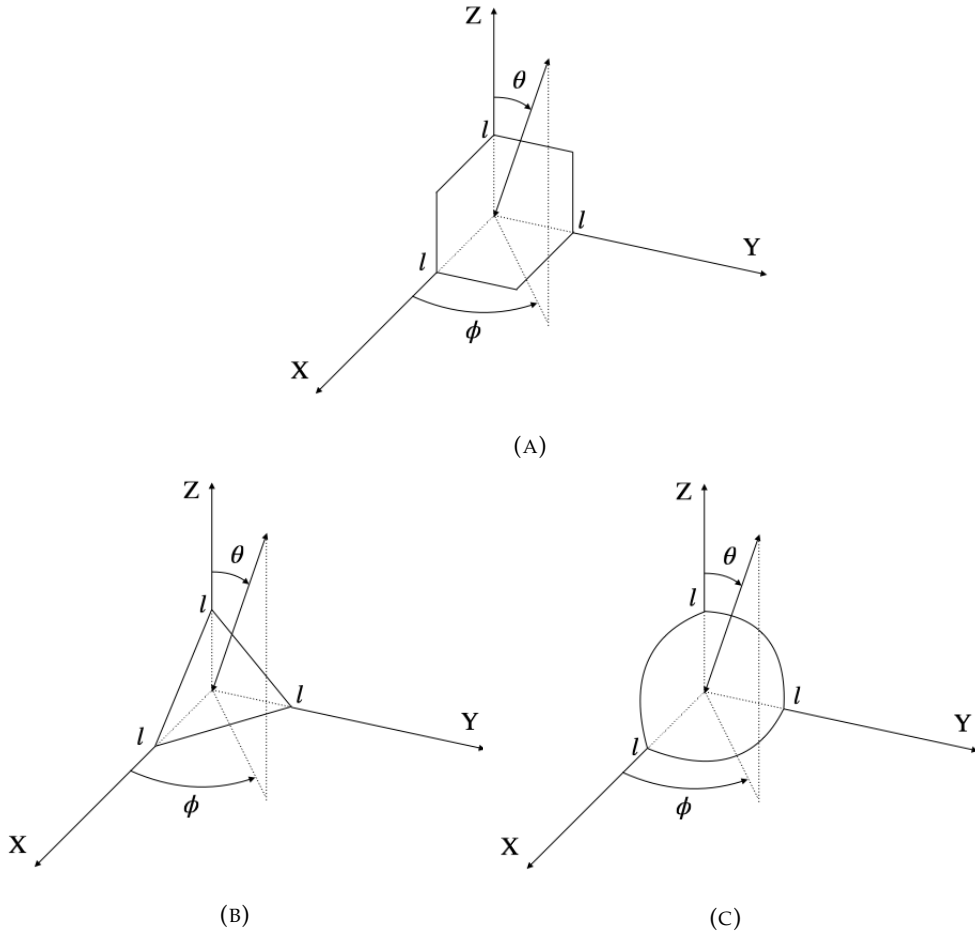
FIGURE 2.17: The different types of trihedral corner reflectors (A) rectangular, (B) triangular and (C) circular are presented.

incident's wave direction (assuming that it enters the reflector's opening). A trihedral corner reflectors can be divided into three main categories based on the shape of each plate. Namely, the main types of corner reflectors are the rectangular, triangular, and circular trihedral corner reflectors (Figure 2.17). Their main characteristics as passive point targets are presented in Table 2.6. These features are related with their maximum and average cross section and the coverage around their symmetry axis.

The radar cross section of a rectangular corner reflector depends upon the length l of the square plates, the azimuth angle ϕ and the elevation angle θ of the incident radiation. The approximation of σ for incident radiation near its symmetry axis (at $\phi = 45°$ and $\theta = 54.74°$) can be expressed as (Ruck, Barrick, and Stuart, 2002):

$$\sigma(\theta, \phi) \approx \frac{4\pi}{\lambda_0} l^4 \cos^2\theta (4 - \cot\phi)^2. \tag{2.79}$$

The same approximation for triangular corner reflectors is (Ruck, Barrick, and Stuart, 2002):

$$\sigma(\theta, \phi) \approx \frac{4\pi}{\lambda_0} l^4 \left[\cos\theta + \sin\theta(\sin\phi + \cos\phi) - 2\Big(\cos\theta + \sin\theta(\sin\phi + \cos\phi)\Big)^{-1} \right]^2. \tag{2.80}$$

Trihedral corner reflectors will be exploited as passive point targets for satellite altimeters sigma-naught and range calibration. As far as the first kind of calibration, the use of corner reflectors is a well-established methodology in various satellite radars. Some examples are presented in the works of Jauvin et al. (2019), Garthwaite (2017), Sun et al. (2017), Garthwaite et al. (2015), Willatt et al. (2011), and Cullen et al. (2007).

Thus, we will elaborate only on their utilization as passive point targets for range calibration. Their key feature that is used, which originates from their geometry, is that their phase center is located exactly at their apex. This approximation is valid for corner reflectors with dimensions at the order of ∼1 m at the wavelengths of satellite altimetry (Ku and Ka bandwidths). In other words, the distance from the source to the target and back is always the same independently of the path (numerous combinations of double or triple reflection upon the plates) that the incident radiation follows and equal to reflection upon the apex. Hence, the corresponding geometrical distance that will be used to compare the measured range and determine the range bias, is calculated using the coordinates of the corner reflector's apex.

Reflection of Microwaves

In this dissertation the use of corner reflectors in the same network with transponders in PFAC is proposed. The first step to comprehend the interaction of corner reflectors with microwaves is to present the interaction of a plane wave with a rectangular metallic flat plate (representing one of the corner reflector sides). Specifically, the scattering of a TE^x (Figure 2.18) uniform plane wave is analyzed. The electric and magnetic field of the incident wave is:

$$\mathbf{E}^i = \eta H_0(\hat{a}_y \cos\theta_i + \hat{a}_z \sin\theta_i)e^{-j\beta(y\sin\theta_i - z\sin\theta_i)}, \tag{2.81}$$

$$\mathbf{H}^i = \hat{a}_x H_0 e^{-j\beta(y\sin\theta_i - z\sin\theta_i)}, \tag{2.82}$$

where H_0 is the magnitude of the incoming magnetic field, β is the propagation constant, a_x, a_y and a_z are the unit vectors of the coordinate system and θ_i (Figures 2.18, 2.19) the incident angle (Balanis, 2012). The solution of the scattered field using physical optics (Andrade et al., 2003) is exact in the case of a plate with infinite width and length. On the other hand, the solution is an approximation in the case of a plate with finite dimensions. For the latter case, the solution has higher accuracy closer to the specular direction in which the Snell's law is valid, whereas the solution reliability degrades at other angles. The wavelengths satellite altimeters operating at Ku and Ka bandwidths are of the order of cm. Thus, a rectangular plate of approximately 2 m can be approximated as infinitive (100 times greater), relatively to the Ku and Ka wavelength and neglect edge effects. The solution regarding the scattered

TABLE 2.6: Characteristics of different types of corner reflectors (Ruck, Barrick, and Stuart, 2002).

Type of Trihedral Corner Reflector	Maximum Radar Cross Section	Average Radar Cross Section	Coverage Around Symmetry Axis
Rectangular	$12\pi l^4/\lambda_0^2$	$0.7\pi l^4/\lambda_0^2$	23°
Triangular	$4\pi l^4/\lambda_0^2$	$0.17\pi l^4/\lambda_0^2$	40°
Circular	$15.6\pi l^4/\lambda_0^2$	$0.47\pi l^4/\lambda_0^2$	32°
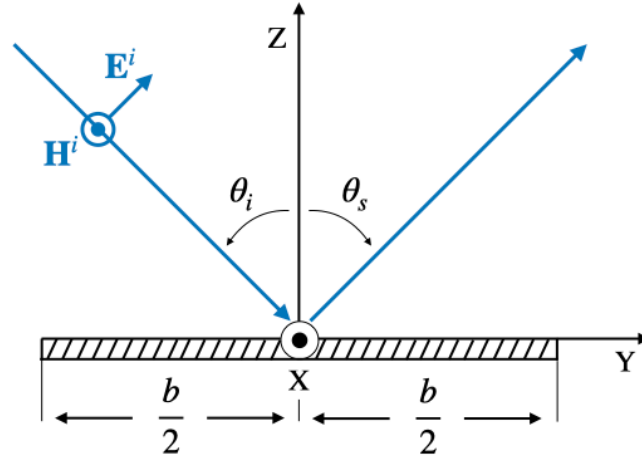
FIGURE 2.18: A YZ cross section of a TE^x incident wave reflected by a flat plate.

field E^s and H^s which is detailed in Balanis (2012):

$$E_r^s \simeq 0, \tag{2.83}$$

$$E_r^s \simeq C\frac{e^{-j\beta r}}{r}\left[cos\theta_s\, sin\phi_s\left(\frac{sin(X)}{X}\right)\left(\frac{sin(Y)}{Y}\right)\right], \tag{2.84}$$

$$E_\phi^s \simeq C\frac{e^{-j\beta r}}{r}\left[cos\phi_s\, sin\phi_s\left(\frac{sin(X)}{X}\right)\left(\frac{sin(Y)}{Y}\right)\right], \tag{2.85}$$

$$H_r^s \simeq 0, \tag{2.86}$$

$$H_\theta^s \simeq -\frac{E_\phi^s}{\eta}, \tag{2.87}$$

$$H_\theta^s \simeq +\frac{E_\theta^s}{\eta}, \tag{2.88}$$

the parameters present in the above equations are:

$$C = -j\eta\frac{ab\beta H_0}{2\pi}, \quad X = \frac{\beta a}{2}sin\theta_s\, cos\phi_s, \quad Y = \frac{\beta b}{2}(sin\theta_s\, sin\phi_s - sin\theta_i), \tag{2.89}$$

where a, b are the dimensions of the plate (Figure 2.19) and θ, ϕ and r the spherical coordinates. Equations (2.83) up to (2.88) are simplified when computed for the principal electric plane in which $\phi_s = \pi/2$ and principal magnetic plane with $\theta_s = \theta_i$ and $\phi_s = 0$.

The radar cross section of a flat plate is:

$$\sigma = \lim_{r \to \infty}\left[4\pi r^2\frac{|\mathbf{E}^s|^2}{|\mathbf{E}^i|^2}\right] \Leftrightarrow \tag{2.90}$$
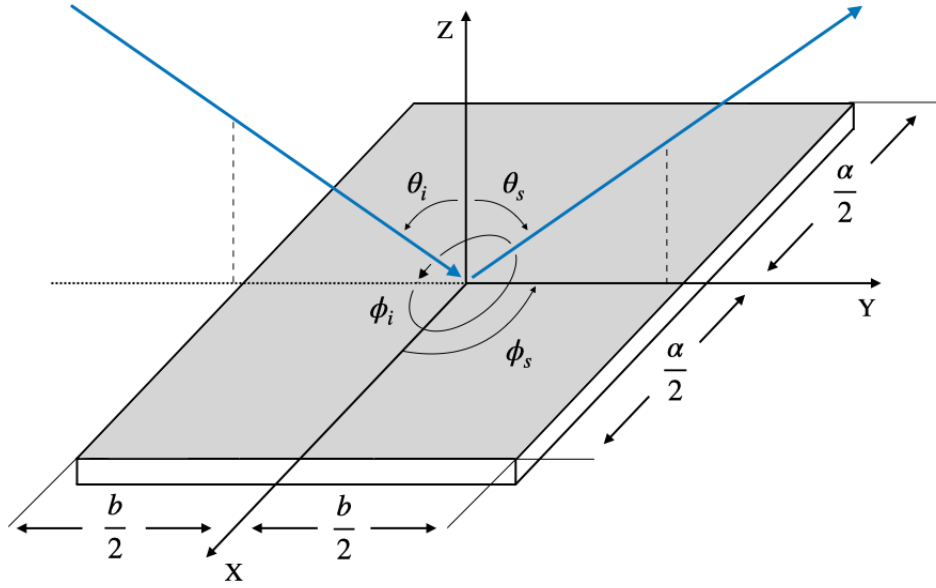
FIGURE 2.19: Scattering of a uniform plane wave by a flat plate.

$$\sigma = 4\pi \left(\frac{ab}{\lambda}\right)^2 (cos^2\theta_s\, sin^2\phi_s + cos^2\phi_s) \left[\frac{sin(X)}{X}\right]^2 \left[\frac{sin(Y)}{Y}\right]^2.$$

The backscattered σ (σ_B) in the direction that fields return to their source is for $\phi_s = \phi_i = \pi/2$, $\theta_s = \theta_i$ can be written using Equation (2.90) as:

$$\sigma_B = 4\pi \left(\frac{ab}{\lambda}\right)^2 cos^2\theta_i \left[\frac{sin(\beta b\, sin\theta_i)}{\beta b\, sin\theta_i}\right]^2. \tag{2.91}$$

Phase Center

The statement that the phase center of corner reflectors coincides with their apex will be proved analytically in this Section. The only assumption is that when the electromagnetic waves interact with the corner reflector they can be approximated as plane waves or in other words to consider points at the same distance along $\overline{Y}$ (Figure 2.20) as the same target. In our case, this assumption is completely justified as we are working in the far-field. This is justified because altimetry satellites fly at an altitude of about 800 - 1200 km (depending on the mission) while the wavelengths of altimetric signals are at the order of cm. For simplicity, the solution is performed for reflection by two perpendicular plates but can be extended for the case of triple "bounce".

Following the notation presented in Figure 2.20, the distance from the source R_0 to the target O and back to R_0 is compared with the path of the blue line that is reflected upon Plane A and B. The angle $O\hat{A}B$ is equal to the incident angle θ and thus $sin\theta\,|AB| = |OB|$. The double reflection on the corner reflector leads to phase φ that equals to:

$$\varphi = \frac{2\pi}{\lambda}\left(|R_0A'| + |AB| + |R_0B'|\right) = \frac{2\pi}{\lambda}\left((R_0 - |OA'|) + |AB| + |R_0 - OB'|\right), \tag{2.92}$$
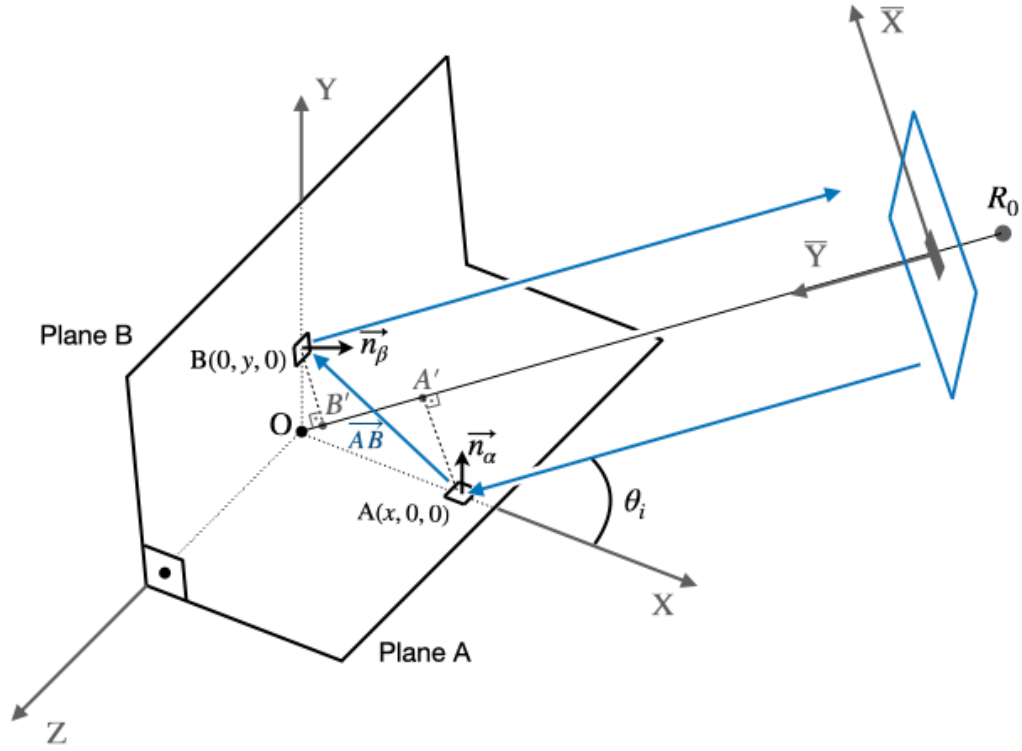
FIGURE 2.20: The reflection of a plane wave by a dihedral corner reflector is presented.

where λ is the wavelength of the incident wave and for example $|R_0A'|$ denotes the distance between the points R_0 and A'. Working on Equation (2.92) gives:

$$\varphi = \frac{2\pi}{\lambda}\left(2R_0 - |OA|\left(\frac{|OA'|}{|OA|} - \frac{|OB'|}{|OA|} + \frac{|AB|}{|OA|}\right)\right). \tag{2.93}$$

Using the trigonometric function of the incident angle θ:

$$cos\theta = \frac{|OA'|}{|OA|}, \tag{2.94}$$

$$\frac{|OA|}{|OB|} = \frac{cos\theta}{sin\theta} \iff \frac{|OA|}{cos\theta} = \frac{|OB'|}{sin^2\theta} \iff \frac{|OB'|}{|OA|} = \frac{sin^2\theta}{cos\theta}, \tag{2.95}$$

$$cos\theta = \frac{|OA|}{|AB|} \iff \frac{|AB|}{|OA|} = \frac{1}{cos\theta}. \tag{2.96}$$

Substituting equations (2.94), (2.95) and (2.96) into (2.93) leads to an expression of wave phase φ that equals to:

$$\varphi = \frac{2\pi}{\lambda}\left(2R_0 - |OA|\left(\frac{cos^2\theta}{cos\theta} - \frac{sin^2\theta}{cos\theta} + \frac{1}{cos\theta}\right)\right) \iff \varphi = \frac{2\pi}{\lambda}2R_0. \tag{2.97}$$

It is evident from the Equation (2.97), that the phase of the wave with double reflection is equal to this which begins from the radar source R_0 reflects upon the apex of the corner reflector and returns back to R_0.

2.6 Satellite Orientation in Space

2.6.1 Determination of the Satellite Attitude

This dissertation proposes the integration of satellite attitude into calibration processing. In this Section, the Jason-3 satellite will be used as an example to demonstrate the applied methodology of attitude determination and its impact on transponder calibration. The Jason-3 spacecraft is designed based on a "box-wing" structural model and consists of the spacecraft bus (box) and the solar panel arrays (wings). The main scientific payload of Jason-3 comprises the Poseidon-3B dual frequency (13.575 GHz and 5.3 GHz) nadir-looking radar altimeter, a microwave radiometer, a precise orbit determination system (PODS) and an attitude determination and control system (ADCS) (L. Cerri, 2022).

The PODS is responsible for the determination of the satellite's position in space and consists of a DORIS receiver, a Global Positioning Sytem (GPS) receiver and a laser retroreflector array. The ADCS provides the satellite's three-dimensional orientation via the combined analysis of measurements coming from star trackers, magnetometers, sun sensors, magnetic torqueres and gyroscopes. The star trackers have optical sensors that capture snapshots of the sky to calculate the positions of specific stars. A comparison of the observed position of stars with the corresponding one from the on-board ephemeris results in the accurate estimation of spacecraft attitude.

The instantaneous orientation of the satellite is used by an attitude actuation mechanism, consisting of reaction wheels, to perform attitude adjustments. The two attitude criteria for a reliable operation of the satellite are as follow. Firstly, the altimeter boresight should point downwards and perpendicularly to the Earth's reference ellipsoid (nadir-pointing). This criterion is necessary for the altimeter to receive reliable return waveforms, following their reflection on the ocean surface. Secondly, the solar panels direction should be perpendicular to the Sun arrays in order to provide and store adequate power to the satellite. The above requirements were firstly realized in the TOPEX/Poseidon altimeter using the algorithms described in (Perrygo, 1987). The same algorithm principles are also used for the adjustment of Jason-3 attitude.

The following reference systems need to be defined for the estimation of satellite attitude and the post-processing of altimetric products (Zeitlhöfler, 2019):

- The inertial reference system (IRS; [O: UVW]), with its origin at the geocenter O. It is a system that does not rotate with the Earth and its axes are parallel to the barycentric system whose origin is at the Sun. The U axis passes from the equatorial plane with direction towards the vernal equinox ♈. The W axis coincides with the Earth's mean rotation axis and the V axis is perpendicular to the U axis to form a right-hand orthogonal reference system. This system is also referred to as "pseudo-inertial" because of the acceleration arising from the Earth's revolution around the Sun.

- The Earth-fixed reference system (EFRS; [O: XYZ]), with its origin at the geocenter O. It is a reference system that rotates with the Earth's angular velocity. Its origin O also coincides with the center of the reference ellipsoid, i.e., the WGS84 ellipsoid for the latest processing baseline (F) of Jason-3 products. The X and Y axes are located at the equatorial plane with directions towards the prime meridian ($\lambda = 0°$) and perpendicular to it ($\lambda = 90°$), respectively. The Z

axis coincides with the Earth's rotation axis with direction towards the North Pole.

- The satellite body reference system (SAT; [Q: $x_B y_B z_B$]), with its origin at the center Q of the launcher attachment ring on the satellite. The x_B axis is parallel to the satellite primary direction and towards the radiometer antenna. The y_B axis is parallel to the rotation axis of the solar panels with direction towards the right solar panel array. The z_B axis direction is chosen to form an orthogonal right-handed reference system. Ideal attitude of the satellite body is realized when the z_B axis is perpendicular to the reference ellipsoid.

- The orbital reference system (ORB; [K: xyz]), with its origin at the satellite CoG (denoted by K in Fig. 2.21). The x axis is along the radial vector connecting the geocenter O and the satellite CoG, K, with direction towards zenith, which is characterized as reverse geocentric positioning (Vallado, 2001). The z axis is perpendicular to the satellite orbital plane with the same direction as the orbital angular momentum. Finally, the y axis has a direction to complete a right-hand orthogonal reference system (i.e., towards the satellite velocity vector but not always parallel to it).

- The local orbital reference system or roll-pitch-yaw system (RPY; [K: $x_0 y_0 z_0$]), has its origin at the satellite CoG, K. Its z_0 axis (yaw) is perpendicular to the reference ellipsoid with a direction towards nadir. The y_0 axis (pitch) is perpendicular to the orbital plane with direction opposite to angular momentum. Finally, the x_0 axis (roll) is defined to form an orthogonal reference system, with direction same as the satellite velocity vector.

The reference systems listed above are presented in Fig. 2.21. The satellite attitude corresponds to the three-dimensional orientation of the satellite spacecraft in space, and it is commonly described by the roll, pitch, and yaw angles, i.e., the angles needed to be applied in order to transform a vector from RPY to SAT system. In the sequel, the fundamental expressions used to estimate the satellite attitude angles are provided.

The transformation of a column-vector $\mathbf{X}_I = [U, V, W]^T$ to $\mathbf{X}_S = [x_B, y_B, z_B]^T$, i.e., from the inertial IRS to the satellite body reference system SAT is performed as:

$$\mathbf{X}_S = \begin{bmatrix} x_B \\ y_B \\ z_B \end{bmatrix} = \mathbf{R}_{IRS \to SAT} \begin{bmatrix} U \\ V \\ W \end{bmatrix} = \mathbf{R}_{IRS \to SAT} \mathbf{X}_I, \qquad (2.98)$$

where the matrix $\mathbf{R}_{S1 \to S2}$ denotes the rotation matrix (square matrix) that transforms a vector from reference system S1 to S2. The rotation matrix $\mathbf{R}_{IRS \to SAT}$ is calculated using information stored in quaternions by (Zeitlhöfler, 2019):

$$\mathbf{R}_{IRS \to SAT} = \begin{bmatrix} q_s^2 + q_x^2 - q_y^2 - q_z^2 & 2(q_x q_y + q_s q_z) & 2(q_x q_z + q_s q_y) \\ 2(q_x q_y + q_s q_z) & q_s^2 - q_x^2 + q_y^2 - q_z^2 & 2(q_y q_z + q_s q_x) \\ 2(q_x q_z + q_s q_y) & 2(q_y q_z + q_s q_x) & q_s^2 - q_x^2 - q_y^2 + q_z^2 \end{bmatrix}, \qquad (2.99)$$

where q_s, q_x, q_y and q_z are the four components of the quaternion. The rotation matrix $\mathbf{R}_{IRS \to SAT}$ can be expressed by the following sequence of rotations (Bloßfeld

FIGURE 2.21: Graphical representation of fundamental reference systems used for satellite attitude determination. The direction OA is defined by the vernal equinox, and the direction OB denotes the prime meridian ($\lambda = 0°$).

et al., 2020):

$$\mathbf{R}_{\text{IRS}\to\text{SAT}} = \mathbf{R}_{\text{RPY}\to\text{SAT}}\mathbf{R}_{\text{ORB}\to\text{RPY}}\mathbf{R}_{\text{IRS}\to\text{ORB}}. \tag{2.100}$$

Solving Eq. (2.100) with respect to $\mathbf{R}_{\text{RPY}\to\text{SAT}}$ yields

$$\mathbf{R}_{\text{RPY}\to\text{SAT}} = \mathbf{R}_{\text{IRS}\to\text{SAT}}\mathbf{R}_{\text{IRS}\to\text{ORB}}^{\text{T}}\mathbf{R}_{\text{ORB}\to\text{RPY}}^{\text{T}}, \tag{2.101}$$

where the relation $\mathbf{R}_{\text{S1}\to\text{S2}}^{\text{T}} = \mathbf{R}_{\text{S1}\to\text{S2}}^{-1} = \mathbf{R}_{\text{S2}\to\text{S1}}$ applies, as a rotation matrix is always orthogonal and thus its transpose will be equal to its inverse. The rotation matrix $\mathbf{R}_{\text{IRS}\to\text{ORB}}$ can be derived from the satellite state vector (i.e., position vector $\mathbf{r}$ and velocity vector $\mathbf{v}$) in the IRF system, as follows:

$$\mathbf{R}_{\text{IRS}\to\text{ORB}} = \begin{bmatrix} \mathbf{R}_1 & \mathbf{R}_2 & \mathbf{R}_3 \end{bmatrix}^{\text{T}}, \tag{2.102}$$

with the components $\mathbf{R}_1$, $\mathbf{R}_2$ and $\mathbf{R}_3$ defined as

$$\mathbf{R}_1 = \frac{\mathbf{r}}{|\mathbf{r}|}, \quad \mathbf{R}_3 = \frac{\mathbf{r}\times\mathbf{v}}{|\mathbf{r}\times\mathbf{v}|}, \quad \mathbf{R}_2 = \mathbf{R}_3\times\mathbf{R}_1, \tag{2.103}$$

and the rotation matrix $\mathbf{R}_{\text{ORB}\to\text{RPY}}$ given by

$$\mathbf{R}_{\text{ORB}\to\text{RPY}} = \begin{bmatrix} 0 & 1 & 0 \\ 0 & 0 & -1 \\ -1 & 0 & 0 \end{bmatrix}. \tag{2.104}$$

After the calculation of $\mathbf{R}_{\text{RPY}\to\text{SAT}}$ from Eqs. (2.100) through (2.104), the evaluation of roll, pitch and yaw angles, denoted as θ_r, θ_p and θ_y, respectively, is performed using the elements of $\mathbf{R}_{\text{RPY}\to\text{SAT}}$, as follows:

$$\theta_r = -\arctan\left(\frac{\mathbf{R}(3,2)}{\mathbf{R}(3,3)}\right), \; \theta_p = \arcsin\left(\mathbf{R}(3,1)\right), \; \theta_y = -\arctan\left(\frac{\mathbf{R}(2,1)}{\mathbf{R}(1,1)}\right), \quad (2.105)$$

with $\mathbf{R}(i,j)$ denoting the i-th row and j-th column element of the rotation matrix $\mathbf{R}$. All rotation angles are considered passive (i.e., the reference systems are actually rotated and not the contextual vectors) and positive in the counterclockwise direction.

2.6.2 Calibration Accounting For Satellite Attitude

For altimeter calibration with a transponder, it is common practice that the measured range $r(t)$ (after all the necessary corrections are applied) is used for the evaluation of range and datation biases based on Eqs. (2.3) and (2.6), respectively. As already discussed in Section 2.6.1, this range is referred from APC to CoG by the processing Agencies using the CoG correction δr.

   The description provided in the product handbook of each altimetry mission states that the CoG correction is defined as the distance along the z-axis between APC and CoG in the satellite body reference frame. Since this parameter is derived by the internal geometry of the spacecraft, its value is commonly kept constant for the entire duration of a mission. A review of previous studies showed that the corrected measured range used for calibration is indeed referred to CoG in this way. For example, the study of Hausleitner et al. (2012) mentions that the Jason-2 altimeter range is referred to the CoG by applying a CoG correction taken from the geophysical data record (GDR) products. The inspection of Jason-2 GDR products shows that this parameter is in fact considered constant. In the work of Cristea and Moore (2007), a constant CoG offset is also applied to correct the measured range for the satellite geometry prior to the calculation of Envisat range bias using a transponder.

   At this point, it is important to examine the implications of applying a constant CoG correction to the measured range with respect to satellite attitude (e.g., ideal or non-ideal) and the reflecting means on the Earth's surface (e.g., ocean surface or point targets). We firstly discuss the case of altimetric measurement acquisition over oceanic regions. Figure 2.22a shows the case of an ideal attitude for a satellite orbiting in geodetic mode, where the altimeter antenna points perpendicularly to the ellipsoid. The ocean surface (OCN1 point can therefore be considered a nadir-located target. The line segments |OCN1;APC|, |APC;CoG′| and |OCN1;CoG′| represent the measured range referred to APC, the constant CoG correction (along the z-axis in satellite body system) and the measured range referred to the CoG′, respectively. The CoG′ point represents the apparent CoG of the satellite at which the measured range $r(t)$ is referred to after applying the CoG correction δr using Eq. (2.4). Finally, the line segment |OCN2;CoG| denotes the distance between the true CoG and the sea surface. From the geometry of Fig. 2.22a it is evident that, for an ideal attitude, the distances |OCN1;CoG′| and |OCN2;CoG| are equal. It is therefore reasonable to consider that the measured range is correctly referred to the true CoG when the constant distance between APC-CoG along the z-axis is used.

   Figure 2.22b shows the case of non-ideal attitude, where only a pitch rotation (exaggerated) is displayed for simplicity. Assuming that all rotations are performed with respect to the CoG, the non-ideal attitude results in a change in the position of APC, and thus CoG′. As a consequence, |OCN1;CoG′| line segment is no longer
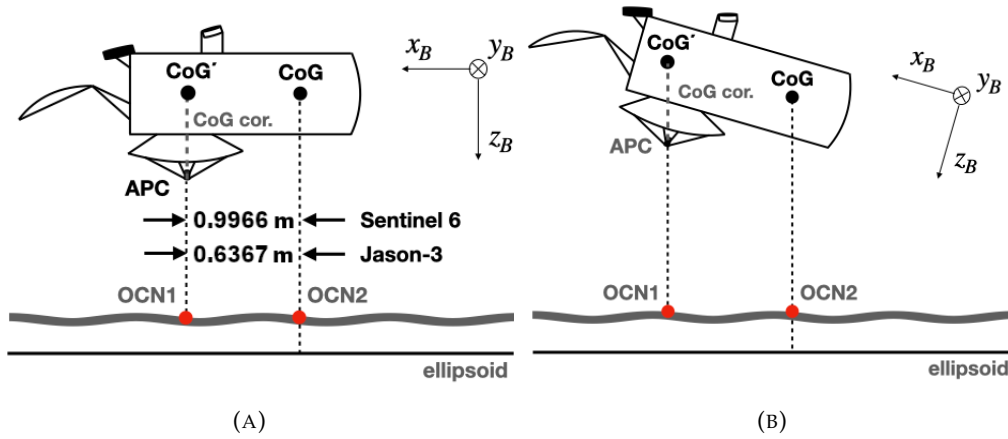
FIGURE 2.22: Altimetric measurement acquisition over sea surface for (a) ideal and (b) non-ideal satellite orientation. The axes of the SAT system (body system) are also presented.

equal to $|\text{OCN2;CoG}|$ distance and therefore the measured range is not realistically referred to the true CoG.

We continue by examining the impact of satellite attitude on altimetric measurements acquired over point targets (e.g., during an altimeter calibration with a transponder). A fundamental difference here is that, unlike ocean surface, transponders are practically never located directly at the nadir of the altimeter antenna. This is because the selection of a transponder site is limited by (a) the terrain topography and site accessibility based on existing road infrastructure, (b) the need to support the simultaneous calibration of multiple missions and (c) the quality of the signal clutter in the area. Even if a transponder is installed at the nadir of a satellite based on its nominal orbit, the repeat ground track location of a specific satellite pass can vary several hundreds of meters on the ground even for consecutive cycles.

The case of a satellite with ideal attitude passing over a transponder is given in Fig. 2.23a. The CoG correction, denoted by the equidistant line segments $|\text{APC;B}_0|$ and $|\text{APC;B}|$, is again applied to the measured range $|\text{APC;A}|$ and accounts for the coordinate difference between APC and CoG in the z_B direction. As a result, the measured range is referred to the apparent CoG, which corresponds to point B. The same also applies for non-ideal satellite attitude, as demonstrated in Fig. 2.23b. It is evident in both cases that the corrected measured range $|\text{A;B}|$ is not equal to the line segment $|\text{A;GoC}|$, therefore, the measured range $r(t)$ is not accurately referred to the satellite CoG.

From the discussion provided so far, it can be concluded that the conventional implementation of CoG correction is proper only when both of the following requirements are met: (a) ideal satellite attitude (i.e., zero attitude angles) and (b) targets located along the altimeter nadir. For satellites passing over transponders, none of these requirements are met. It is therefore reasonable to argue that during satellite calibration, the measured range $r(t)$ is not correctly referred to the CoG. On the contrary, the geometric distance $r_0(t)$ is rigorously referred to CoG since the estimated CoG coordinates provided in the GDR products already account for attitude effects. This inconsistency has a direct impact on the evaluation of range bias using Eq. (2.3). In addition, the different reference of the measured and geometric range can affect the TCA and introduce errors in the estimation of datation bias using Eq. (2.6). The datation errors due to non-ideal attitude mostly depend on the relative

position between B and CoG in relation to the transponder.

It is evident that attitude effects have an influence on transponder results and need to be further examined. An improved calibration procedure that accounts for these effects using attitude information is also required. A revisited calibration procedure is discussed in the rest of this Section. Attitude effects on transponder results can be corrected by rigorously referring the measured and geometric ranges to the same reference point using information regarding the instantaneous orientation of the spacecraft. In this dissertation, we have chosen the APC as the reference point for all parameters related to the calculation of range and datation biases. The new range bias, denoted as $\widetilde{B}(t)$, is defined as:

$$\widetilde{B}(t) = R(t) - R_0(t), \tag{2.106}$$

where $R(t)$ and $R_0(t)$ are the corrected measured and corrected geometric ranges between transponder and APC. The calculation of $R(t)$ is performed using Eq. (2.4) and only requires the subtraction of the constant CoG correction from the corrected altimeter range used in the conventional calibration procedure. The rest of the corrections (i.e., atmospheric delays, loading effects, etc.) are applied as usual. Following Eq. (2.5) the geometric range $R_0(t)$ is defined as:

$$R_0(t) = \sqrt{\left(X^{\mathrm{TRP}} - X^{\mathrm{APC}}(t)\right)^2 + \left(Y^{\mathrm{TRP}} - Y^{\mathrm{APC}}(t)\right)^2 + \left(Z^{\mathrm{TRP}} - Z^{\mathrm{APC}}(t)\right)^2} \tag{2.107}$$

It is evident from Eq. (2.107) that the evaluation of the geometric range $R_0(t)$ requires the calculation of APC coordinates in EFRS. The APC coordinate vector in EFRS, denoted as $\mathbf{V}_{\mathrm{EFRS}}^{\mathrm{APC}} = [X^{\mathrm{APC}}, Y^{\mathrm{APC}}, Z^{\mathrm{APC}}]^{\mathrm{T}}$, can be determined using the relation:

$$\mathbf{V}_{\mathrm{EFRS}}^{\mathrm{APC}} = \mathbf{V}_{\mathrm{EFRS}}^{\mathrm{CoG}} + \Delta\mathbf{V}_{\mathrm{EFRS}}, \tag{2.108}$$

where $\mathbf{V}_{\mathrm{EFRS}}^{\mathrm{CoG}}$ is the CoG coordinate vector and $\Delta\mathbf{V}_{\mathrm{EFRS}}$ the CoG–APC baseline vector in EFRS. The vector $\mathbf{V}_{\mathrm{EFRS}}^{\mathrm{CoG}}$ corresponds to the satellite position as defined by orbit determination. The baseline vector $\Delta\mathbf{V}_{\mathrm{EFRS}}$ depends on the satellite attitude and is transformed from SAT system [Q: $x_B y_B z_B$] to EFRS system [O: XYZ] using the equation:

$$\Delta\mathbf{V}_{\mathrm{EFRS}} = \mathbf{R}_{\mathrm{SAT}\rightarrow\mathrm{EFRS}}\Delta\mathbf{V}_{\mathrm{SAT}} = \mathbf{R}_{\mathrm{IRS}\rightarrow\mathrm{EFRS}}\mathbf{R}_{\mathrm{SAT}\rightarrow\mathrm{IRS}}\Delta\mathbf{V}_{\mathrm{SAT}}. \tag{2.109}$$

The calculation of rotation matrix $\mathbf{R}_{\mathrm{IRS}\rightarrow\mathrm{EFRS}}$ for the transformation between IRS and EFRS is described in the IERS conventions 2010 (Petit and Luzum, 2010b; "The IERS

TABLE 2.7: Coordinates of CoG and APC in the SAT system for Jason-3 and Sentinel-6 MF (L. Cerri, 2022; Giulicchi, 2022).

	Reference points	x_B (m)	y_B (m)	z_B (m)
Jason-3	Spacecraft center of gravity	1.0023	0.0000	−0.0021
	Altimeter phase center	1.6390	0.0000	0.6644
Sentinel-6 MF	Spacecraft center of gravity	1.5274	−0.0073	0.0373
	Altimeter phase center	2.5240	0.0001	0.5650
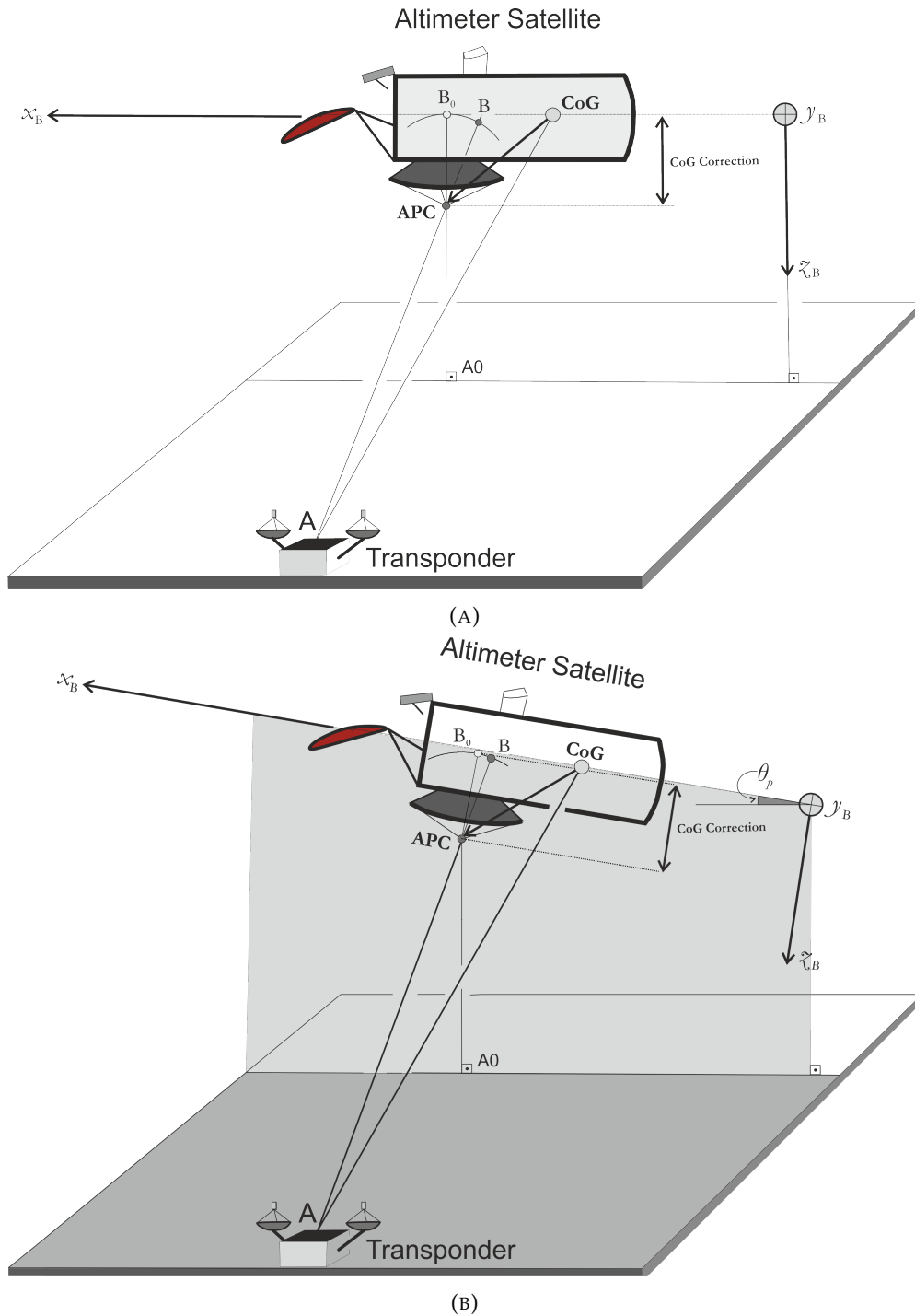
FIGURE 2.23: Altimetric measurement acquisition over a transponder for (a) ideal and (b) non-ideal satellite orientation (when pitch is introduced). The vector with origin the satellite's CoG and end the APC (used in the revised processing) and the axes of the satellite body reference system are also presented.
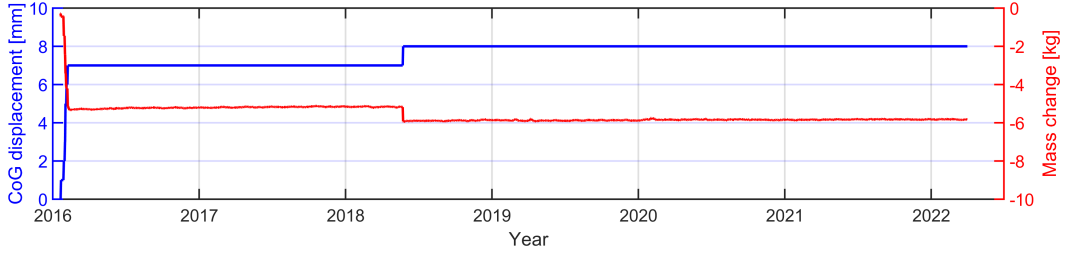
FIGURE 2.24: Jason-3 mass and CoG (x-component) history since
deployment.

Conventions (2010)"). The calculation of $\mathbf{R}_{\text{SAT}\to\text{IRS}}$ can be performed as already discussed in Section 2.2, and the evaluation of vector $\Delta\mathbf{V}_{\text{SAT}}$ is based on the spacecraft geometry and mass properties that are provided in the corresponding mission documentation. The APC and CoG coordinates in the SAT system for Jason-3 and Sentinel-6 MF are given in Table 2.7. During the spacecraft operation, the CoG is subject to a minor displacement over time due to events such as fuel consumption (Figure 2.24). The precise evaluation of $\Delta\mathbf{V}_{\text{SAT}}(t)$ at a specific time epoch t is performed as follows:

$$\Delta\mathbf{V}_{\text{SAT}}(t) = \Delta\mathbf{V}_{\text{SAT}}(t_0) + \delta\mathbf{V}_{\text{SAT}}(t). \tag{2.110}$$

The first term on the right-hand side of Eq. (2.110) denotes the APC–CoG baseline vector as measured prior to the satellite deployment, and the second term denotes its temporal variations due to the CoG displacement (L. Cerri, 2022). The Jason-3 x_B-axis component of the CoG displacement in the SAT system is given in Fig. 2.24, along with the spacecraft mass change. In line with Eq. (2.6), the new datation bias, $\widetilde{dt}$, after referring all parameters to APC is given by:

$$\widetilde{dt} = \arg\min_{t\in\mathbb{R}_+} R(t) - \arg\min_{t\in\mathbb{R}_+} R_0(t). \tag{2.111}$$

We finally define the attitude effect on range and datation bias per cycle (denoted δB and δT, respectively) as the bias difference before and after accounting for non-ideal attitude:

$$\delta B = \widetilde{B} - B, \tag{2.112}$$

and

$$\delta T = \widetilde{dt} - dt. \tag{2.113}$$

Chapter 3

Methods and Results

3.1 Geophysical Corrections

3.1.1 Wet Delays

The altimetric range, measured during calibration with a point target (transponder or corner reflector), should be corrected for the additional path induced by the wet component of the atmosphere (Section 2.2). The wet delay, which affects altimetric signals, is strongly variable temporally and spatially as detailed in Section 2.3. Therefore, the estimation of the corresponding correction is challenging and directly affects calibration's accuracy and robustness. Thus, this dissertation proposes and tests additional methodologies and instrumentation for wet delays correction for improving the calibration of satellite altimeters. Specifically, the insertion of diverse
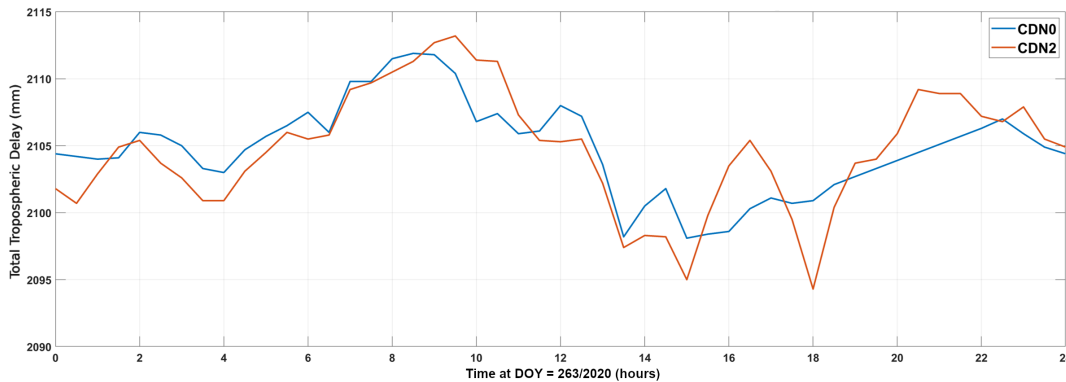
FIGURE 3.1: Wet delays computed using relative positioning.

methodologies concurrently with the established technique exploiting GNSS (Section 2.3), offers important advantages at the calibration. Namely, it increases the redundancy of operational altimetry calibration by having alternative sources for tropospheric delays estimation in the case of a possible instrumentation failure and its validity by comparing results of diverse observations in line with the FRM guidelines (Mertikas et al., 2019).

The difficulty in determining wet delays is reflected in Figure 3.1 by the results' variability, even though they are produced with the same processing methodology (relative positioning) and adjacent GNSS receivers (CDN0 and CDN2) in CDN1 Cal/Val site. Similarly, Figure 3.2 shows variability when applying different methodologies, namely precise point positioning with ambiguity resolution (PPP-AR) and relative positioning on the same measurements of the CDN0 receiver.

Integration of Sentinel-3 OLCI

The OLCI instrument on-board Sentinel-3A & B satellites can be used for estimating wet tropospheric delays as explained in Section 2.3.1 and presented in the work of Mertikas et al. (2020b). Wet delays estimated with OLCI are used for the calibration of satellite altimeters along with the well-established and tested GNSS method (Fernandes et al., 2013; Fernandes et al., 2014).

The wet delays from OLCI were compared against corresponding results calculated using GNSS stations in Crete, Greece for assessing their accuracy and reliability before incorporating them in calibration. The network used in this analysis consists of ten permanent GNSS receivers. Namely, the CDN0, CRS1, MEN2, RDK1, and TUC2 GNSS sites, which are maintained and operated by the Technical University of Crete, and the PALC, RETH, MOIR, HERA and IERA that belong to the HxGN SmartNet RTK network of METRICA S.A. The processing of GNSS observations incorporates precise satellite orbits while the elevation cut-off angle was set at $10°$ and the rate of measurements at 30 s. Additionally, solid-Earth, polar and ocean tides were incorporated into the GNSS processing (Petit and Luzum, 2010a; Lyard et al., 2006).

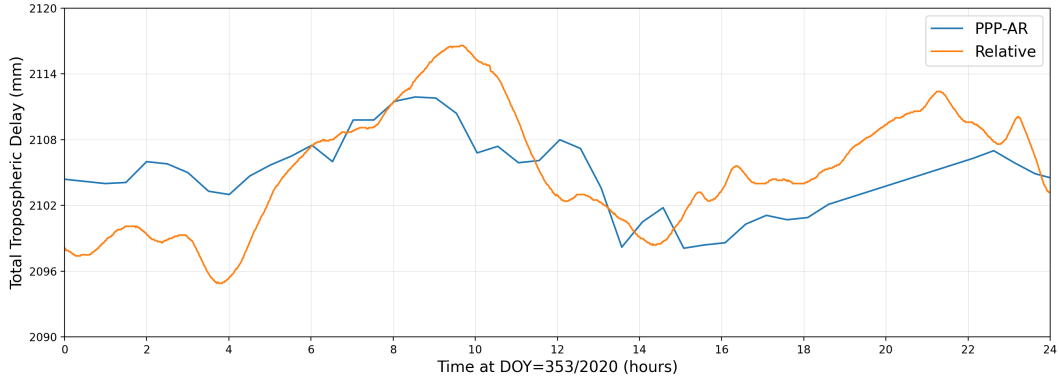It should be noted that CDN0, CRS1 and TUC2 are equipped with meteo sensors, whereas the remaining GNSS stations rely upon atmospheric pressure loading models (Tregoning and Dam, 2005) and the VMF1 model for atmospheric pressure estimation (Boehm and Schuh, 2004). The impact of this different pressure input on IWV and consequently on wet delays was examined before comparing GNSS with OLCI corrections. In particular, the zenith wet delays were estimated at a rate of one minute in CDN0, CRS1 and TUC2 for the entire operational timespan, using the VMF1 model and independently with meteorological measurements. Thus, the difference between the two IWV results can only be attributed to the diverse atmospheric pressure input.

There is strong statistical correlation between IWV using pressure models and measurements in CDN0, CRS1 and TUC2, as presented in Figures 3.3, 3.4 and 3.5. The Pearson correlation coefficient equals to 0.96, 0.98 and 0.98 for CDN0, CRS1 and TUC2 respectively while the mean bias is on the sub-millimeter level. The R^2 coefficient is greater than 0.92 in every case, which denotes that the results are statistically significant for all three stations. Thus, the different pressure source does not affect the IWV estimation and both sources will be applied in the sequel at the comparison of GNSS with OLCI.
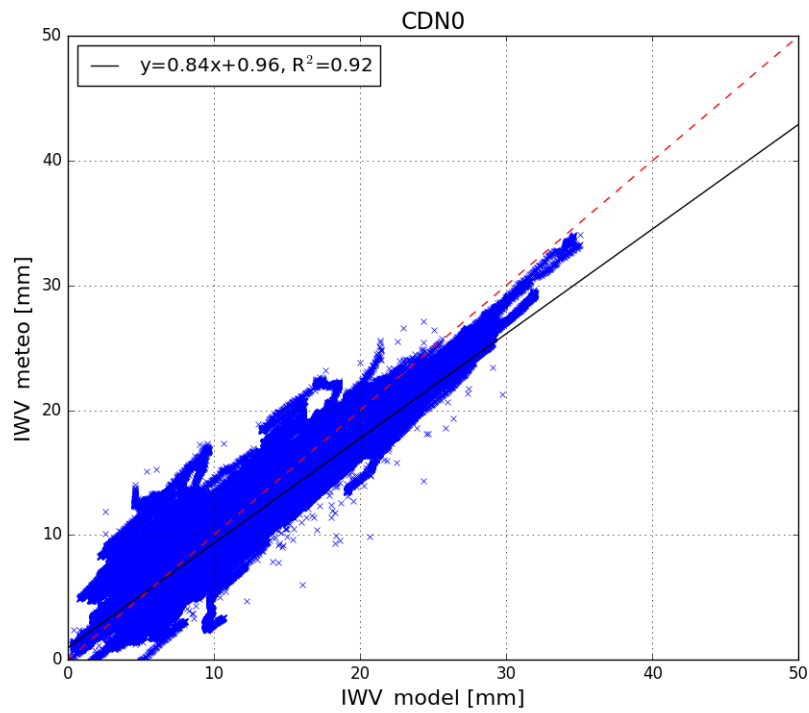
FIGURE 3.3: IWV estimated with the VMF1 model (x-axis) and with in-situ meteo observations (y-axis). The linear regression line is provided along with the R^2 value.
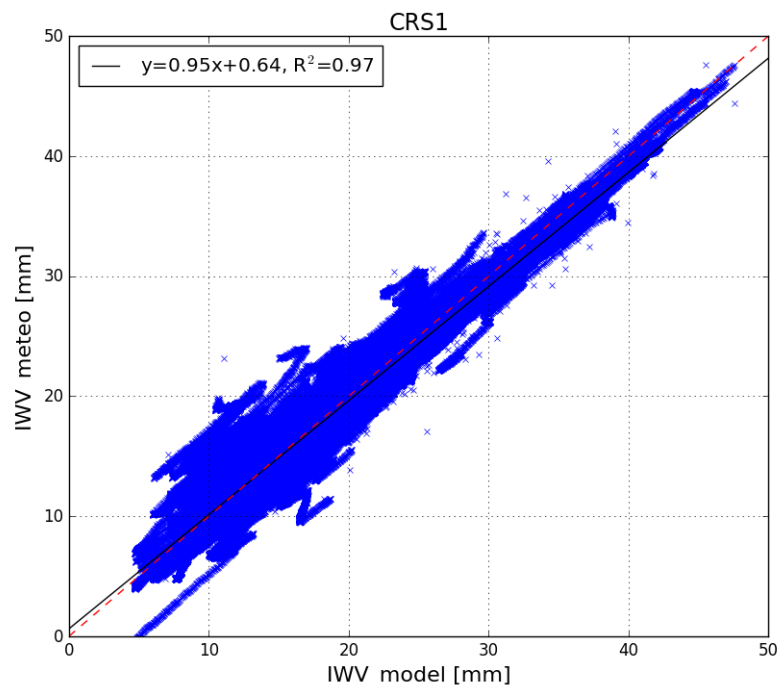
FIGURE 3.4: IWV estimated with the VMF1 model (x-axis) and with in-situ meteo observations (y-axis). The linear regression line is provided along with the R^2 value.
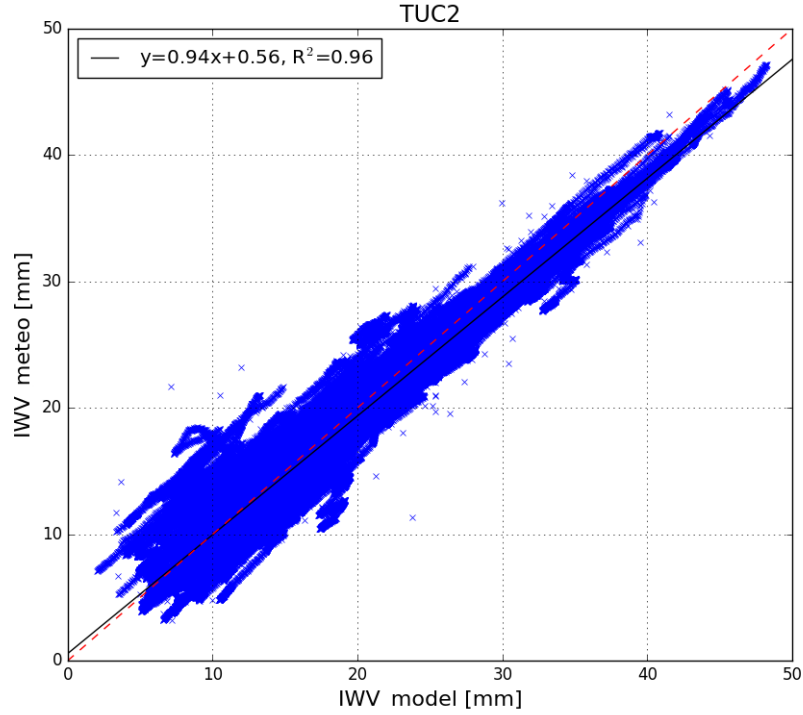
FIGURE 3.5: IWV estimated with the VMF1 model (x-axis) and with
in-situ meteo observations (y-axis). The linear regression line is pro-
vided along with the R^2 value.

The OLCI dataset consists of images that contain the entire island of Crete in
order to have simultaneous comparison with all GNSS sites. This criterion is fulfilled
by twelve passes of Sentinel-3A & B with numbers 7, 21, 64, 78, 121, 135, 178, 235,
278, 292, 335, and 349 as presented in Table 3.1. The OLCI products that contain the
necessary bands (described in Section 2.3.1) for the estimation of IWV are the Level
2 Land Full Resolution (OL_2_LFR). These data were acquired from the Copernicus
Open Access Hub [1]. The spatial resolution of OL_2_LFR is 300 m and thus a value
of IWV is obtained for every 300 m pixel.

Two methods were followed for the determination of IWV from an OLCI image.
The first one is the nearest neighbour, in which the GNSS IWV is compared with the
IWV value of the closest pixel in the OLCI image. A similar approach was followed
in Carbajal Henken et al. (2020) to compare GNSS with Moderate Resolution Imag-
ing Spectroradiometer (MODIS) IWV results. In the second approach, the GNSS
IWV value is compared with the average IWV of a 31 × 31 pixels area (with area
around 9.3 km^2) centered to the GNSS station location. Approximately, area of the
same size was selected in the work of Makarau et al. (2016). This method is applied
to approximate the fact that the zenith total delay in GNSS originates from slant
paths towards observable satellites (Lindenbergh et al., 2008). Hence, the 31 × 31
pixel area has been selected to simulate the GNSS area of influence for the wet delay
estimation. Only pixels that are characterized as "LAND" (which denotes surface of
land with clear sky) has been including into the IWV averaging.

The distribution of IWV$_{OLCI}$ − IWV$_{GNSS}$ is examined, before moving to GNSS
and OLCI scatter plots and the quantification of their statistical correlation with the

---

[1] https://scihub.copernicus.eu

TABLE 3.1: Cycles with invalid measurements at every pixel are characterized as "defective" and were excluded from the analysis.

Orbit No.	Sentinel-3A		Sentinel-3B	
	Cycle No.	Defective Cycle No.	Cycle No.	Defective Cycle No.
7	4 – 55	17	21 – 34	25, 26, 27, 28
21	4 – 55	21	21 – 34	24
64	4 – 55	–	21 – 33	23, 24, 25
78	4 – 55	12, 14, 16, 23	24 – 33	27
121	4 – 55	30, 38, 41	21 – 33	24, 31
135	4 – 55	4, 12, 37	22 – 33	24
178	4 – 55	10, 43	22 – 33	23, 24
235	4 – 55	38	23 – 33	–
278	4 – 55	–	21 – 33	24, 25
292	3 – 55	12	20 – 33	25
335	3 – 55	27	21 – 33	–
349	3 – 55	14	21 – 33	24, 25, 26, 27

Pearson correlation coefficient. The histograms of each station are presented in Mertikas et al. (2020b) along with the theoretical line (denoted with red color) of normal distribution with parameters the average value and the standard deviation of the data. It is evident in Mertikas et al. (2020b) that the distribution of IWV differences follows at a sufficient extend the normal (or Gauss) distribution for every station. The ranges of x and y-axis were kept constant for every case to directly compare the average values and standard deviations. The average value and standard deviation of the IWV differences are provided in Table 3.2 for both single-point and area-of-influence approaches regarding the Sentinel-3A OLCI imaginary. For the RDK1 station the single-point approach could not be performed since the closest OLCI pixel to the station was marked as "WATER" and had an error of approximately 25 mm. Thus, it was excluded from the analysis as presented in Table 3.2 in which there are no values for the RDK1 single point. As can be seen from Table 3.2 the average IWV differences between OLCI and GNSS are at the order of mm except the case of RDK1 with −4 mm. This higher difference is attributed to the presence of "WATER" pixels in the 31 × 31 pixels area of influence as mentioned before.

Scatter plots of IWV determined by OLCI and GNSS are applied to investigate the correlation between the two independent techniques. To quantify whether a method overestimates the IWV compared and determine their relative bias, a linear regression line along with the corresponding R^2 value is calculated for each scatter plot. The scatter plots are provided for both area of influence (Figure 3.6) and single point (Figure 3.7) approaches. It should be noted that the criteria to take into consideration an IWV estimation from OLCI is to have the pixel marked as "LAND" and its IWV error being lower than 2 mm.

Additionally, the Pearson correlation coefficient along with the corresponding significant value (p-value) is determined and presented in Table 3.3. In Figures 3.6

TABLE 3.2: The average value (Average) and standard deviation (SD) for the IWV difference between GNSS stations and Sentinel-3A OLCI for both single-point (SGL) and area-of-influence (AOI) approaches.

Site	$\text{OLCI}_{\text{SGL}} - \text{GNSS}$		$\text{OLCI}_{\text{AOI}} - \text{GNSS}$	
	Average (mm)	SD (mm)	Average (mm)	SD (mm)
CDN0	−1.1	±2.4	+2.3	±2.6
CRS1	+1.4	±2.7	−0.6	±2.0
HERA	+1.9	±2.0	+0.9	±1.6
IERA	+1.2	±2.3	−0.8	±1.8
MEN2	−0.6	±1.7	−1.1	±1.6
MOIR	+0.9	±2.0	+0.6	±1.6
PALC	+1.0	±2.3	−1.4	±1.6
RDK1	–	–	−4.1	±2.7
RETH	+1.1	±2.1	+1.0	±1.6
TUC2	+0.3	±2.1	+0.9	±1.9

TABLE 3.3: The parameters of the linear regression lines of Figures 3.6 (average) and 3.7 (single) along with the Pearson correlation coefficient are presented.

Site	Offset (mm)		Slope		R^2		Pearson	
	Single	Average	Single	Average	Single	Average	Single	Average
CDN0	−0.26	1.71	0.93	1.04	0.80	0.81	0.89	0.89
CRS1	1.08	−0.58	1.01	0.99	0.86	0.93	0.93	0.96
HERA	0.11	−0.31	1.09	1.06	0.94	0.96	0.97	0.98
IERA	0.24	−0.79	1.05	0.99	0.90	0.93	0.95	0.96
MEN2	0.47	−0.33	0.95	0.96	0.93	0.94	0.96	0.97
MOIR	−0.23	−0.14	1.06	1.03	0.93	0.95	0.96	0.97
PALC	0.73	−0.74	1.02	0.97	0.89	0.94	0.94	0.98
RDK1	–	−2.16	–	0.91	–	0.84	–	0.92
RETH	1.02	0.48	1.00	1.03	0.91	0.95	0.96	0.97
TUC2	−0.63	−0.54	1.05	1.07	0.92	0.94	0.96	0.97

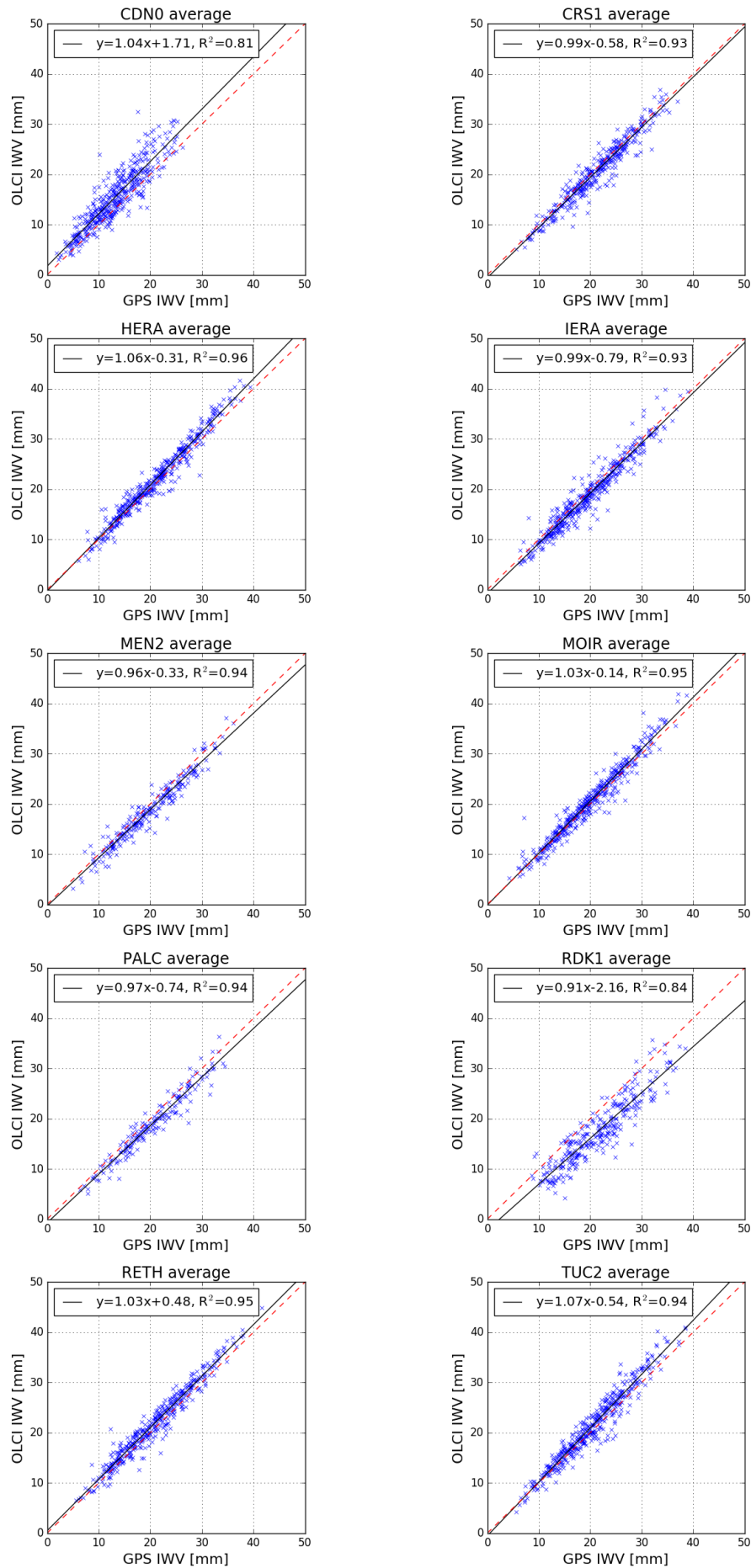FIGURE 3.6: Scatter-plots of IWV determined using the Sentinel-3A OLCI (area of influence approach) with IWV from GNSS stations. The red dashed line denotes the linear regression line and the black the bisector.
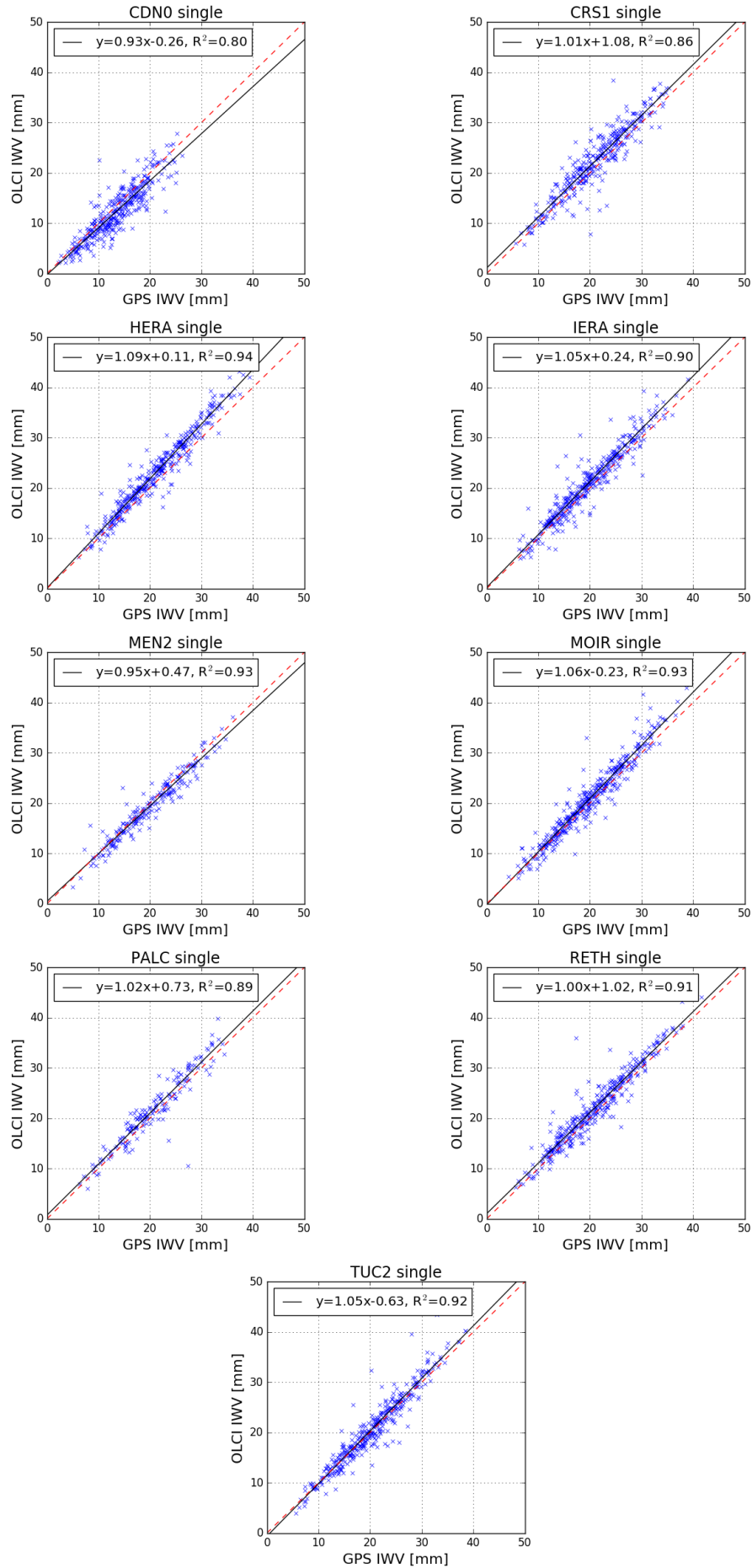
FIGURE 3.7: Scatter-plots of IWV determined using the Sentinel-3A OLCI (single point approach) with IWV from GNSS stations. The red dashed line denotes the linear regression line and the black the bisector.

and 3.7 denote that there is agreement of IWV from the two independent methodologies of OLCI and GNSS in every case. Additionally, the data of the scatter plots are well distributed close to the bisector line (with red color) without observing some clear deviation between the IWV determined by OLCI and GNSS. The parameters of the linear regression lines are presented in Table 3.3 and denote that there is strong correlation between the IWV from OLCI and from GNSS. Indicatively, in every case the Pearson coefficient is higher than 0.80 and statistically significant with p-value < 0.003. There are some differences between the results from the single-point and area-of-influence approaches. However, in both cases the results are sufficiently compatible with these derived from GNSS. The presented investigation for Sentinel-3A OLCI ($OLCI_A$) was also performed for the OLCI ($OLCI_B$) on-board Sentinel-3B and the detailed analysis can be found in the work of Mertikas et al. (2020b).

To quantify the offset between $OLCI_A$ and $OLCI_B$ with the regional GNSS network as well as their relative difference, the corresponding biases have been determined. The bias of $OLCI_A$ or $OLCI_B$ with the GNSS stations is defined as absolute and the difference between the two OLCI as relative. Specific criteria were set for the inter-comparison between the OLCI on board the two Sentinel-3 satellites. To begin with, (1) the IWV selected originate from $OLCI_A$ and $OLCI_B$ measurements over the same ground area, which are the locations of the GNSS stations, (2) both instruments should have valid measurements, (3) concurrent observation and (4) have GNSS results with the same time-tagging.

The last criterion was chosen to create pseudo-simultaneity between the measurements of $OLCI_A$ and $OLCI_B$. This is necessary because Sentinel-3A imagery is referenced at 08:12 UTC, while Sentinel-3B at 08:51 UTC for the same date. Thus, to compensate for the IWV variation originating from the acquisition at different times, we used the corresponding IWV offset between the GNSS results at 08:12 UTC and 08:51 UTC. The GNSS offset was applied at the IWV value of $OLCI_B$ to reference it at the time of $OLCI_A$ i.e., 08:12 UTC.

The main findings of the comparison between the methodology based on OLCI and GNSS for IWV estimations (which defines the absolute bias) and the IWV differences between OLCI on board Sentinel-3A and Sentinel-3B satellites (that is expressed by the relative bias) are:

- The absolute bias of $OLCI_A$ is -0.23 mm and $+0.57$ mm for the area-of-influence and single-point approaches respectively.

- The absolute bias of $OLCI_B$ is $+0.24$ mm and $+1.07$ mm for the area-of-influence and single-point approaches respectively.

- The relative bias of OLCI ($OLCI_B$ - $OLCI_A$) is at the order of $+3$ mm or in other words $OLCI_B$ overestimates IWV by around $+3$ mm.

As a general conclusion, the IWV retrieval from both $OLCI_A$ and $OLCI_B$ can be used as a diverse and redundant methodology concurrently with other techniques (e.g., GNSS) for satellite altimeters calibration.
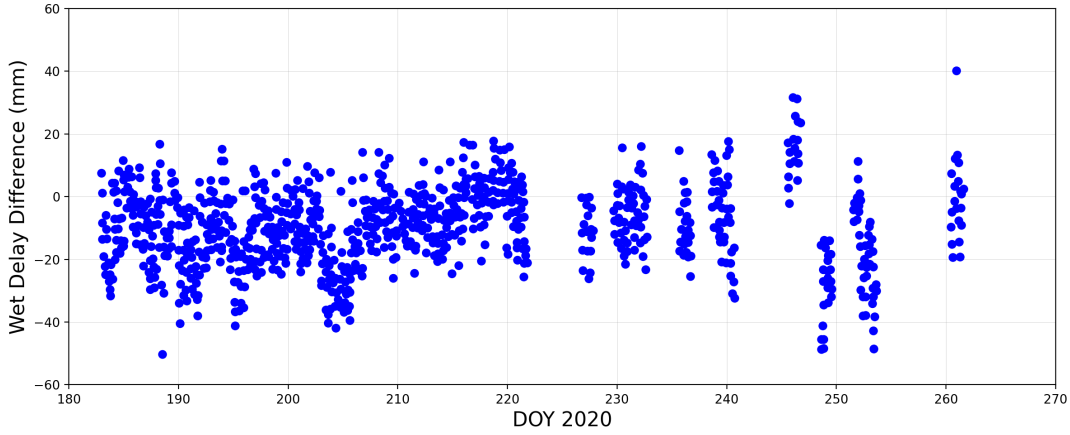
FIGURE 3.8: The difference between wet delays estimated using the
MP–3000A radiometer against these from the CDN0 GNSS station.

Integration of Radiometer

As described in Section 2.3.1 microwave radiometers (on-board satellites or on Earth's surface) can be used for the estimation of the IWV or in other terms for the wet delays corrections on satellite altimetry signals. In this dissertation, a ground radiometer was incorporated for satellite altimeters calibration as an additional and independent method of determining the wet delay correction. Particularly, the MP–3000A microwave radiometer by Radiometrics was installed in the CDN1 Cal/Val site. We calibrated the radiometer using liquid nitrogen (target of known thermal radiation) at the premises of the Technical University of Crete to assure its optimal operation. After this procedure, the radiometer was installed at the CDN1 station.

Similarly to OLCI, a comparison of radiometer against the well-established GNSS methodology was conducted before including OLCI operationally into calibration. To check the validity of the ground microwave radiometer in CDN1, we used estimations of wet delays by a GNSS receiver located at the same site. The period of concurrent measurements in the present analysis, spans for about three months with a sampling interval of five minutes.

The gaps in Figure 3.8 correspond lack of data from the GNSS and/or ground radiometer. This station is not connected to the power grid and the high energy consumption of ground radiometers led to insufficient power. As far as the comparison between the two techniques presented in Figure 3.8 the radiometer tends to underestimate the wet delays compared with the GNSS. Specifically, the average value of the wet delays difference (radiometer - GNSS) is -9 mm with a standard deviation of 12 mm. This level of difference is anticipated because of the high temporal and spatial variability of wet delays. The software used for determining all the previous wet delays with GNSS is the GAMIT. This software is commonly used for similar analyses such as these presented in Fernandes and Lázaro (2018), Fernandes et al. (2014), Fernandes, Nunes, and Lázaro (2013), and Fernandes et al. (2013).

Additionally, the results derived from GNSS processing with Gipsy were included, to further investigate the results of wet delays from independent sources. The Gipsy software is based on precise point positioning and GNSS satellites observations. Thus, it is a redundant technique to the relative positioning of GAMIT, which relies upon other nearby GNSS stations. For eight calibrations over CDN1, the wet delays were estimated with Gipsy and GAMIT using the GNSS receiver in CDN1 and the microwave radiometer (Figure 3.9). The results on Figure 3.9 indi-
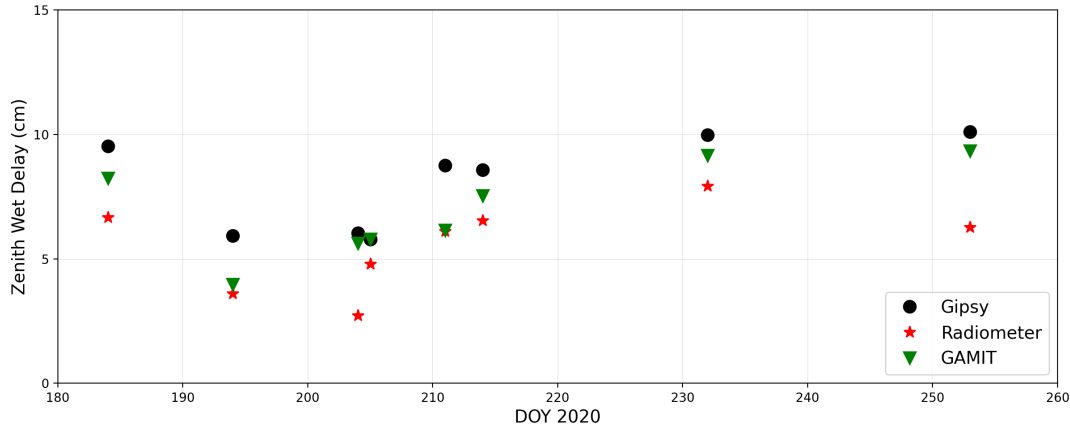
FIGURE 3.9: Wet delays using the MP–3000A radiometer and CDN2 GNSS receiver processed with Gipsy and GAMIT are provided.

cate the variability of wet delay determined using different methodologies. Even though the statistical sample of Figure 3.9 is small it coincides with the conclusion from Figure 3.8 that the radiometer underestimates the wet delay compared with the results derived from GNSS. This supports the need for diverse techniques and instrumentation for the simultaneous estimation of wet delays. Thus, the addition of independent techniques for determining wet delays is beneficial for the final accuracy and validity of the calibration.

3.1.2 Point Target Positioning

There are applied simultaneously two techniques of GNSS positioning in this dissertation for the calibration of satellite altimeters. The diverse methodologies are implemented in order to follow the FRM guidelines. In particular, to increase the robustness of calibration by having alternative methodologies and the confidence of the final positioning by combining independent results. Namely, these methodologies are precise point positioning and relative positioning, explained in Sections 2.4.1 and 2.4.2, respectively. The Gispy 6.4 and Gipsy-X of the Jet Propulsion Laboratory (Webb, 1993; Lichten, 1995; Sibois et al., 2017) was applied throughout my PhD for precise point positioning, while the relative positioning was performed through the **GNSS A**t **MIT** (GAMIT), provided by the Massachusetts Institute of Technology (MIT) (Herring, King, and McClusky, 2006; Herring, King, McClusky, et al., 2010; Yalvac, 2021). The GNSS receivers along with their antennas in CDN1 and GVD1 Cal/Val sites that are used for transponder calibration are presented in Table 2.2.

In both techniques, the absolute coordinates determined by the GNSS processing refer to the position of GNSS antenna's phase center. However, the necessary parameter for calibration is the absolute position of the point target's reference point. These coordinates are necessary for calculating the geometrical distance between the point target and the orbiting satellite. Thus, an extra step is required to calculate the absolute position of the point target based on the known coordinates of the GNSS antenna. This transfer is realized with geodetic techniques that introduce an error at the order of mm (Avram, Bratosin, and Ilie, 2016).

As shown in Figures 3.10, 3.11, 3.12, 3.13, 3.14 and 3.15, the time series originating from the two diverse solution show similar behaviours. Specifically, there are

FIGURE 3.10: The North component as calculated using GAMIT (top) and Gipsy (bottom).

FIGURE 3.11: The East component as calculated using GAMIT (top) and Gipsy (bottom).

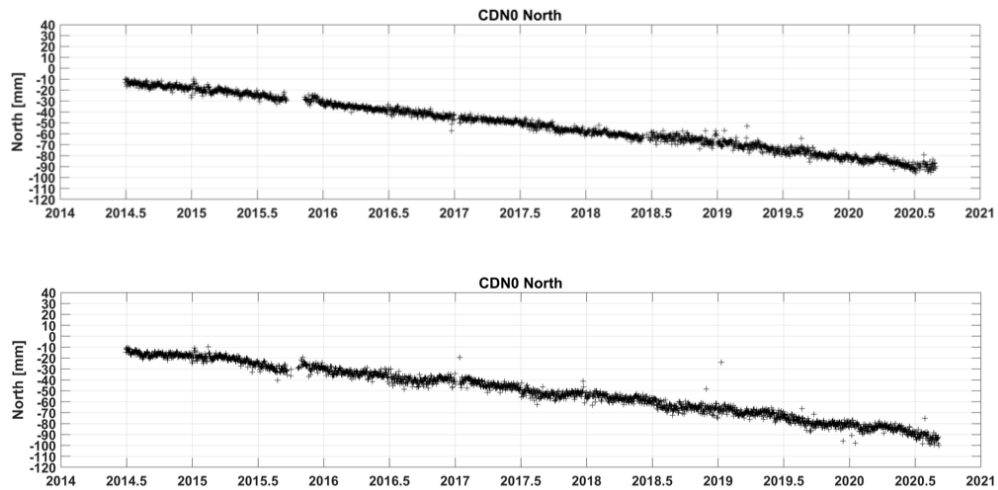FIGURE 3.12: The Up component as calculated using GAMIT (top) and Gipsy (bottom).

FIGURE 3.13: The North component as calculated using GAMIT (top)
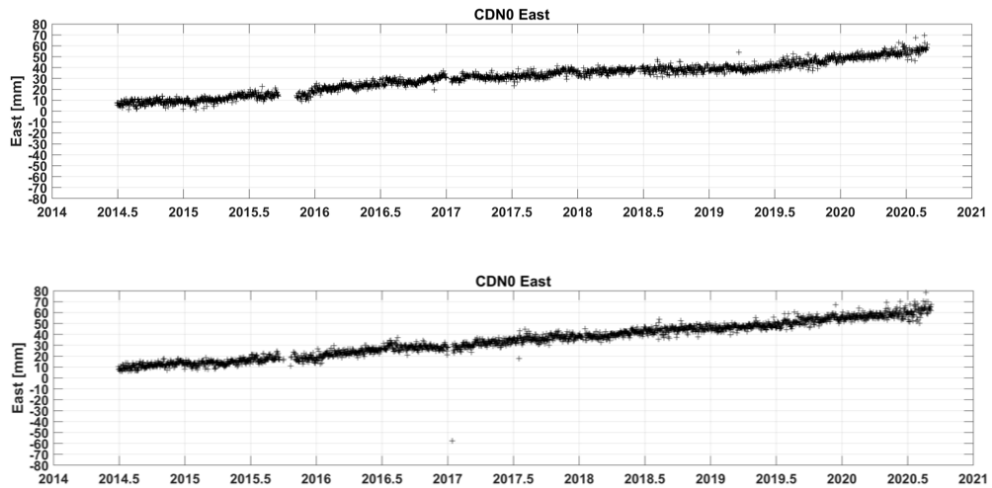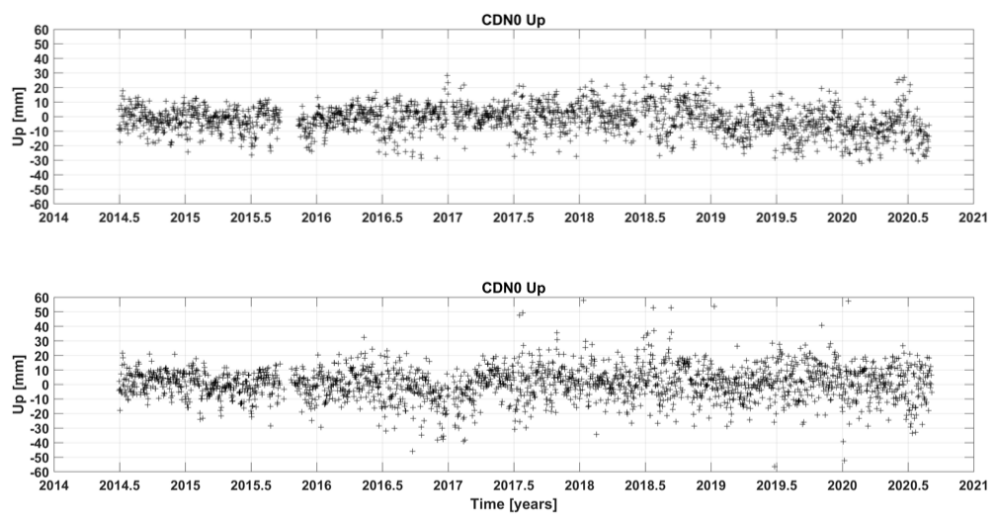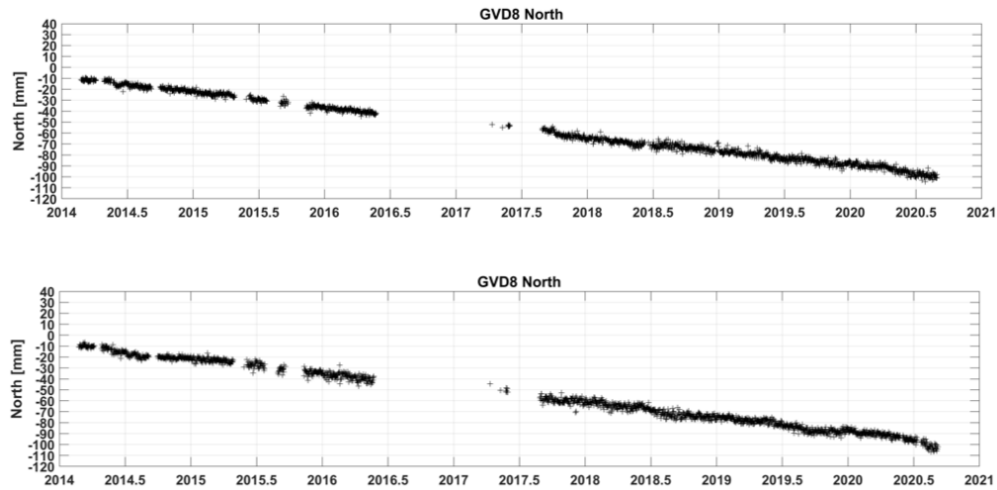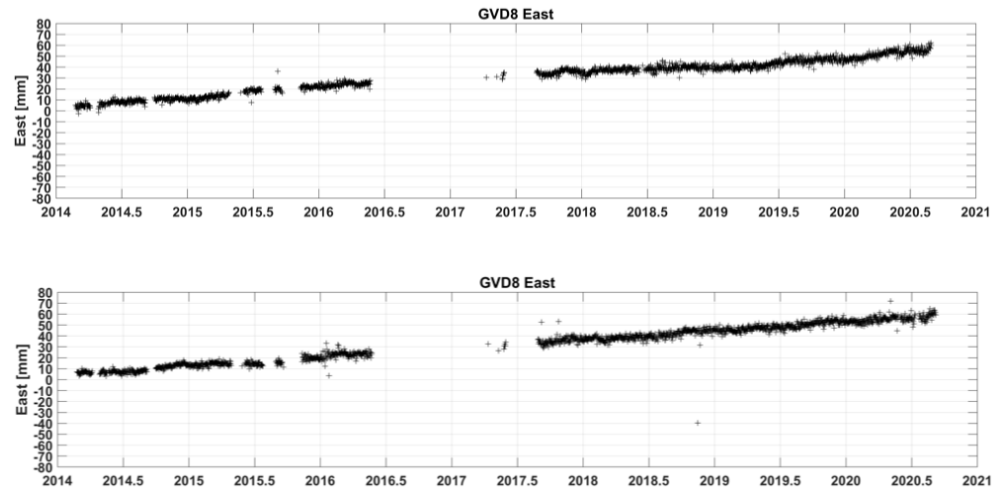and Gipsy (bottom).

FIGURE 3.14: The East component as calculated using GAMIT (top)
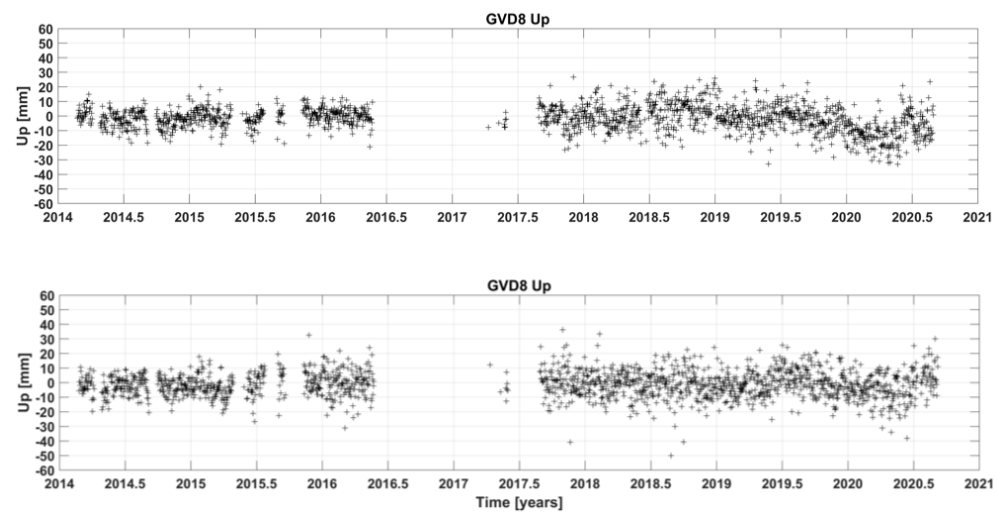and Gipsy (bottom).

FIGURE 3.15: The Up component as calculated using GAMIT (top)
and Gipsy (bottom).

TABLE 3.4: The coordinates and velocities of CDN0 and GVD8 stations calculated using GAMIT and Gipsy at epoch 2013.5.

Station	Software	X (m)	Y (m)	Z (m)
CDN0	GAMIT	4767408.6178	2100658.5740	3669108.1804
	Gipsy	4767408.6182	2100658.5734	3669108.1813
GVD8	GAMIT	4782603.4083	2141348.9745	3624048.9145
	Gipsy	4782603.4091	2141348.9753	3624048.9136

Station	Software	V_x (m/yr)	V_y (m/yr)	V_z (m/yr)
CDN0	GAMIT	0.0027	0.0096	−0.0111
	Gipsy	0.0033	0.0088	−0.0119
GVD8	GAMIT	0.0038	0.0100	−0.0116
	Gipsy	0.0030	0.0105	−0.0107

common inclinations, periodic effects, and gaps. However, there are some clear differences between the components calculated using GAMIT and Gipsy. Generally, Gipsy time series show higher variability compared to these of GAMIT. Additionally, in Gipsy results there are some steps in the y-axis, which are not present in GAMIT solutions. An example of such a case can be seen around decimal year 2015.75 in Figure 3.10. These characteristic differences originate from the diverse methodologies of Gipsy and GAMIT for determining coordinates. Gipsy processing exploits only GNSS satellites' observations whereas GAMIT solution is based on other ground stations. Therefore, the multiple vectors connecting the various stations, create a mesh which reduces the level of freedom and lead to a more "smoothed" final solution.

Among the East, North and Up components, the higher variability can be detected in the Up of both GAMIT and Gipsy. However, the higher error of the vertical component commonly known in GNSS positioning. Moreover, the periodical constituents are more pronounced in GAMIT time series of the Up component. This can be attributed to the connection with other ground stations that experience the same tides (solid Earth tide, ocean tide, pole tide) and non-tidal effects (atmospheric and water loading) with the CDN1 GNSS receiver. Another explanation of the more prominent periodicity is the lower dispersion of GAMIT solution which allows to clearly detect this characteristic.

The coordinates of the station are extracted for a specific epoch and then transferred to different time instants (e.g., at the epoch of a calibration) with the assumption of linear velocity. This solution is called tide-free since the linear velocity removes periodical effects. The aforementioned tides and non-tidal effects should added in order to obtain the "true" position of the GNSS station. The difference between GAMIT and Gipsy in determining the coordinates of CDN0 and GVD8 is at the level of sub-mm and mm/yr for velocities, as presented in Table 3.4.

3.2   Calibration With Corner Reflectors

According to the FRM strategy for altimetry, every component in calibration processing should be produced by diverse methodologies and instrumentation in order to
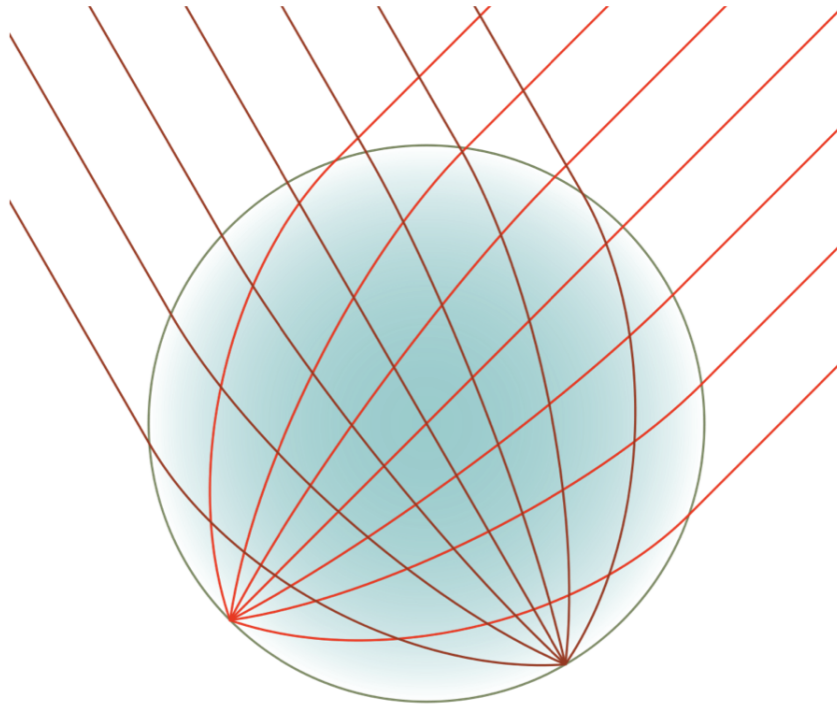
FIGURE 3.16: Cross section of a Luneburg lens. The gradient color denotes the decreasing refractive index n from the center towards the surface of the lens. The path of two groups of incident arrays and their reflection is also presented.

have redundancy and cross-evaluation among different results. Even though all the main calibration parameters are simultaneously produced by independent sources, the main constituent the altimetric range, is measured by only one type of point target in PFAC, an active microwave transponder. Hence, the need for complementing transponders with a diverse target arose. The first step of this dissertation was to identify the potential targets that offer altimetric signal enhancement and thus been detectable by the satellite altimeter. There are several techniques to achieve signal amplification in order to have a target separable by the target.

One approach is to specially design the shape and dimensions of a target and hence obtain strong reflection at specific aspect angles and thus satellites. This option was rejected because it is an ad hoc solution, which restricts the use of such calibration targets only at a particular mission, reduces their operational life and eliminates the capacity for cross-calibration among different missions.

The second method examined was to use targets with impedance loading (also known as reactive loading). This solution was rejected because we sought passive targets (it will be justified in the sequel) and also because of their complexity. The latter results into increased possibility of fault operation at Cal/Val sites that are controlled remotely through telecommunications.

The third solution for signal enhancement, was the application of targets with multiple scatterings such as retrodirective arrays, dielectric lenses, and corner reflectors. Retrodirective arrays (Figure 3.17) were deselected because again they are active targets (incorporate electronic components) whereas we need passive targets to complement the microwave transponder. The second category exploiting multiple scatterings, is the dielectric lenses. Some characteristic examples of this category are the cylindrical Eaton-Lippman lens, the spherical lenses of Kay and the Luneberg
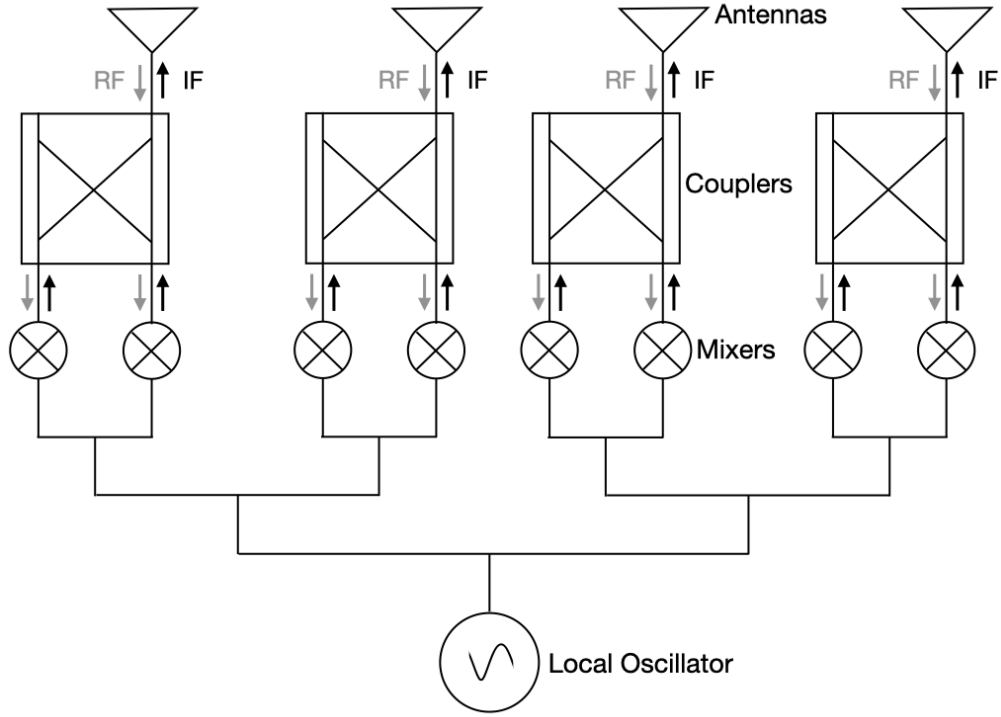
FIGURE 3.17: Schematic diagrams showing the typical design of retrodirective arrays in which RF and IF denote Radio Frequency and Intermediate Frequency respectively.

lens. The latter is an interesting kind of lens that is based on the characteristic of spherically symmetrical gradient of refracting index (Figure 3.16). Luneburg lenses are transformed into radar targets by metallizing part of their outer surface in order to reflect the signal towards its source. These targets accumulate a plethora of preferable characteristics, such as the strong maximum radar cross section that equals to $4\pi^3\alpha^4/\lambda^2$, where α is the dimension of the reflector (Ruck, Barrick, and Stuart, 2002). However, their complex structure results into higher possibility of manufacturing failure and deformations during outdoor operation that will degrade their signal amplification and effectiveness as reference targets. On the contrary, we need robust targets for continuous operation that will calibrate multiple altimeters. Therefore, we finally selected corner reflectors as targets for satellite altimeters calibration. In Sections 2.5.4 and 3.2.1 more details are provided on the specific orientation of target's maximum back-scattering, corner reflector's placement configuration, type, dimension and material of the final design proposed for altimeter calibration.

This dissertation proposes and justifies the application of corner reflector for measuring the altimetric range almost simultaneously (with a difference of a few seconds) with an active transponder. The operation of a corner reflector for satellite altimeter calibration has already been demonstrated in the work of Gibert et al. (2023). There is a fundamental difference between the two targets which is the core motivation of proposing their tandem operation. Specifically, transponders are active (i.e., electronically amplify the incoming signal), while corner reflectors are passive (i.e., their echo originates only from the apparent area as seen by the radar and depends on their physical structure). Consequently, there are diverse error sources affecting corner reflectors and transponder calibration. Therefore, their simultaneous operation can be used to estimate the inherent errors of each methodology. The

dominant uncertainty of transponders, arises from the determination of the exact value of their internal delay. Moreover, how the internal delay varies with operating conditions (e.g., temperature, humidity) and its change over time (drift) caused by aging electronic components. On the contrary, corner reflectors do not introduce delay to the reflected signal, as proved in Section 2.5.4. Hence, corner reflectors can be used in order to independently estimate at every pass, the transponders' internal delay and mitigate this uncertainty.

At the same time, transponders are preserved as the main reference target because of their stronger amplification which reduces bias variability. It is important to note, that active transponders have stronger gain which results into higher signal to noise ratio compared to passive targets. Therefore, active transponders can be detected even in cases of high clutter and/or high atmospheric absorption. As far as the calibration algorithms, transponders can be used at Low Resolution Mode, SAR and Fully Focused Synthetic Aperture Radar (FFSAR) processing whereas corner reflectors are limited only to FFSAR because of their lower gain. On the other hand, the lack of electronic components in corner reflectors allows higher operational life expectancy and multi-frequency capability and zero internal delay. Thus, these targets can be used as reference to combine results from satellite altimeters and transponders of different generations and/or location. Consequently, the optimal scenario, which is proposed in this work, is the concurrent operation of both targets.

3.2.1 Absolute Calibration

This dissertation provides the optimal corner reflector design for calibrating satellite altimeters simultaneously with an active target i.e., transponder at the same calibration network. Particularly, we propose a rectangular trihedral corner reflector with a dimension of 1.5 m, manufactured by the 5083 aluminium alloy. Calibration with the corner reflector as reference target will be performed using the FFSAR. Manufacturing requirements are the perpendicularity of plates with an error of $0.1°$, flatness of plates with an error less than 0.5 mm and no surface imperfections on the plates greater than 0.5 mm (Jauvin et al., 2019). The justification for every one of these characteristics will be analyzed. To begin with, the selected type of rectangular corner reflector resulted from the criterion of maximum radar cross section for a given dimension (Figure 3.18). This criterion was set in order to have a target which is clearly separable from the area's clutter but at the same time not too bulky. Hence, the portability feature, the reduced probability of manufacturing failures and the reduction of loads from atmospheric phenomena (e.g., wind) are achieved. In Figure 3.18a the radar cross section is given as a function of the plates' dimension, which is the independent variable of the max radar cross section function. Additionally, in Figure 3.18b the radar cross section is presented as a function of the plates surface area, which is more representative of the mass of the corner reflector.

The decision about the dimension of 1.5 m was determined by the necessity to combine the feature of calibrating altimeters of different frequencies (e.g., Ku and Ka) and the reduction of forces acting on the corner reflector in the field. An outdoor operating corner reflector experiences forces from the wind and loads from snow and rain. These forces are proportional to the reflector's dimensions. Thus, larger targets require stronger reinforcement for maintaining the requirements of plates perpendicularity and flatness. This complicates the manufacturing process and excludes calibrating sites with extreme weather conditions such as the CDN1. Moreover, the available sheets of 5083 aluminium alloy have a width limitation of
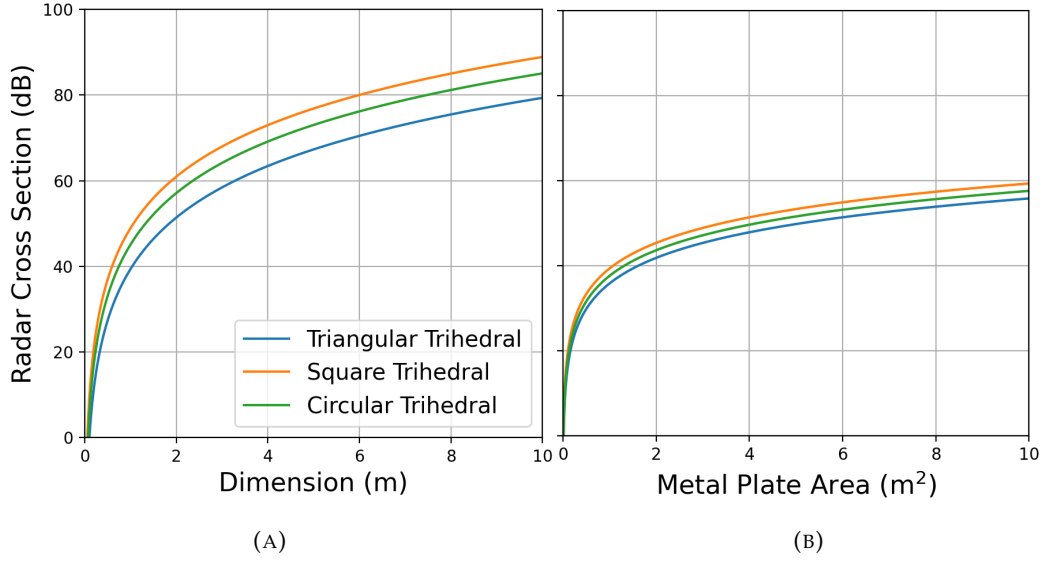
FIGURE 3.18: The radar cross section of different types of corner reflectors as a function of their plates dimension in (A) and total plates area in (B) at 13.575 GHz.

1.5 m. The selected dimension was this of 1.5 m which corresponds to a radar cross section of about 56 dB for 13.575 GHz.

The radar cross-section is proportional to the frequency of the incident signals, as presented in Figure 3.19. Thus, if a corner reflector is detectable from the clutter with Ku signals, then it also stands out in Ka. The material that was selected for the corner reflector manufacturing is aluminium. This element has the higher conductivity compared to all other metals and high relative (compared to its mass) strength. The only metals with higher conductivity are (in descending order): silver, copper, and gold. Specifically, the 5083 aluminium alloy is proposed, with additions of magnesium (4.0 to 4.9%), copper (0.1% max), iron (0.4% max) and others. This is the strongest of the alloys (excluding heat treated alloys) and it is resistant to sea water. Thus, it has intrinsic rigidity which reduces the need of external supporting structure. Additionally, its resistance to sea water allows deployment at sites near coasts.

The proposed orientation of the corner reflector is to point the axis of maximum radar cross section (azimuth angle 45° and elevation 54.74°) toward the zenith. It should be noted that rectangular corner reflectors have a coverage of around 23° around the symmetry axis (Table 2.6). Thus, their effectiveness as radar targets is not sensitive to their pointing accuracy. However, this orientation is preferable for the nadir looking altimeters because it minimizes the possibility of multi-path effects.

3.2.2 Altimeter Differential Corner Reflector

This Section proposes the ADCR new methodology of calibrating satellite altimeters using at least two corner reflectors simultaneously (Figure 3.20).

The key point of this methodology is that at least two corner reflectors are inside the same tracking window of a satellite altimeter and their response is detected concurrently. The corner reflectors are deployed at the same site, with a height difference of 10 m between their apexes (phase centers) because a usual value of an altimeter range bin is around 0.4 m. Thus, the targets signals are placed at distance
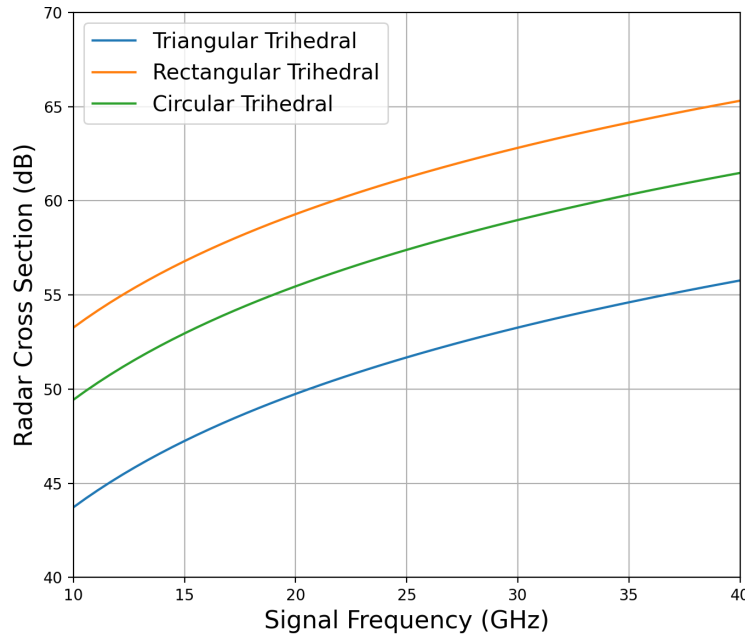
FIGURE 3.19: The radar cross section of different corner reflector types (with 1.5 m dimension) as a function of the incident radiation frequency.

range bins and each signature is distinguishable. The elevation difference is realized by exploiting the physical inclination of the region or by installing artificial bases. The targets should have a distance of 100 m along the track of the satellite being calibrated. In this way, the targets' signals are distinguishable with FFSAR processing and its spatial resolution of about 0.5 m along track (Egido and Smith, 2016; Scagliola and Guccione, 2020). The along track distance of 100 m is proposed in order to assure that the corner reflectors are at different along track strips of 0.5 m (FFSAR) for multiple missions (i.e., Sentinel-6 MF, Sentinel-3A and Sentinel-3B) that have different inclinations. The proposed configuration offers the capability of retracking simultaneous responses from corner reflectors with known relative coordinates (at the order of mm). Thus, the difference between the measured ranges of the two corner reflectors can be estimated and compared with their geometric distance calculated using their coordinates. This comparison will result into the altimetric differential bias.

The main advantage of the proposed methodology is that it is free of the errors related to geophysical and atmospheric corrections applied on measured and geometrical range, presented in Equation (2.1) and (2.2) respectively. The previous statement is justified because the targets are co-located and thus their signals experience the same atmospheric delays which are canceled out with subtraction. Furthermore, the additional constituents that should be added to their tide-free coordinates and thus get their "true" position are identical, since they are at the same site. Consequently, the aforementioned errors are cancelled out. One other interesting feature of the differential calibration is that it allows to determine an additional datation bias between the two measurements. As explained in Section 2.2, the datation bias is defined as the difference between the time that the measured range reaches its minimum with the corresponding time of the geometrical range. In this datation bias, the TCA determined by orbital data is taken as the correct value and is compared with the TCA from the altimeter's measurements. On the other hand, in the proposed
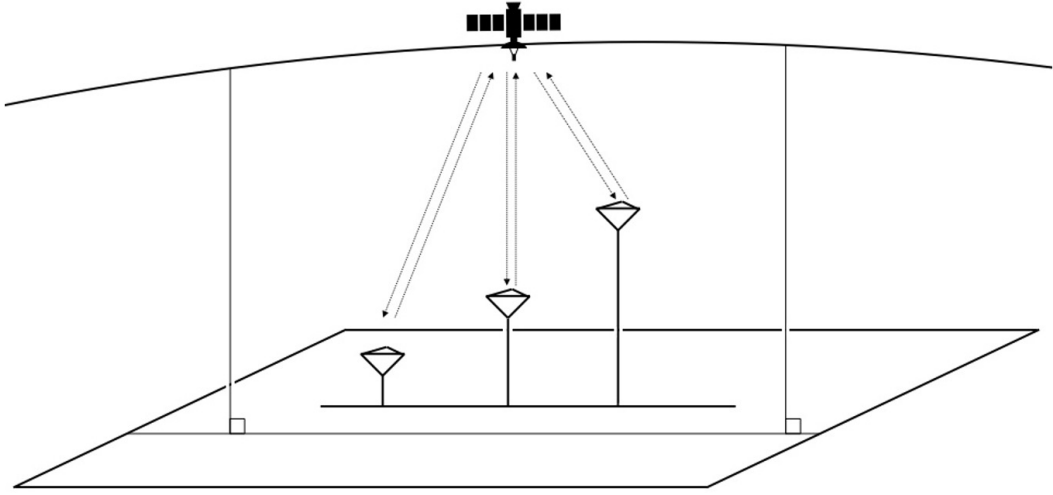
FIGURE 3.20: The ADCR concept of simultaneous calibration of a
satellite altimeter using corner reflector with different elevation.

calibration the TCA between the two measured ranges can be calculated and com-
pared against the altimeter's sampling rate since the targets' positions are accurately
known. This comparison of the two TCAs results into a new datation bias.

It should be noted that in parallel with ADCR, the standard absolute calibration
(Section 3.2.1) can be performed regularly with each one of the corner reflectors.
Therefore, a single pass of an altimetry satellite will result into multiple independent
absolute biases originating from the point targets.

3.3   Calibration Accounting for Spacecraft Attitude

3.3.1   The Case of Jason-3 Attitude Determination

The Jason-3 attitude angles are evaluated at the TCA over CDN1 and GVD1 transpon-
der sites for each cycle using the methodology of Section 2.6.1. The files containing
the Jason-3 quaternion data for the construction of matrix $\mathbf{R}_{\text{IRS}\rightarrow\text{SAT}}$ are acquired
from the NASA's Crustal Dynamics Data Information System (CDDIS). Each quater-
nion file covers a time period of 28 hours with a temporal resolution of 30 seconds.
The data stored in consecutive quaternion files have a two-hour overlap. The quater-
nions at a specific TCA are estimated using spherical linear interpolation. Daily val-
ues of mass and CoG displacements for Jason-3 are obtained from the International
DORIS Service (IDS). The estimation of CoG displacements at TCA is performed
using linear interpolation. The estimated CoG displacements are then used for the
calculation of $\delta\mathbf{V}_{\text{SAT}}$ parameter.

The attitude angles are presented in Fig. 3.21 for the entire duration of Jason-3
operational phase (February 2016 – April 2022) before transitioning to an interleaved
orbit (after the end of Sentinel-6 MF tandem phase). The temporal resolution of all
time series in Fig. 3.21 is 9.915 days, which corresponds to the repeat period of Jason-
3. Each sample represents a different cycle, with the entire time series spanning 226
cycles. The presence of an attitude angle for a specific cycle does not necessarily
denote an operation of the corresponding transponder. For example, the calculation
of attitude angles for the GVD1 transponder location is performed for the entire
duration of Jason-3 altimetric phase, although operation of the GVD1 transponder
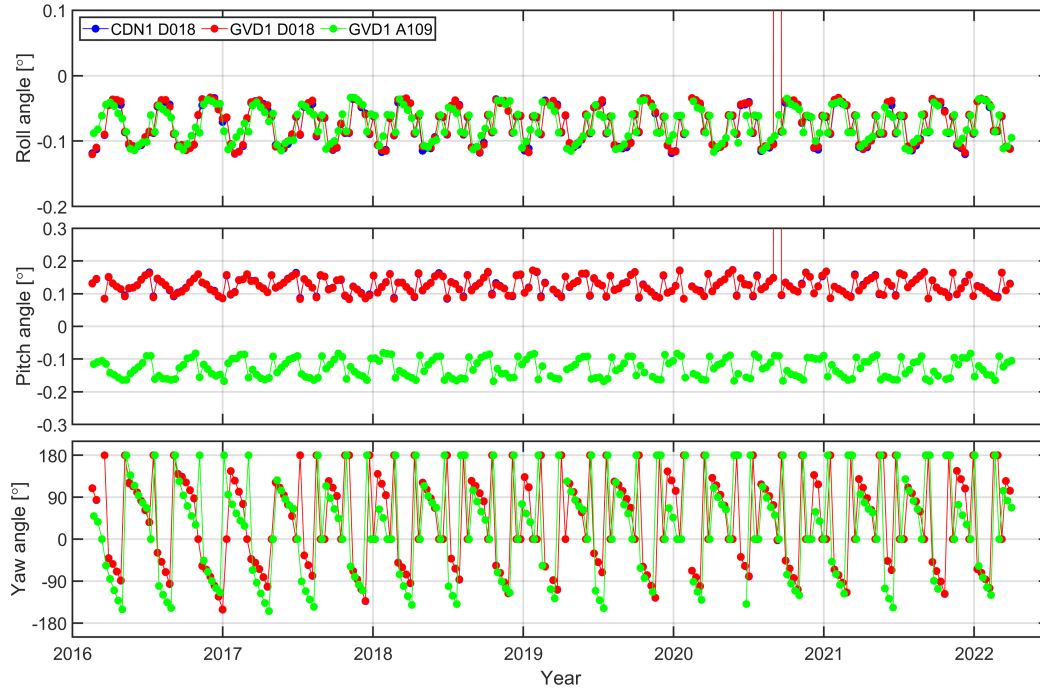
FIGURE 3.21: Jason-3 roll, pitch and yaw angles at CDN1 and
GVD1 calibration sites.

commenced in October 2021. Therefore, all attitude angles for the GVD1 D018 and GVD1 A109 times series before October 2021 are referred to the Jason-3 TCA over the "apparent" GVD1 transponder location. Obtaining a complete time series for the GVD1 site increases the confidence of spectral analysis on attitude angles.

Due to the relatively short time (approximately 11 seconds) it takes Jason-3 to travel from the CDN1 Cal/Val site in Crete to the GVD1 Cal/Val site in Gavdos, the attitude angles remain almost unchanged and thus the CDN1 D018 and GVD1 D018 time series overlap (Fig. 3.21). From the results of Fig. 3.21, an incident of abnormal roll ($\theta_r = 7.25°$) and pitch ($\theta_p = 19.58°$) angles is evident in both CDN1 D018 and GVD1 D018 time series at 2020.67 (9 September 2020 22:32:43, cycle 169). These extreme angles are caused by the on-board gyro calibration, which occurred on 9th of September 2020 from 22:13:36 to 23:04:55 (H. Roinard, 2021). It is worth noting that for this date, the returned waveform did not correspond to a typical point target response. Consequently, the calibration of Jason-3 could not be performed. Prior to the examination of the satellite attitude, this strange behavior of the returned waveform could not be explained, therefore, the reason for this unsuccessful calibration was not clear to the PFAC Cal/Val team. This highlights the importance of always examining the satellite attitude and not taking for granted nominal attitude in the context of Cal/Val activities.

There are sporadic gaps in the time series of Jason-3 attitude angles in Fig. 3.21, e.g., on 26 February 2019 (cycle 112), 8 February 2020 (cycle 147) and 16 June 2020 (cycle 160), because the satellite was set on safe hold mode (H. Roinard, 2021) and thus, quaternions are not available. The general behavior of the roll angle θ_r is approximately the same for all time series, with values fluctuating from $\theta_r = -0.12°$ to $-0.03°$. The pitch angle θ_p is positive for the descending pass D018 from $\theta_p = +0.08°$ to $+0.17°$ and negative for the ascending pass A109 from $\theta_p = -0.17°$ to $-0.08°$; hence, the pitch angle is also in agreement in terms of absolute magnitude for all

TABLE 3.5: Main periods (in days) of Jason-3 attitude angles obtained
by spectral analysis with a Hann window.

	Roll	**Pitch**	**Yaw**
CDN1/GVD1 D018	117, 39, 32, 27, 23.5, 21	117, 39, 32, 27, 23.5, 21	117, 88, 58, 47, 39, 32, 27, 23.5, 21
GVD1 A109	117, 39, 32, 27, 23.5, 21	117, 70, 51, 39, 32, 27, 23.5, 21	117, 58, 39, 32, 27, 23.5, 21

time series. Finally, the yaw angle θ_y is between $-180°$ and $180°$ in all cases, as expected. It is worth noting that the satellite spacecraft performs recurrent yaw flip maneuvers (i.e., yaw transitions from $\theta_y = 0°$ to $\pm 180°$ and conversely) approximately every 58 days. These maneuvers are carried out for sufficient power inflow and their scheduling is based on a Sun-pointing algorithm.

A spectral analysis of Jason-3 attitude angles over CDN1 and GVD1 transponders is performed to identify main periodic components. The amplitude spectra are calculated using the standard Fast Fourier transform algorithm and are provided in Fig. 3.22. The results reveal various periodic components for Jason-3 roll, pitch and yaw angles. The periodicities of the most distinct spectral peaks are estimated after applying a Hann window to the time series of Fig. 3.21 to reduce side lobe artifacts and are summarized in Table 3.5. Differences are observed in both peak amplitudes and peak periodicities among the different attitude angles and satellite passes. For example, the amplitude of the roll angle at 117 days period is larger for D018 compared to A109, whereas the opposite is true for the yaw angle amplitude at 58 days period. Additionally, there are periodic constituents present in D018 amplitude spectra but not in A109, and vice versa. For example, the periodic constituent of 88 days for the yaw angle spectrum, which is evident in D018 but does not exist in A109. Another case is the periodic constituent of 51 days for the pitch angle, which is only present in A109 (Tab. 3.5).

For the majority of cases, the constituent with the strongest amplitude corresponds to the 117 days period, followed by the 39 days period for the roll and pitch angles, and by the 58 days period for the yaw angle. Two notable exceptions are the pitch amplitude spectra for the CDN1 and GVD1 D018 passes, where the strongest amplitude is at the 39 days period with a marginally higher value than the 117 days period. Some differences in the amplitudes of the most prominent periodic constituents are also evident. For example, the D018 passes have a larger amplitude than A109 at the period of 117 days for the roll angle. The most pronounced periodic constituents (117, 58 and 39 days) of Jason-3 attitude angles are also evident in the time series of range bias, as derived from the CDN1 transponder (Mertikas et al., 2022). The period of 117 days corresponds to Jason-3 draconic period (i.e., period of solar beta angle). Finally, the period of 58 days is the yaw flip-maneuver period of Jason-3 and exists only in yaw angle spectrum, as expected.

3.3.2   Jason-3 Attitude Effects on Transponder Results

The attitude effects of Jason-3 spacecraft on range and datation biases are derived using the methodology of Section 2.6.2. The time series of δB and δT for each successful calibration of D018 and A109 passes over the CDN1 and GVD1 sites, are presented in Fig. 3.23. It is evident from the results that the attitude effect on range bias ranges from approximately -2 mm to $+1$ mm, whereas the effect on datation
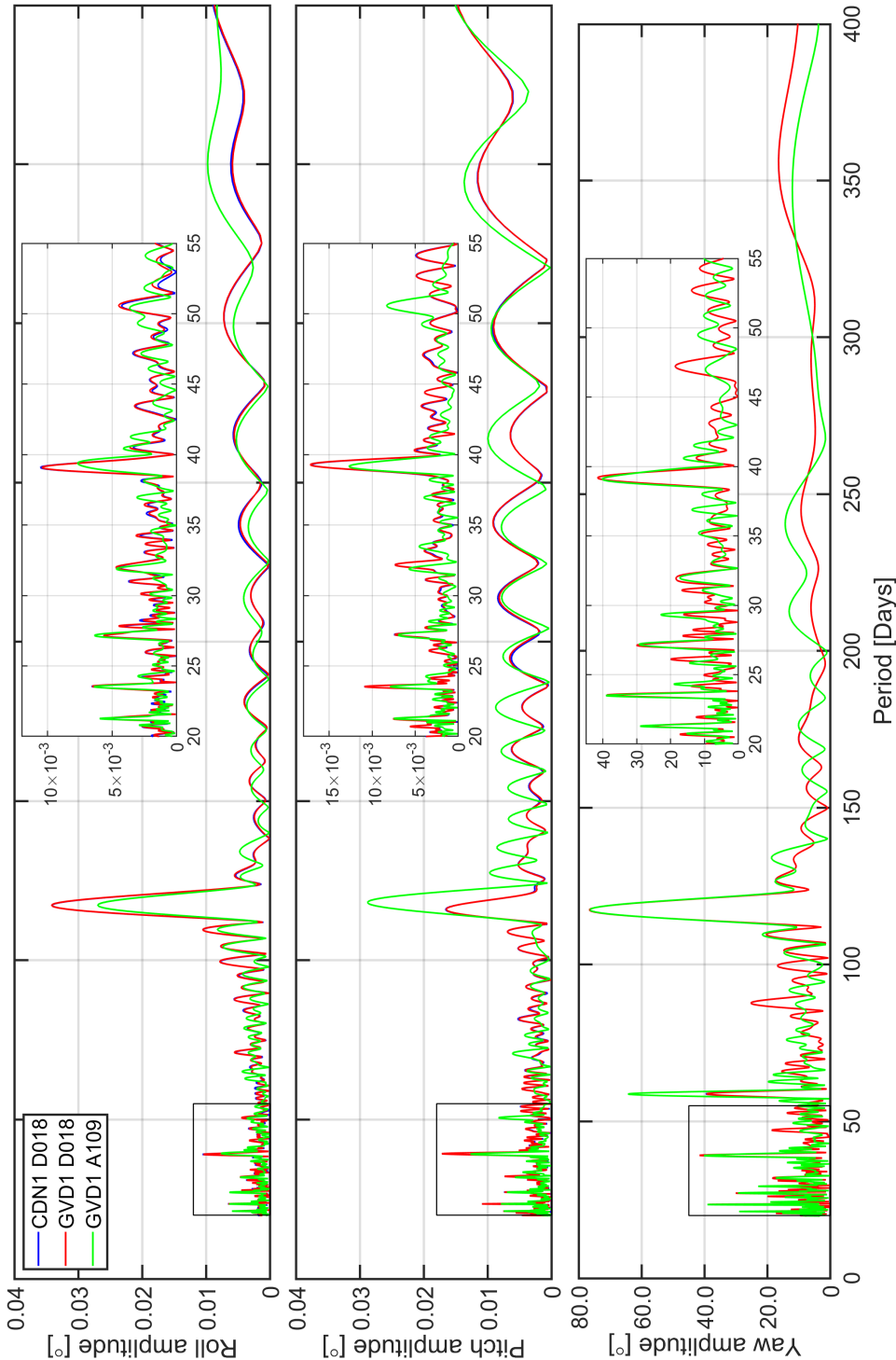
FIGURE 3.22: Jason-3 roll, pitch and yaw amplitude spectrum at CDN1 and GVD1 calibration sites. The framed area on the bottom left is zoomed and presented on the upper right part of the figures.
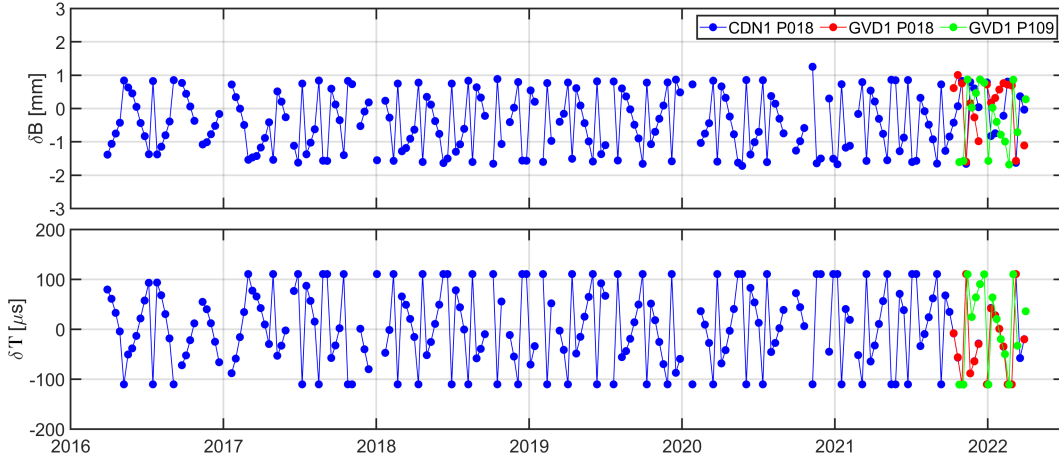
FIGURE 3.23: Time series of Jason-3 attitude effects on range (top)
and datation (bottom) biases.

varies between ± 110 μs. The two effects show an inversely proportional behavior, i.e., as δB increases, δT decreases. It is also apparent from Fig. 3.23 that there are upper and lower limits for the attitude effects on δT, generated by attitude variations. The outer limits of attitude effects stem from the CoG–APC baseline length, which is constant (assuming temporal variations are negligible) and restricted by the physical dimensions of the satellite.

To identify additional patterns in the behavior of δB and δT, we provide scatter plots of the generated attitude effects as a function of roll, pitch, and yaw angles (Fig. 3.24). From the right diagrams of Fig. 3.24 it is evident that attitude effects become large when the yaw angle is either $\theta_y = 0°$ or $\theta_y = \pm 180°$. The APC precedes the CoG with respect to the transponder location on the ground (Table 2.7) when the satellite flies with $\theta_y = 0°$. In this case, the effect on range bias becomes minimum ($\delta B = -1.7$ mm), and datation grows to a maximum, value ($\delta T = 110$ μs). The opposite behavior arises when the satellite flies with $\theta_y = 180°$ with CoG preceding the APC (Table 2.7). In this flying orientation, the effect on range bias becomes maximum ($\delta B = 0.7$ mm), and datation comes to a minimum ($\delta T = -110$ μs). When the satellite is aligned at a right angle with respect to flight direction, where the yaw angle is $\theta_y = \pm 90°$, the impact on datation has its lowest magnitude with $\delta T = 0$ μs.

Datation seems to be affected primarily from the yaw angle. The effect of yaw attitude on δT can be approximated using the relation:

$$\delta T \simeq \frac{\mathbf{V}_{\text{SAT}}^x \cos \theta_y}{|\mathbf{u}|} = \frac{|\text{CoG}; \text{B}_0| \cos \theta_y}{|\mathbf{u}|}, \tag{3.1}$$

where the $\mathbf{V}_{\text{SAT}}^x$ is the projection component of the CoG–APC baseline vector on the x_B-axis in the SAT system which starts from the CoG and terminates at B_0 as presented in Fig. 2.23a. The $|\mathbf{u}|$ represents the magnitude of the satellite's velocity in the EFRS. In practice, Eq. (3.1) describes the time it takes for Jason-3 to cover the distance between APC and CoG projected onto the flight direction. The values of δT are evaluated for the complete range of yaw angles using Eq. (3.1). The results are shown in Fig. 3.24. It is evident that the modeled yaw effect of Eq. (3.1) (shown with red dots on Fig. 3.24) is in good agreement with the actual result of the analytical solution (blue dots) for datation. The attitude angles of pitch and roll seem not to significantly influence the datation as shown in Fig 3.24.
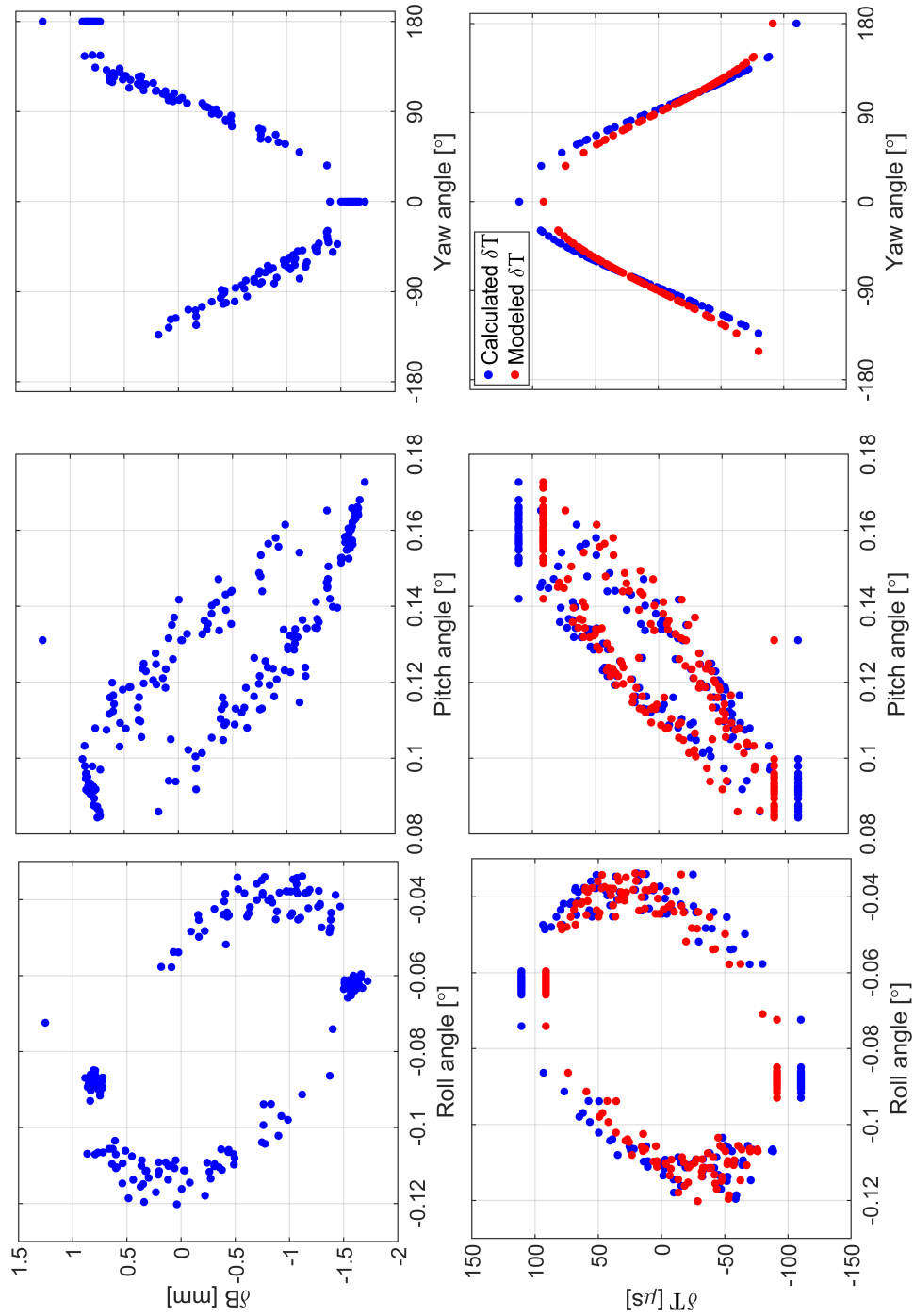
FIGURE 3.24: Jason-3 attitude effects δB (top) and δT (bottom) as a function of yaw plotted with respect to roll, pitch, and yaw for the CDN1 transponder Cal/Val site and the descending pass D018.
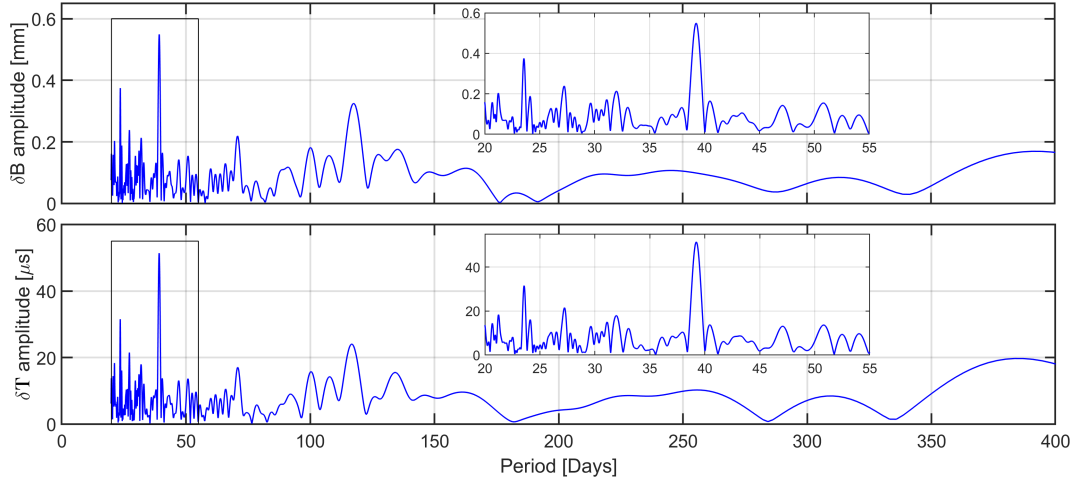
FIGURE 3.25: Amplitude spectrum of Jason-3 attitude effects on range and datation bias on CDN1 D018. The framed area on the bottom left is zoomed and presented on the upper right part of the figures.

Another spectral analysis on δB and δT is also performed to examine any potential propagation of periodic effects of attitude angles to biases. The spectral analysis in Fig. 3.25 indicate that the periods with the greatest amplitude (in descending order of magnitude) are: 39, 23 and 117 days. These periods have already been revealed by the spectral analysis of the angles shown in Fig. 3.22. This resemblance in periodicities corroborates the existence of effects on biases coming from attitude variations.

3.3.3 Jason-3 Crossover Analysis

The GVD1 Cal/Val site is located at a crossover point, which is defined by A109 and D018 passes of Jason-3 and Sentinel-6 MF nominal orbit (Fig. 2.1). The time difference between two consecutive (asceding and descending) satellite passes over GVD1 is about five days. Altimeter calibrations conducted using the GVD1 transponder offer the possibility of crossover analysis by comparing the biases of the ascending and passes. In this section, we calculate the range bias of Jason-3 for both A109 and D018 passes using the conventional and new calibration procedure. We then evaluate the range bias difference per cycle between A109 and D018 for each calibration procedure. This difference defines the crossover bias and can be used to assess the altimeter performance and identify systematic effects. The evaluation and comparison of crossover bias for the two calibration procedures can also yield valuable information regarding attitude effects on transponder results. This experiment is especially interesting for the case of Jason-3 satellite since the spacecraft passes over GVD1 with opposite pitch angles (positive pitch angle for D018 and negative pitch angle for A109), as presented in Fig. 3.21. The same crossover analysis is also performed for Sentinel-6 MF mission, as its orbital characteristics are identical to Jason-3.

According to the results, the proposed calibration procedure improves the Jason-3 crossover bias. Specifically, the mean difference between D018 and A109 using the
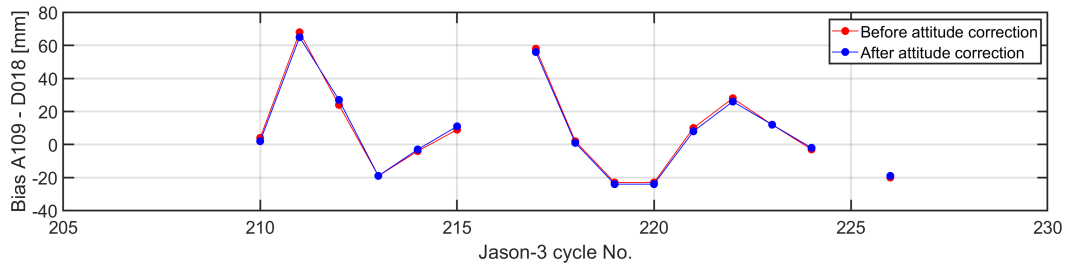
FIGURE 3.26: Jason-3 crossover bias determined by the GVD1 transponder using the conventional (red) and new (blue) calibration procedure.

new calibration is reduced to 7 mm and shows an improvement of 12% compared to conventional calibration (Fig. 3.26). The absence of results for cycles 216 and 225 is because the GVD1 transponder was not operational during that time. The level of improvement presented here is comparable with the results of Jason-3 sea surface height (SSH) crossover analysis reported in Bloßfeld et al. (2020). In their study the calculation of SSH is based on orbits estimated using model-based and observation-based attitude realization.

Chapter 4

Conclusions

The research conducted in this dissertation aimed at improving altimetry calibration by mitigating the major errors in the current procedures and proposing new methodologies. The research objectives and corresponding contributions of this work was divided into four sections.

The first section regarded the estimation of wet delay, the most variable parameter in range calibration. The wet delay was estimated using only one technique based on GNSS. This practice reduced the confidence in the wet delay and thus bias estimation. To mitigate this inadequacy, the implementation of two additional techniques (i.e., using Sentinel-3 OLCI and a ground radiometer) was demonstrated.

Each technique for wet delay estimation was compared against the well stablished methodology using GNSS, before its integration into operational calibration. The data set of OLCI included images with a resolution of 300 m (native resolution) that contained the entire island of Crete and thus the whole GNSS network consisting of ten receivers. This criterion was covered by 12 passes of Sentinel-3A & B because of the 1270 km OLCI swath. Two approaches were followed for the comparison between OLCI and GNSS techniques. The first is the nearest neighbour approach in which the wet delay of the GNSS receiver was compared with the OLCI pixel that contained the GNSS station. In the second, called area of influence, the GNSS value was compared with the average value of a 31×31 OLCI pixels area, centered at the GNSS station. The OLCI wet delays coincided for both approaches inside one standard deviation with those using GNSS stations, except RDK1. The OLCI pixel containing RDK1 was characterized as "water" and the corresponding wet delay estimation was not reliable. Therefore, the nearest neighbour approach could not be applied at RDK1, while for the area of influence the correlation between OLCI and RDK1 was the lowest and the agreement was inside two standard deviations. Although OLCI is generally a reliable technique for estimating wet delay, if the calibration station is adjacent to water and its pixel is characterized as water, OLCI should not be used. On the other hand, the comparison between the ground radiometer and the GNSS operating in CDN1 Cal/Val station, was performed using concurrent observations spanning around four months. The results from the two techniques coincide inside one standard deviation, with an average difference of -9 ± 12 mm.

This dissertation increases the robustness of calibration by adding alternative techniques and assuring the success of calibration even in the case of GNSS receiver malfunction. Additionally, the comparison analysis using independent techniques, increases the confidence in wet delay estimation because the outliers of an individual technique can be detected and rejected without affecting the bias accuracy.

The second section presented the objective of examining alternative point target

calibration methods to mitigate the major uncertainty in calibration with a transponder, i.e., the knowledge of its internal delay. To address this uncertainty, the simultaneous operation of passive targets along with active microwave transponder is proposed.

This work investigated and provided the optimal passive target to deploy in the same calibration network with a transponder. Initially, several types of passive targets were evaluated with analytical calculations and simulations, according to their gain, average radar cross section, half power beam width, operation at multiple frequencies and design complexity. After evaluating various passive targets, such as top hat reflectors, the final candidates were Luneburg reflectors and corner reflectors. The first category gathers preferable characteristics like strong signal amplification (compared to their physical dimensions) and multi-frequency operation. However, Luneburg reflectors were excluded because of their complex design. Therefore, the final candidates with strong gain, wide coverage and simple design were the different types of corner reflectors, i.e., rectangular, circular and triangular. The rectangular gathers the most preferable characteristics (average radar cross section, coverage and simplest shape). After deciding the type, analytical calculations were used to evaluate the radar cross section as a function of the reflector's size. The selected size is a corner reflector comprised of three 1.5 m square plates, resulting in a radar cross section of around 56 dB at Ku and 63 dB at Ka. Thus, the reflected signal can be distinguished at an area of low clutter (for both Ku and Ka), while preserving the reflectors portability. Considering the above, the optimal design, accounting for calibration needs and practical limitations, is the trihedral corner reflector, built by 1.5 m square plates of 5083 aluminum alloy connected with honeycomb aluminum. The usage of honeycomb aluminum offers intrinsic structural integrity to the reflector, removing the need for an exoskeleton, forcing expansions and contractions to lengthen rather than warp the plates.

The tandem operation of diverse targets allows to preserve the transponder as the main reference target, because of its significantly higher SNR, but at the same time continuously monitor its internal delay. The monitoring is accomplished by comparing the transponder's echo with this of the corner reflector. The site for corner reflectors installation (that will expand the PFAC network) has already been selected and called ALX0. The ALX0 is in an area of low clutter and offers the capability of calibrating multiple missions, i.e., Sentinel-6 MF, Sentinel-3A and Sentinel-3B.

In the third section, this dissertation proposes a new methodology of satellite altimetry calibration based on co-located corner reflectors and the estimation of differential bias. Altimetry satellites like the recently launched SWOT and the future CRISTAL mission have increased capabilities and requirements that are not covered by conventional calibration.

Therefore, this dissertation presented a calibration methodology called ADCR, that offers a quantification of altimeter measurements' quality without the errors of atmospheric delays (i.e., wet, dry and ionospheric delay), geophysical effects (i.e., solid Earth, pole and ocean tides, atmospheric pressure and mass loadings) and orbital parameters. This is achieved by comparing the height difference of two (or more) corner reflectors apexes as estimated using altimetric measurements against their known distance determined using conventional spirit leveling. The differential bias originating from this comparison is free from all the common errors of atmospheric delays, geophysical displacements and orbital errors because the targets experience identical effects.

The proposed configuration in ADCR is a distance between targets of 100 m along the track of the calibrated satellite and a height difference of 10 m between the

apexes of adjacent reflectors. In this way, the spatial resolution of FFSAR (around 0.5 m along track) can be used to distinguish each target while having them inside the same altimeter tracking window that usually covers a height difference of around 25 m. The proposed distance between consecutive targets is two orders of magnitude greater than FFASAR spatial resolution to assure that ADCR can be applied to multiple missions with different orbit inclinations. For the case of ALX0 the ADCR methodology can be performed for Sentinel-6 MF, Sentinel-3A & B.

The last section, showed the integration of attitude measurements from star trackers on-board altimetry satellites into calibration processing. Conventionally, the common reference of measured and geometric was performed by adding a constant offset to the measured range. However, the attitude of altimetry satellites during calibration with point targets, affects the relative position between the starting point of measured (APC) and geometrical (CoG) ranges and should be taken into account. This dissertation presented a rigorous processing for referencing at the same satellite point the APC and CoG by adding to the latter a vector that incorporates the satellite's attitude.

For the case of Jason-3, the correction on range and datation biases from CDN1, fluctuated from -2 mm to $+1$ mm and ± 110 μs, respectively. The magnitude of attitude effects on datation bias corresponds to about 30% of its average value. The implementation of the new processing at the crossover between the ascending (A109) and descending (D018) pass over GVD1, showed an improvement of 12% for Jason-3. The proposed calibration procedure for mitigating attitude effects is comprehensive and can be applied to every past, current and future mission with available attitude measurements.

This dissertation presented a holistic approach for addressing all the major uncertainties and improving current calibration by strengthening existing procedures, integrating diverse point targets, proposing new calibration methodologies and revisiting conventional processing. To ensure that calibration procedures are aligned with the requirements of future satellite missions and FRM standards, the methods proposed in this dissertation should be considered in every current and future Cal/Val infrastructure. This work removes the influence of systematic effects both in the ground infrastructure (i.e., internal delay knowledge, atmospheric and geophysical corrections) and on the satellite that depend on both physical characteristics (e.g., internal geometric structure) and attitude realization of each satellite. The potential impact of this work is to reach sub-cm accuracy in the calibration of satellite altimeters.

With regards to PFAC network, the deployment of corner reflectors is currently planned for the acquisition of simultaneous calibrations from the currently operating active transponders and the passive targets. The presence of corner reflectors also allows the implementation of the ADCR approach to estimate the differential bias.

Bibliography

Abdalla, Saleh (2012). "Ku-band radar altimeter surface wind speed algorithm". In: *Marine Geodesy* 35.sup1, pp. 276–298.

Alizadeh, MM et al. (2011). "Global ionosphere maps of VTEC from GNSS, satellite altimetry, and Formosat-3/COSMIC data". In: *Journal of Geodesy* 85.12, pp. 975–987.

Andrade, LA et al. (2003). "Backscattering analysis of flat plate and dihedral corner reflectors using PO and comparison with RCS measurements in anechoic chamber". In: *Proceedings of the 2003 SBMO/IEEE MTT-S International Microwave and Optoelectronics Conference-IMOC 2003.(Cat. No. 03TH8678)*. Vol. 2. IEEE, pp. 719–724.

Archer, Matthew R, Zhijin Li, and Lee-Lueng Fu (2020). "Increasing the space–time resolution of mapped sea surface height from altimetry". In: *Journal of Geophysical Research: Oceans* 125.6, e2019JC015878.

Askne, J and H Nordius (1987). "Estimation of tropospheric delay for microwaves from surface weather data". In: *Radio science* 22.03, pp. 379–386.

Askne, Jan IH and Ed R Westwater (1986). "A review of ground-based remote sensing of temperature and moisture by passive microwave radiometers". In: *IEEE transactions on geoscience and remote sensing* 3, pp. 340–352.

Auriol, A and C Tourain (2010). "DORIS system: the new age". In: *Advances in space research* 46.12, pp. 1484–1496.

Avram, Daniel, Iulian Bratosin, and Dragos Ilie (2016). "Surveying theodolite between past and future". In: *J. Young Sci* 4.

Badatala, Sowkhya et al. (2022). "Radiometric calibration stability assessment of Sentinel-1B using point targets at Surat Basin, Australia". In: *International Journal of Microwave and Wireless Technologies*, pp. 1–8.

Balanis, Constantine A (2012). *Advanced engineering electromagnetics*. John Wiley & Sons.

Baldysz, Zofia et al. (2016). "Comparison of GPS tropospheric delays derived from two consecutive EPN reprocessing campaigns from the point of view of climate monitoring". In: *Atmospheric Measurement Techniques* 9.9, pp. 4861–4877.

Barbaliscia, F, E Fionda, and PG Masullo (1998). "Ground-based radiometric measurements of atmospheric brightness temperature and water contents in Italy". In: *Radio Science* 33.3, pp. 697–706.

Basili, P, O Ciotti, and E Fionda (1998). "Accuracy of physical, statistical and neural network based algorithms for the retrieval of atmospheric water by ground-based microwave radiometry". In: *IGARSS'98. Sensing and Managing the Environment. 1998 IEEE International Geoscience and Remote Sensing. Symposium Proceedings.(Cat. No. 98CH36174)*. Vol. 1. IEEE, pp. 418–420.

Basili, Patrizia et al. (2001). "Atmospheric water vapor retrieval by means of both a GPS network and a microwave radiometer during an experimental campaign in Cagliari, Italy, in 1999". In: *IEEE transactions on geoscience and remote sensing* 39.11, pp. 2436–2443.

Bean, Bradford R and EJ Dutton (1966). *Radio meteorology*. Vol. 92. Superintendentof Documents, US GovernmentPrint. Office.

Bevis, Michael et al. (1994). "GPS meteorology: Mapping zenith wet delays onto precipitable water". In: *Journal of Applied Meteorology (1988-2005)*, pp. 379–386.

Bloßfeld, Mathis et al. (2020). "Observation-based attitude realization for accurate jason satellite orbits and its impact on geodetic and altimetry results". In: *Remote Sensing* 12.4, p. 682.

Boehm, Johannes and Harald Schuh (2004). "Vienna mapping functions in VLBI analyses". In: *Geophysical research letters* 31.1.

Boehm, Johannes, Birgit Werl, and Harald Schuh (2006). "Troposphere mapping functions for GPS and very long baseline interferometry from European Centre for Medium-Range Weather Forecasts operational analysis data". In: *Journal of geophysical research: solid earth* 111.B2.

Bojinski, Stephan et al. (2014). "The concept of essential climate variables in support of climate research, applications, and policy". In: *Bulletin of the American Meteorological Society* 95.9, pp. 1431–1443.

Bonforte, Alessandro et al. (2001). "Calibration of atmospheric effects on SAR interferograms by GPS and local atmosphere models: first results". In: *Journal of Atmospheric and Solar-Terrestrial Physics* 63.12, pp. 1343–1357.

Borel, Christoph C and Daniel Schlaepfer (1996). *Atmospheric pre-corrected differential absorption techniques to retrieve columnar water vapor: Theory and simulations*. Tech. rep. Los Alamos National Lab.(LANL), Los Alamos, NM (United States).

Born, Max and Emil Wolf (2013). *Principles of optics: electromagnetic theory of propagation, interference and diffraction of light*. Elsevier.

Bosser, Pierre et al. (2007). "An improved mean-gravity model for GPS hydrostatic delay calibration". In: *IEEE Geoscience and Remote Sensing Letters* 4.1, pp. 3–7.

Bourg, L. et al. (2021). *Copernicus Sentinel-3 OLCI Land User Handbook*. Tech. rep. S3MPC.ACR.HBK.001. European Space Agency.

Brizzi, Gabriele (2020). *Fundamental Data Records at ESA*. Secro. URL: https://earth.esa.int/eogateway/documents/20142/1484253/ESA-Fundamental-Data-Records-for-Atmospheric-Composition-%28FDR4ATMOS%29-status-and-updates.pdf.

Brown, G 977 (1977). "The average impulse response of a rough surface and its applications". In: *IEEE transactions on antennas and propagation* 25.1, pp. 67–74.

Brunner, Fritz K and Min Gu (1991). "An improved model for the dual frequency ionospheric correction of GPS observations". In: *Manuscripta geodaetica* 16.3, 205–214.

Budden, Kenneth George (1988). *The propagation of radio waves: the theory of radio waves of low power in the ionosphere and magnetosphere*. Cambridge University Press.

Cain, Bruce E, Elisabeth R Gerber, and Iris Hui (2020). "Getting bipartisan support for sea level rise adaptation policies". In: *Ocean & Coastal Management* 197, p. 105298.

Calmant, Stéphane, Jean-François Crétaux, and Frédérique Rémy (2016). "Principles of radar satellite altimetry for application on inland waters". In: *Microwave Remote Sensing of Land Surface*. Elsevier, pp. 175–218.

Carbajal Henken, Cintia et al. (2020). "Assessment of sampling effects on various satellite-derived integrated water vapor datasets using GPS measurements in Germany as reference". In: *Remote Sensing* 12.7, p. 1170.

Carlowicz, M (2015). *Sea Level Rise Hits Home at NASA: Watching Water Rise Right outside the Front Door*. URL: https://earthobservatory.nasa.gov/features/NASASeaLevel (visited on 08/26/2015).

Chandrasekhar, Subrahmanyan (2013). *Radiative transfer*. Courier Corporation.

Chelton, DB et al. (2001). *Satellite Altimetry. Satellite Altimetry and Earth Sciences: a Handbook of Techniques and Applications; ed. by L.-L. Fu and A. Cazenave*.

Clarke, JHR (1978). "BAND SHAPES AND MOLECULAR DYNAMICS IN LIQUIDS." In:

Crane, RK (1976). "Refraction effects in the neutral atmosphere." In: *Astrophysics. Part B: Radio Telescopes*, pp. 186–200.

Cristea, Elena and Phil Moore (2007). "Altimeter bias determination using two years of transponder observations". In: *Proc. Envisat Symp.* Pp. 23–27.

Cullen, R et al. (2007). "ESA's CryoSAT-2 multi-mode level 0 to level 1B science processors–algorithm design and pre-launch verification with ASIRAS". In: *Proceedings of Envisat Symposium*. Citeseer.

Dasgupta, Susmita et al. (2007). "The impact of sea level rise on developing countries: a comparative analysis. World Bank Policy Research Working Paper 4136". In: *Velichko (2007). Ecosystems, Their Properties, Goods, and Services. Climate Change 2007: Impacts, Adaptation and Vulnerability; Contribution of Working Group II to the Fourth Assessment Report of the Intergovernmental Panel on Climate*. Citeseer.

Davis, JL et al. (1985). "Geodesy by radio interferometry: Effects of atmospheric modeling errors on estimates of baseline length". In: *Radio science* 20.6, pp. 1593–1607.

Desai, Shailen D and Bruce J Haines (2004). "Monitoring measurements from the Jason-1 microwave radiometer and independent validation with GPS". In: *Marine Geodesy* 27.1-2, pp. 221–240.

Donlon, Craig et al. (2012). "The global monitoring for environment and security (GMES) sentinel-3 mission". In: *Remote sensing of Environment* 120, pp. 37–57.

Donlon, Craig J et al. (2014). "Strategies for the laboratory and field deployment of ship-borne fiducial reference thermal infrared radiometers in support of satellite-derived sea surface temperature climate data records". In: *Experimental Methods in the Physical Sciences*. Vol. 47. Elsevier, pp. 557–603.

Döring, Björn, Marco Schwerdt, and Robert Bauer (2007). "TerraSAR-X calibration ground equipment". In: *Wave Propagation in Communication, Microwaves Systems and Navigation (WFMN)*.

Duan, Jingping et al. (1996). "GPS meteorology: Direct estimation of the absolute value of precipitable water". In: *Journal of Applied Meteorology and Climatology* 35.6, pp. 830–838.

Edmonds, Alan Robert (1996). *Angular momentum in quantum mechanics*. Princeton university press.

Edwards, Stuart, Philip Moore, and Matt King (2004). "Assessment of the Jason-1 and TOPEX/Poseidon microwave radiometer performance using GPS from offshore sites in the north sea". In: *Marine Geodesy* 27.3-4, pp. 717–727.

Egido, Alejandro, Salvatore Dinardo, and Christopher Ray (2021). "The case for increasing the posting rate in delay/Doppler altimeters". In: *Advances in Space Research* 68.2, pp. 930–936.

Egido, Alejandro and Walter HF Smith (2016). "Fully focused SAR altimetry: Theory and applications". In: *IEEE Transactions on Geoscience and Remote Sensing* 55.1, pp. 392–406.

El-Rabbany, Ahmed and Alfred Kleusberg (2003). "Effect of temporal physical correlation on accuracy estimation in GPS relative positioning". In: *Journal of Surveying Engineering* 129.1, pp. 28–32.

ESA (2019). "*Fiducial Reference Measurements for Sentinel-6*". Tech. rep. ESA-EOPSM-S6-SOW-3607. European Space Research and Technology Centre.

Fernandes, M Joana, Clara Lázaro, and Telmo Vieira (2021). "On the role of the tro-
    posphere in satellite altimetry". In: *Remote Sensing of Environment* 252, p. 112149.

Fernandes, M Joana, Alexandra L Nunes, and Clara Lázaro (2013). "Analysis and
    inter-calibration of wet path delay datasets to compute the wet tropospheric cor-
    rection for CryoSat-2 over ocean". In: *Remote Sensing* 5.10, pp. 4977–5005.

Fernandes, M Joana et al. (2013). "Tropospheric delays from GNSS for application in
    coastal altimetry". In: *Advances in Space Research* 51.8, pp. 1352–1368.

Fernandes, M Joana et al. (2014). "Atmospheric corrections for altimetry studies over
    inland water". In: *Remote Sensing* 6.6, pp. 4952–4997.

Fernandes, Maria Joana and Clara Lázaro (2018). "Independent assessment of sentinel-
    3A wet tropospheric correction over the open and coastal ocean". In: *Remote Sens-
    ing* 10.3, p. 484.

Fionda, E, MJ Falls, and ER Westwater (1991). "Attenuation statistics at 20.6, 31.65
    and 52.85 GHz derived from emission measurements by ground-based microwave
    radiometers". In: *IEE Proceedings H-Microwaves, Antennas and Propagation*. Vol. 138.
    1. IET, pp. 46–50.

Fischer, Jürgen, Ronny Leinweber, and Rene Preusker (2010). "Retrieval of total wa-
    ter vapour content from OLCI measurements". In: *ATBD Water Vapour. Available
    online: https://earth. esa. int/documents/247904/349589/OLCI_L2_ATBD_Water_Vapour.
    pdf (accessed on 20 May 2020)*.

Fixsen, DJ (2009). "The temperature of the cosmic microwave background". In: *The
    Astrophysical Journal* 707.2, p. 916.

Foresta, Luca et al. (2016). "Surface elevation change and mass balance of Icelandic
    ice caps derived from swath mode CryoSat-2 altimetry". In: *Geophysical Research
    Letters* 43.23, pp. 12–138.

Fornari, Marco et al. (2014). "CryoSat: Siral calibration and performance". In: *2014
    IEEE Geoscience and Remote Sensing Symposium*. IEEE, pp. 702–705.

Fu, Lee Lueng and Pierre-Yves Le Traon (2006). "Satellite altimetry and ocean dy-
    namics". In: *Comptes Rendus Geoscience* 338.14-15, pp. 1063–1076.

Fu, Lee-Lueng et al. (1994). *TOPEX/POSEIDON mission overview*.

Garcia-Mondéjar, Albert et al. (2018). "CryoSat-2 range, datation and interferome-
    ter calibration with Svalbard transponder". In: *Advances in Space Research* 62.6,
    pp. 1589–1609.

Garthwaite, Matthew C (2017). "On the design of radar corner reflectors for defor-
    mation monitoring in multi-frequency InSAR". In: *Remote Sensing* 9.7, p. 648.

Garthwaite, Matthew C et al. (2015). "Corner reflectors as the tie between InSAR and
    GNSS measurements: Case study of resource extraction in Australia". In: *Eur. Sp.
    Agency. Spec. Publ., ESA SP SP-731*.

Georgiadou, Yola and Alfred Kleusberg (1988). "On carrier signal multipath effects
    in relative GPS positioning". In: *Manuscripta geodaetica* 13.3, pp. 172–179.

Gibert, Ferran et al. (2023). "A Trihedral Corner Reflector for Radar Altimeter Cali-
    bration". In: *IEEE Transactions on Geoscience and Remote Sensing* 61, pp. 1–8.

Giulicchi, Luisella (2022). *Sentinel-6 Michael Freilich POD Context*. Tech. rep. JC-TN-
    ESA-SY-0420. European Space Agency.

Goody, Richard M and Yuk Ling Yung (1995). *Atmospheric radiation: theoretical basis*.
    Oxford university press.

Gordon, RG (1968). "Correlation functions for molecular motion". In: *Advances in
    Magnetic and Optical Resonance*. Vol. 3. Elsevier, pp. 1–42.

Gordy, Walter, Robert L Cook, and Arnold Weissberger (1984). *Microwave molecular
    spectra*. Vol. 18. Wiley New York.

Gornitz, Vivien (1995). "Monitoring sea level changes". In: *Climatic change* 31.2, 515–544.

Griffiths, HD and B Purseyyed (1989). "A radar altimeter with synthetic aperture processing". In: *1989 19th European Microwave Conference*. IEEE, pp. 281–286.

Grody, Norman C (1988). "Surface identification using satellite microwave radiometers". In: *IEEE Transactions on Geoscience and Remote Sensing* 26.6, pp. 850–859.

Group, Mission Performance Working (2019). *Sentinel-6/Jason-CS Cal/Val Concept*. Tech. rep. JC-PL-ESA-MI-0500. Noordwijk, The Netherlands: European Space Research and Technology Centre, European Space Agency.

H. Roinard, L. Michaud (2021). *Jason-3 validation and cross calibration activities (Annual report 2020)*. Tech. rep. SALP-RP-MA-EA-23473-CLS. CLS.

Haigh, Ivan D et al. (2014). "Timescales for detecting a significant acceleration in sea level rise". In: *Nature Communications* 5.1, pp. 1–11.

Hanson, Susan E and Robert J Nicholls (2020). "Demand for ports to 2050: Climate policy, growing trade and the impacts of sea-level rise". In: *Earth's Future* 8.8, e2020EF001543.

Hartmann, GK and R Leitinger (1984). "Range errors due to ionospheric and tropospheric effects for signal frequencies above 100 MHz". In: *Bulletin géodésique* 58.2, pp. 109–136.

Hausleitner, Walter et al. (2012). "A new method of precise Jason-2 altimeter calibration using a microwave transponder". In: *marine Geodesy* 35.sup1, pp. 337–362.

Hering, Wayne S (1965). "Atmospheric Composition". In: *Handbook of geophysics and space environments*. Air Force Cambridge Research Laboratories. Chap. 6.2.

Herring, TA, RW King, and SC McClusky (2006). "GAMIT". In: *Refer ence Manual. GPS Analysis at MIT. Release* 10, pp. 1–182.

Herring, TA, RW King, SC McClusky, et al. (2010). "Introduction to gamit/globk". In: *Massachusetts Institute of Technology, Cambridge, Massachusetts*.

Herrmann, Sebastian, Hans-Joachim Kretzschmar, and Donald P Gatley (2009). "Thermodynamic properties of real moist air, dry air, steam, water, and ice (RP-1485)". In: *HVAC&R Research* 15.5, pp. 961–986.

Herzberg, Gerhard (1950). "Molecular spectra and molecular structure. Vol. 1: Spectra of diatomic molecules". In: *New York: Van Nostrand Reinhold*.

Hofmann-Wellenhof, Bernhard, Herbert Lichtenegger, and James Collins (2012). *Global positioning system: theory and practice*. Springer Science & Business Media.

Hollmann, Rainer et al. (2013). "The ESA climate change initiative: Satellite data records for essential climate variables". In: *Bulletin of the American Meteorological Society* 94.10, pp. 1541–1552.

Hopfield, Helen S (1971). "Tropospheric effect on electromagnetically measured range: Prediction from surface weather data". In: *Radio science* 6.3, pp. 357–367.

Hopfield, HS (1969). "Two-quartic tropospheric refractivity profile for correcting satellite data". In: *Journal of Geophysical research* 74.18, pp. 4487–4499.

Iijima, BA et al. (1999). "Automated daily process for global ionospheric total electron content maps and satellite ocean altimeter ionospheric calibration based on Global Positioning System data". In: *Journal of Atmospheric and Solar-Terrestrial Physics* 61.16, pp. 1205–1218.

Imel, David A (1994). "Evaluation of the TOPEX/POSEIDON dual-frequency ionosphere correction". In: *Journal of Geophysical Research: Oceans* 99.C12, pp. 24895–24906.

Janssen, Michael A (1994). "Atmospheric remote sensing by microwave radiometry". In:

Janssen, Volker, Linlin Ge, and Chris Rizos (2004). "Tropospheric corrections to SAR interferometry from GPS observations". In: *GPS solutions* 8.3, pp. 140–151.

Jauvin, Matthias et al. (2019). "Integration of corner reflectors for the monitoring of mountain glacier areas with Sentinel-1 time series". In: *Remote Sensing* 11.8, p. 988.

Jay, Frank and JA Goetz (1984). "IEEE Standard Dictionary of Electrical and Electronics Terms, ; The Institute of Electrical and Electronics Engineers". In: *Inc.: New York*.

Jin, Shuanggen et al. (2007). "Seasonal variability of GPS-derived zenith tropospheric delay (1994–2006) and climate implications". In: *Journal of geophysical research: atmospheres* 112.D9.

Katzberg, Stephen J and James L Garrison Jr (1996). *Utilizing GPS to determine ionospheric delay over the ocean*. Tech. rep.

King, RW and Y Bock (2006). *GAMIT reference manual, GPS Analysis at MIT*. Tech. rep. Massachusetts Institute of Technology, Cambridge.

Kloosterman, Jenna L et al. (2017). "The Advanced Microwave Radiometer–Climate Quality (AMR-C) Instrument for Sentinel-6". In:

Knott, Eugene F, John F Schaeffer, and Michael T Tulley (2004). *Radar cross section*. SciTech Publishing.

Komjathy, Attila and George H Born (1999). "GPS-based ionospheric corrections for single frequency radar altimetry". In: *Journal of Atmospheric and Solar-Terrestrial Physics* 61.16, pp. 1197–1203.

Kouba, Jan (2009). "A guide to using International GNSS Service (IGS) products". In:

L. Cerri A. Couhert, P. Ferrage (2022). *DORIS satellites models implemented in POE processing*. Tech. rep. SALP-NT-BORD-OP-16137-CN. Centre national d'ètudes spatiales.

Lamquin, Nicolas et al. (2020). "OLCI A/B tandem phase analysis, part 1: Level 1 homogenisation and harmonisation". In: *Remote Sensing* 12.11, p. 1804.

Le Roy, Yves et al. (2007). "SRAL SAR radar altimeter for sentinel-3 mission". In: *2007 IEEE International Geoscience and Remote Sensing Symposium*. IEEE, pp. 219–222.

Le Vine, David and Neils Skou (2006). *Microwave radiometer systems: design and analysis*. Artech.

Leinweber, Ronny (2010). "Remote sensing of atmospheric water vapor over land areas using MERIS measurements and application to numerical weather prediction model validation". PhD thesis.

Li, Xingxing et al. (2020). "Galileo PPP rapid ambiguity resolution with five-frequency observations". In: *GPS Solutions* 24.1, pp. 1–13.

Lichten, Stephen (1995). "GIPSY-OASIS II: A high precision GPS data processing system and general satellite orbit". In:

Liebe, H (1969). "Calculated tropospheric dispersion and absorption due to the 22-GHz water vapor line". In: *IEEE Transactions on Antennas and Propagation* 17.5, pp. 621–627.

Lin, Xu et al. (2022). "A Spatiotemporal Network Model for Global Ionospheric TEC Forecasting". In: *Remote Sensing* 14.7, p. 1717.

Lindenbergh, Roderick et al. (2008). "High resolution spatio-temporal water vapour mapping using GPS and MERIS observations". In: *International Journal of Remote Sensing* 29.8, pp. 2393–2409.

Luzum, B. and G. Petit. "The IERS Conventions (2010): reference systems and new models". en. In: *Proceedings of the International Astronomical Union* 10.H16 (). ISSN:

1743-9213, 1743-9221. DOI: 10.1017/S1743921314005535. URL: https://www.cambridge.org/core/product/identifier/S1743921314005535/type/journal_article (visited on 09/06/2022).

Lyard, Florent et al. (2006). "Modelling the global ocean tides: modern insights from FES2004". In: *Ocean dynamics* 56.5, pp. 394–415.

Maiwald, Frank et al. (2016). "Reliable and stable radiometers for Jason-3". In: *IEEE Journal of Selected Topics in Applied Earth Observations and Remote Sensing* 9.6, 2754–2762.

Makarau, Aliaksei et al. (2016). "APDA water vapor retrieval validation for Sentinel-2 imagery". In: *IEEE Geoscience and Remote Sensing Letters* 14.2, pp. 227–231.

Marini, John W (1972). "Correction of satellite tracking data for an arbitrary tropospheric profile". In: *Radio Science* 7.2, pp. 223–231.

Meloni, Marco et al. (2015). "Recent developments in radar altimetry over land and their application to the CryoSat-2 mission". In: *IEEE Aerospace and Electronic Systems Magazine* 30.10, pp. 28–36.

Mertikas, Stelios et al. (2020a). "The ESA Permanent Facility for altimetry calibration: Monitoring performance of radar altimeters for Sentinel-3A, Sentinel-3B and Jason-3 using transponder and sea-surface calibrations with FRM standards". In: *Remote Sensing* 12.16, p. 2642.

Mertikas, Stelios et al. (2020b). "Validation of Sentinel-3 OLCI integrated water vapor products using regional GNSS measurements in crete, Greece". In: *Remote Sensing* 12.16, p. 2606.

Mertikas, Stelios P et al. (2018). "Fifteen years of Cal/Val service to reference altimetry missions: Calibration of satellite altimetry at the Permanent Facilities in Gavdos and Crete, Greece". In: *Remote Sensing* 10.10, p. 1557.

Mertikas, Stelios P et al. (2019). "Fiducial Reference Measurements for Satellite Altimetry Calibration: The Constituents". In: *Fiducial Reference Measurements for Altimetry*. Springer, pp. 1–6.

Mertikas, Stelios P et al. (2022). "Performance evaluation of the CDN1 altimetry Cal/Val transponder to internal and external constituents of uncertainty". In: *Advances in Space Research*.

Moran, JM and BR Rosen (1981). "Estimation of the propagation delay through the troposphere from microwave radiometer data". In: *Radio Science* 16.2, pp. 235–244.

Müller, Felix L et al. (2019). "Dynamic ocean topography of the northern Nordic seas: a comparison between satellite altimetry and ocean modeling". In: *The Cryosphere* 13.2, pp. 611–626.

Nazarnia, Hadi et al. (2020). "A systematic review of civil and environmental infrastructures for coastal adaptation to sea level rise". In: *Civil engineering journal* 6.7, pp. 1375–1399.

Niell, AE (2001). "Preliminary evaluation of atmospheric mapping functions based on numerical weather models". In: *Physics and Chemistry of the Earth, Part A: Solid Earth and Geodesy* 26.6-8, pp. 475–480.

Niell, Arthur E (1996). "Global mapping functions for the atmosphere delay at radio wavelengths". In: *Journal of geophysical research: solid earth* 101.B2, pp. 3227–3246.

Obligis, E, N Tran, and Laurence Eymard (2004). "An assessment of Jason-1 microwave radiometer measurements and products". In: *Marine Geodesy* 27.1-2, 255–277.

Pauling, Linus and E Bright Wilson (2012). *Introduction to quantum mechanics with applications to chemistry*. Courier Corporation.

Paziewski, Jacek, Rafal Sieradzki, and Radoslaw Baryla (2018). "Multi-GNSS high-rate RTK, PPP and novel direct phase observation processing method: Application to precise dynamic displacement detection". In: *Measurement Science and technology* 29.3, p. 035002.

Perrygo, C (1987). "TOPEX satellite yaw maneuvers". In: *IOC* 968, pp. 87–074.

Petit, G and B Luzum (2010a). "Frankfurt am Main: Verlag des Bundesamts für Kartographie und Geodäsie". In: *IERS Conventions, Frankfurt, Germany, Appl. Note* 36, p. 179.

Petit, Gérard and Brian Luzum (2010b). *IERS Conventions 2010 (IERS Technical Note; 36), Frankfurt am Main: Verlag des Bundesamts für Kartographie und Geodäsie, 179 pp.* Tech. rep. ISBN 3-89888-989-6.

Petty, Grant William (2006). *A first course in atmospheric radiation*. Sundog Pub.

Picard, Bruno et al. (2020). "Assessment of the "zero-bias line" homogenization method for microwave radiometers using Sentinel-3A and Sentinel-3B tandem phase". In: *Remote Sensing* 12.19, p. 3154.

Plummer, Stephen, Pascal Lecomte, and Mark Doherty (2017). "The ESA climate change initiative (CCI): A European contribution to the generation of the global climate observing system". In: *Remote Sensing of Environment* 203, pp. 2–8.

Powell, Redvers J. (1986). "Relative Vertical Positioning Using Ground-Level Transponders with the ERS-1 Altimeter". In: *IEEE Transactions on Geoscience and Remote Sensing* GE-24.3, pp. 421–425. DOI: 10.1109/TGRS.1986.289601.

Psychas, Dimitrios, Sandra Verhagen, and Peter JG Teunissen (2020). "Precision analysis of partial ambiguity resolution-enabled PPP using multi-GNSS and multi-frequency signals". In: *Advances in Space Research* 66.9, pp. 2075–2093.

Quartly, Graham D et al. (2018). "Review of radar altimetry techniques over the Arctic ocean: Recent progress and future opportunities for sea level and sea ice research". In: *The Cryosphere Discussions*, pp. 1–51.

Radiometrics (2008). *Profiler Operator's Manual*. English. Radiometrics Corporation. 87 pp.

Raney, R Keith (1998). "The delay/Doppler radar altimeter". In: *IEEE Transactions on Geoscience and Remote Sensing* 36.5, pp. 1578–1588.

Rango, A, ATC Chang, and JL Foster (1979). "The utilization of spaceborne microwave radiometers for monitoring snowpack properties". In: *Hydrology Research* 10.1, pp. 25–40.

Ray, Chris et al. (2014). "SAR altimeter backscattered waveform model". In: *IEEE Transactions on Geoscience and Remote Sensing* 53.2, pp. 911–919.

Ray, Richard D (2020). "Daily harmonics of ionospheric total electron content from satellite altimetry". In: *Journal of Atmospheric and Solar-Terrestrial Physics* 209.

Raynal, M et al. (2018). "From conventional to Delay Doppler altimetry: A demonstration of continuity and improvements with the Cryosat-2 mission". In: *Advances in Space Research* 62.6, pp. 1564–1575.

Riccardi, Umberto, Umberto Tammaro, and Paolo Capuano (2021). "Tropospheric Delay in the Neapolitan and Vesuvius Areas (Italy) by Means of a Dense GPS Array: A Contribution for Weather Forecasting and Climate Monitoring". In: *Atmosphere* 12.9, p. 1225.

Roca, M et al. (2013). "Transponder Calibration of CryoSat-2 Datation, Range and Interferometric Phase Errors". In: *20 Years of Progress in Radar Altimatry* 710, p. 80.

Rose, Stine Kildegaard et al. (2019). "Arctic Ocean sea level record from the complete radar altimetry era: 1991–2018". In: *Remote Sensing* 11.14, p. 1672.

Rosenkranz, Philip (1993). "Absorption of microwaves by atmospheric gases". In: John Wiley and Sons.

Ruck, GT, DE Barrick, and WD Stuart (2002). *Radar Cross Section Handbook, vol. 1, 3 vols. Newport Beach*.

Ruf, Christopher S et al. (1994). "TOPEX/POSEIDON microwave radiometer performance and in-flight calibration". In: *Journal of Geophysical Research: Oceans* 99.C12, pp. 24915–24926.

Saastamoinen, J (1972). "Atmospheric correction for the troposphere and stratosphere in radio ranging satellites". In: *The use of artificial satellites for geodesy* 15, pp. 247–251.

— (1973). "Contributions to the theory of atmospheric refraction". In: *Bulletin Géodésique (1946-1975)* 107.1, pp. 13–34.

Santerre, Rock and Alain Geiger (2018). "Geometry of GPS relative positioning". In: *GPS Solutions* 22.2, pp. 1–14.

Sarabandi, Kamal and Tsen-Chieh Chiu (1996). "Optimum corner reflectors for calibration of imaging radars". In: *IEEE Transactions on antennas and Propagation* 44.10, pp. 1348–1361.

Scagliola, Michele and Pietro Guccione (2020). "Datation and range calibration of radar altimeter exploiting fully focused SAR processing". In: *IEEE Geoscience and Remote Sensing Letters* 18.3, pp. 480–483.

Scharroo, Remko et al. (2016). "Jason continuity of services: continuing the Jason altimeter data records as Copernicus Sentinel-6". In: *Ocean Science* 12.2, pp. 471–479.

Schroeder, John A and Ed R Westwater (1991). "User's guide to WPL microwave radiative transfer software". In: *NASA STI/Recon Technical Report N* 92, p. 26809.

Shangguan, Ming et al. (2015). "Validation of GPS atmospheric water vapor with WVR data in satellite tracking mode". In: *Annales Geophysicae*. Vol. 33. 1. Copernicus GmbH, pp. 55–61.

Sibois, Aurore et al. (2017). "Ensuring a smooth operational transition from GIPSY-OASIS to GipsyX: product verification and validation overview". In: *IGS Workshop Poster*, pp. 1–9.

Sibthorpe, Ant et al. (2011). "Calibration and validation of the Jason-2/OSTM advanced microwave radiometer using terrestrial GPS stations". In: *Marine Geodesy* 34.3-4, pp. 420–430.

Sorensen, KW (1991). "A dihedral corner reflector model for full polarization calibration of RCS measurements". In: *Antennas and Propagation Society Symposium 1991 Digest*. IEEE, pp. 748–751.

Strandberg, MWP, HR Johnson, and JR Eshbach (1954). "Apparatus for microwave spectroscopy". In: *Review of Scientific Instruments* 25.8, pp. 776–792.

Sun, Guangde et al. (2017). "An efficient polarimetric SAR calibration algorithm using corner reflectors". In: *Canadian Journal of Remote Sensing* 43.3, pp. 286–296.

Team, Sentinel-3 CalVal (2016). *Sentinel-3 OLCI-B Spectral Response Functions from Pre-Flight Characterization*. Tech. rep. S3-TN-ESA-OL-660. Noordwijk, The Netherlands: European Space Research and Technology Centre, European Space Agency.

Thayer, Gordon D (1974). "An improved equation for the radio refractive index of air". In: *Radio Science* 9.10, pp. 803–807.

Timmermans, BW et al. (2020). "Global wave height trends and variability from new multimission satellite altimeter products, reanalyses, and wave buoys". In: *Geophysical Research Letters* 47.9, e2019GL086880.

Townes, Charles H and Arthur L Schawlow (2013). *Microwave spectroscopy*. Courier Corporation.

Tregoning, Paul and Tonie van Dam (2005). "Atmospheric pressure loading corrections applied to GPS data at the observation level". In: *Geophysical Research Letters* 32.22.

Tucker, AJ and BM Fannin (1968). "Analysis of ionospheric contributions to the Doppler shift of CW signals from artificial Earth satellites". In: *Journal of Geophysical Research* 73.13, pp. 4325–4334.

Ulaby, Fawwaz T, Richard K Moore, and Adrian K Fung (1981). "Microwave remote sensing: Active and passive. volume 1-microwave remote sensing fundamentals and radiometry". In:

Vallado, David A (2001). *Fundamentals of astrodynamics and applications*. Vol. 12. Springer Science & Business Media.

Van Vleck, JH (1947a). "The absorption of microwaves by oxygen". In: *Physical Review* 71.7, p. 413.

— (1947b). "The absorption of microwaves by uncondensed water vapor". In: *Physical Review* 71.7, p. 425.

Vignudelli, Stefano et al. (2019). "Satellite altimetry measurements of sea level in the coastal zone". In: *Surveys in geophysics* 40.6, pp. 1319–1349.

Wallace, John M and Peter V Hobbs (2006). *Atmospheric science: an introductory survey*. Vol. 92. Elsevier.

Wang, Caiyun et al. (2021). "In-orbit calibration and validation of HY-2B altimeter using an improved transponder". In: *IEEE Journal of Selected Topics in Applied Earth Observations and Remote Sensing* 14, pp. 10162–10173.

Wang, Shuen-Yih and Shyh-Kang Jeng (1998). "A compact RCS formula for a dihedral corner reflector at arbitrary aspect angles". In: *IEEE Transactions on Antennas and Propagation* 46.7, pp. 1112–1113.

Webb, FH (1993). "An introduction to the GIPSY/OASIS-II". In: *JPL Publ.*, pp. D–11088.

Wei, Guo et al. (2011). "A transponder system dedicating for the on-orbit calibration of China's new-generation satellite altimeter and scatterometer". In: *Proceedings of 2011 IEEE CIE International Conference on Radar*. Vol. 1. IEEE, pp. 22–25.

Westwater, ER and FO Guiraud (1980). "Ground-based microwave radiometric retrieval of precipitable water vapor in the presence of clouds with high liquid content". In: *Radio Science* 15.05, pp. 947–957.

Willatt, Rosemary et al. (2011). "Ku-band radar penetration into snow cover on Arctic sea ice using airborne data". In: *Annals of Glaciology* 52.57, pp. 197–205.

Yalvac, Sefa (2021). "Investigating the historical development of accuracy and precision of Galileo by means of relative GNSS analysis technique". In: *Earth Science Informatics* 14.1, pp. 193–200.

Zeitlhöfler, Julian (2019). "Nominal and observation-based attitude realization for precise orbit determination of the Jason satellites". PhD thesis. Technical University of Munich, Department of Civil, Geo and Environmental . . .

Zeitlhöfler, Julian (2019). "Nominal and observation-based attitude realization for precise orbit determination of the Jason satellites". MA thesis. Technical University of Munich, Department of Civil, Geo and Environmental Engineering.

Zhang, Lei et al. (2020). "Evaluation of the initial sea surface temperature from the HY-2B scanning microwave radiometer". In: *IEEE Geoscience and Remote Sensing Letters* 18.1, pp. 137–141.